A Multi-Scale Assessment of Solar-Induced Chlorophyll Fluorescence and Its Relation to Northern Hemisphere Forest Productivity

by

Zachary Butterfield

A dissertation submitted in partial fulfillment
of the requirements for the degree of
Doctor of Philosophy
(Atmospheric, Oceanic and Space Sciences)
in the University of Michigan
2021

Doctoral Committee:

Associate Professor Gretchen Keppel-Aleks, Chair
Associate Professor Inés Ibáñez
Associate Professor Eric A. Kort
Professor Allison L. Steiner

Zachary T. Butterfield

zbutterf@umich.edu

ORCID iD: 0000-0003-3120-1430

Dedication

To the friends who keep me sane.

Acknowledgements

While applying to doctoral programs in 2014, a mentor of mine told me that getting a PhD is supposed to change who you are. At the time, I underestimated the truth of that statement and both the cost and reward that the next several years would bring. Looking back, I am incredibly grateful for the experiences I have had at the University of Michigan, and for the many people who have made it a successful journey.

I want to first acknowledge my advisor, Gretchen Keppel-Aleks, for her encouragement and guidance. I could not have asked for a better mentor through navigating these last few years. I want to thank my committee members, Inés Ibáñez, Eric Kort, and Allison Steiner, for their input and advice, as well as Wolfgang Buermann for his invaluable feedback on the second chapter of this dissertation.

So many people contributed to the process of building and maintaining the PhotoSpec system and I want to recognize just a few of those individuals. Katja Grossmann and Jochen Stutz for providing their designs and expertise throughout the process, Stephen ‘Simi’ Barr for his instrumental contributions during the initial build and deployment, Brad Angelocci and Robb Gillespie for their help with machining our custom parts, Tonya Thompson for putting up with the countless times I stopped by her office with random McMaster orders, Faye Ogasawara for her help troubleshooting software issues, Chris Vogel and all the other UMBS folks for helping to get the PhotoSpec telescope on the tower and for their accommodations at the station, Gil

Bohrer for providing the AmeriFlux data to compare with, and Katja, Gil, Chris, and Troy Magney for their help in understanding the science behind the data we collected.

I want to thank the past and present AOSS/CLASP community including staff (in addition to those mentioned above, I have to give a shout out to Darren Britten-Bozzone, Bryan White, Kelly Weiseman, and Jessica Pfund), faculty, postdocs, and students. In particular, the Keppel-Aleks group members have all been amazing colleagues to work with. I wish I could have celebrated with all of you in person.

I also want to acknowledge grant funding from NASA, including from the Interdisciplinary Science and Terrestrial Ecology programs (grants NNX17AK19G, 80NSSC17K0116, and NNX17AE14G), as well as funding through the Rackham Merit Fellowship Program.

Lastly, I need to thank the mentors and educators throughout my life who encouraged and influenced me to ultimately pursue a PhD, and the friends who have kept me grounded throughout what has been for me in many ways a journey of self-discovery. I would not have made it to where I am without you.

Table of Contents

List of Tables

List of Figures

List of Appendices

Abstract

Photosynthesis, or gross primary productivity (GPP), plays a critical role in the global carbon cycle, since it is the sole pathway for carbon fixation by the biosphere. Quantifying GPP across multiple spatial scales is needed to improve our understanding of current and future behavior of biosphere-atmosphere carbon exchange and subsequent feedbacks on the climate system. Remote sensing represents one method to observe vegetation properties and processes, and solar-induced chlorophyll fluorescence (SIF), a light signal originating from leaves, has been shown to be proportional to GPP on diurnal and seasonal timescales. Recently, new techniques to retrieve SIF from satellite observations have provided an unprecedented opportunity to study GPP on a global scale. The relationship between SIF and GPP, however, is subject to significant uncertainty as it is influenced by a number of ecosystem traits (e.g. plant species, canopy structure, leaf age). In this dissertation, I evaluate SIF signals and their relation to GPP over Northern Hemisphere forest ecosystems.

First, I compare climate-driven variations in satellite-based SIF to both longstanding satellite vegetation indices derived from reflected sunlight and tower-based estimates of GPP. Even when aggregated regionally, interannual variability (IAV) of SIF is found to be subject to low signal-to-noise performance, particularly during summer. However, through a statistical analysis, I show that increases in springtime temperature driven by warmer temperatures are offset by drier, less productive conditions later in the growing season. Summer productivity, however, is more strongly correlated with moisture than with temperature, suggesting that moisture exerts a greater influence on growing season-integrated signals. While these results demonstrate that satellite observations can be used to reveal meaningful carbon-climate interactions, they also show that currently available satellite observations of SIF do not allow for robust studies of IAV at scales comparable to surface-based observations.

To investigate how SIF signals are related to ecosystem function at a local scale, I built and deployed a PhotoSpec spectrometer system to the AmeriFlux tower at the University of Michigan Biological Station (US-UMB) above a temperate deciduous forest. These observations show a strong correlation between SIF and GPP at diurnal and seasonal timescales, but SIF is more closely tied to solar radiation and exhibits a delayed response to water stress-induced losses in summer GPP. This decoupling during drought highlights the challenges in using SIF to detect changes in summertime productivity. However, an increased ratio between red and far-red SIF during drought indicates that the combination of SIF at multiple wavelengths may improve the detection of water stress. Lastly, I explore diurnal and directional aspects of the SIF signal. Observations of SIF are sensitive to sun-sensor geometry, with smaller incident angles (between solar and viewing angles) leading to stronger signals. However, afternoon SIF is typically lower than morning values at equivalent light levels due to ecosystem downregulation, which obfuscates angular dependencies in the afternoon. While satellite observations typically rely on a clear-sky sunlight proxy to scale instantaneous observations of SIF to daily values, these results demonstrate the need to account for sounding geometry and diurnal hysteresis in SIF signals in order to advance the interpretation of satellite observations. Overall, my results provide a multiscale assessment of SIF over Northern Hemisphere forests and emphasize that careful attention must be given to the spatial and temporal scales at which SIF can be used to make inferences about GPP.

Chapter 1

Introduction

1.1 Carbon and the Climate System

An increasing atmospheric concentration of Carbon Dioxide (CO_2) is the primary driver of climate change, contributing, as of 2017 and relative to 1750, 2.0 W/m^2 of a total 3.1 W/m^2 anthropogenic radiative forcing (Bruhwiler et al., 2018). Atmospheric CO_2 continues to increase at a significant rate, due to land-use change and the burning of fossil fuels. However, the oceans and land surface act as a sink for roughly half of anthropogenic carbon emissions, acting to buffer this increase. Future concentrations of CO_2, and subsequent climate impacts, are therefore not only dependent on future carbon emissions, but also on the future behavior of the land and ocean sinks.

The land sink contributes the most uncertainty to current understanding of the global carbon cycle, with current estimates at an average of 3.2 ± 0.6 PgC yr^{-1} for 2009-2018, and has continued to increase alongside anthropogenic carbon emissions (Friedlingstein et al., 2019). Both the drivers and geographic locations behind the long-term behavior of the land sink are not well understood, with potential explanations including carbon fertilization in tropical forests or regrowth of forests in northern midlatitudes (Schimel et al., 2015). In addition to significant uncertainty, the land sink is also highly variable from year to year, as it is heavily influenced by interannual variability in climate conditions. Because year-to-year variations in biosphere carbon fluxes reveal sensitivities of ecosystems to climate conditions, which have implications for the long-term behavior of the land sink (Cox et al., 2013), it is therefore important to assess carbon-climate interactions at multiple temporal scales and across multiple ecosystems.

Specifically in the northern hemisphere, increasing temperatures have impacted biosphere-atmosphere carbon fluxes in part by driving a lengthening growing season. Higher temperatures generally lead to earlier spring growth and enhanced spring productivity (Barichivich et al., 2012), although the influence of temperature on spring carbon uptake has been shown to be weakening (Piao et al., 2017). In contrast, higher temperatures have also been found to correlate with a higher CO_2 seasonal cycle minimum, indicating decreased carbon uptake (Wunch et al., 2013). These divergent impacts on ecosystem fluxes can be partly reconciled by identifying competing influences on different components (e.g. photosynthesis, decomposition) of total carbon exchange. In addition to temperature, water availability also plays a critical role in the behavior of ecosystem productivity, although its influences are also subject to competing effects (Jung et al., 2017). To improve our understanding of the biosphere carbon sink and our ability to predict its future behavior, it is therefore important to observe and assess how climate conditions influence individual fluxes that contribute to the total land carbon sink. An improved understanding of these relationships will subsequently improve our ability to gauge how the global carbon cycle will respond to future climate change-induced shifts in temperature and precipitation, and the feedbacks these responses will exert on the climate system.

1.2 Photosynthesis and Atmosphere-Biosphere Carbon Exchange

While the biosphere carbon sink is currently estimated at ~3.2 PgC yr^{-1} (Friedlingstein et al., 2019), this net flux is the sum of several individual fluxes, the largest of which is carbon uptake via photosynthesis, or gross primary productivity (GPP). Photosynthesis occurs when sunlight absorbed by leaves excites electrons within photosystems II and I, which in turn power redox reactions that convert CO_2 molecules into sugars. GPP is then offset by autotrophic respiration (R_a), as plants use sugars for growth and maintenance needs, the balance of which is net primary productivity (NPP):

$$NPP = GPP - R_a \tag{1.1}$$

NPP is further offset by heterotrophic respiration (R_h), or the consumption and respiration of organic material by non-primary producing organisms, resulting in net ecosystem productivity (NEP):

$$NEP = GPP - R_a - R_h \tag{1.2}$$

Lastly, net biome productivity (NBP) represents NEP offset by carbon emissions due to fire and disturbance. As all of these individual fluxes represent different mechanisms that interact differently with their surrounding environment, it is important to understand their behavior independently. However, observing and quantifying individual fluxes poses a challenge, with current estimates of GPP ranging from 120 to more than 150 PgC yr^{-1} (Beer et al., 2010; Joanna Joiner et al., 2018; Welp et al., 2011).

Tower-based eddy-flux methods provide one observational method for estimating carbon exchange (Baldocchi et al., 2001). By simultaneously measuring CO_2 concentrations and vertical wind speed above an ecosystem, carbon exchange or NEP can be estimated through the covariance of eddy-driven fluctuations in both quantities. While these observations relate most directly to NEP, partitioning methods can be used to infer GPP and respiration. One traditional

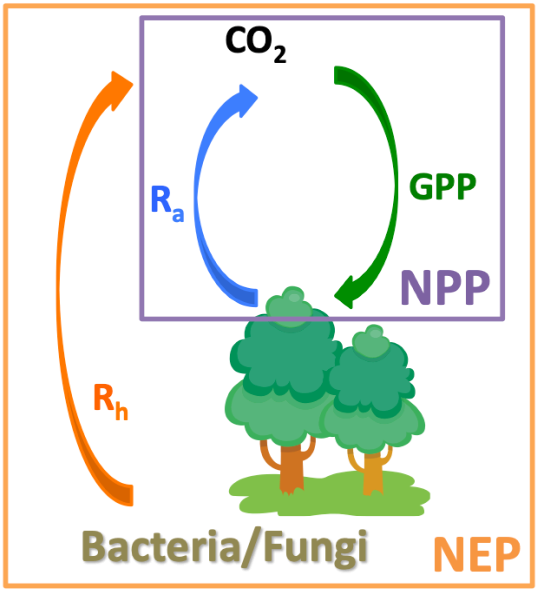

Fig. 1.1. Net ecosystem productivity (NEP) and component carbon fluxes. NEP is defined as the difference between net primary productivity (NPP) and heterotrophic respiration (R_h), and NPP is defined as the difference between gross primary productivity (GPP) and autotrophic respiration (R_a).

method for doing so uses nighttime observations, when photosynthesis is inactive, to gapfill daytime respiration. GPP is then estimated as the difference. A second method, however, uses daytime observations and a light response curve to estimate respiration. Both partitioning methods are subject to respective uncertainties and potential biases (Keenan et al., 2019; Lasslop et al., 2010; Wohlfahrt & Galvagno, 2017). While tower-based observations provide the most direct observations of ecosystem carbon exchange, they require significant infrastructure, leading to networks of towers (e.g. AmeriFlux, FLUXNET) being mostly constrained to North America and Europe, and represent footprints of only 1-5 km^2 (Chen et al., 2011). Limitations in the spatial coverage of eddy-flux observations and the need for productivity-related observations on a global scale suggest the need for remote sensing of vegetation.

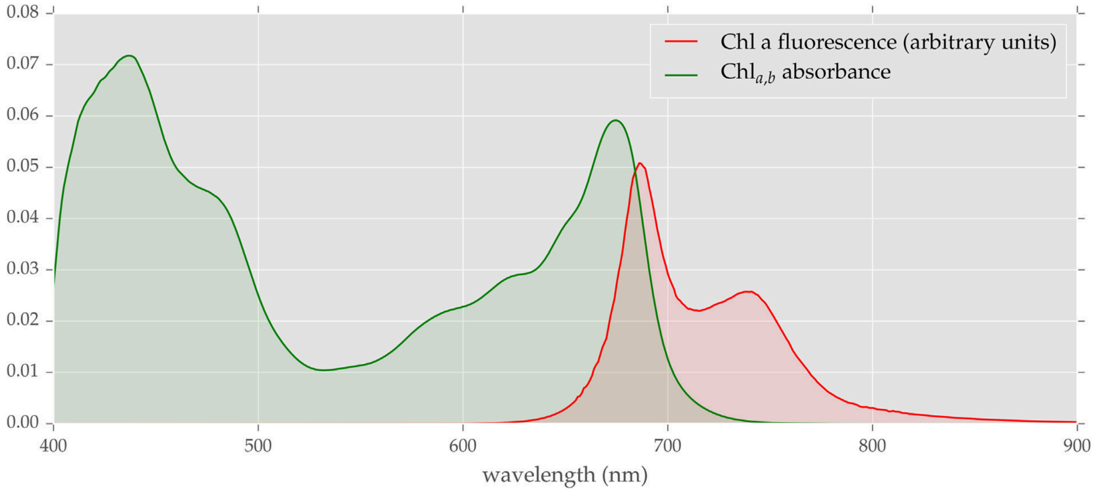

Fig. 1.2. Chlorophyll absorption (green) and chlorophyll fluorescence (red) spectra (from Frankenberg & Berry, 2018).

1.3 Remote Sensing of Vegetation

As photosynthesis is powered by photosynthetically active radiation (PAR), or solar radiation at wavelengths of light absorbed by chlorophyll (between 400 and 700 nm), GPP is dependent on how much PAR is absorbed by vegetation. Sellers (1987) demonstrated that absorbed PAR could be estimated using differences in the reflectance of visible and near-infrared (NIR) light. As visible light is absorbed by chlorophyll, while NIR light is reflected, differences in the reflectance at both wavelengths relate to the fraction of available PAR absorbed by vegetation (fPAR). The differences in how NIR and visible light interact with vegetation have given rise to the use of vegetation indices, the most common of which is the normalized difference vegetation index (NDVI), for monitoring vegetation on a large scale via remote sensing (Huete et al., 2002; Tucker et al., 2005). And Running et al. (2004) developed methods for using NDVI from the MODIS (Moderate Resolution Imaging Spectroradiometer) satellite-based instrument to generate global estimates of ecosystem productivity.

While NIR reflectance from vegetation alone can provide an independent estimate of absorbed PAR (Sellers, 1987), partitioning satellite observations of NIR into vegetation and non-vegetation contributions poses a challenge. Recently, a straightforward estimate of NIR reflectance of vegetation (NIR_V) has shown promise as a computationally efficient method for estimating fPAR, and subsequently ecosystem productivity, via remote sensing. For this method, NDVI is hypothesized to be equivalent to the fraction of NIR originating from vegetation. Thus, NIR_V is calculated as the product of NIR reflectance with NDVI:

$$NIR_V = NIR \times (NDVI - 0.08) \tag{1.3}$$

where NDVI is offset by 0.08 in order to account for the bare soil signal (Badgley et al., 2017).

While satellite observations of NDVI and other vegetation indices and reflectances have advanced our ability to quantify biosphere productivity on a large scale, they provide limited information how photons are used once they are absorbed by vegetation. While GPP is dependent on absorbed PAR, it is also dependent on light use efficiency (LUE), or the efficiency at which absorbed photons are used for photochemistry:

$$GPP = PAR \times fPAR \times LUE \tag{1.4}$$

where fPAR is the fraction of absorbed PAR. As vegetation experiences decreased LUE under environmental stress, these changes are not immediately reflected in NDVI. Thus, estimates of GPP based on vegetation indices rely on modeling approaches to estimate LUE. Traditionally, LUE is assumed to have a biome-specific maximum value under favorable conditions (Ryu et al., 2019), while environmental variables such as temperature and vapor pressure deficit (VPD) are used as a proxy for suboptimal conditions that lead to decreases in LUE (Running et al., 2004).

As leaves are not perfectly efficient at converting absorbed sunlight into chemical energy they employ two mechanisms, non-photochemical quenching (NPQ) and fluorescence, for disposing of excess energy. NPQ occurs when carotenoid pigments are used to absorb photons and convert them to heat, which is then radiated away. This process can account for from a few percent to nearly all of absorbed energy under certain conditions (e.g. evergreen needleleaf forests during winter), and is typically anti-correlated with LUE. Chlorophyll fluorescence occurs when the photosystems within leaves fluoresce photons (generally < 2% of those absorbed) back into the environment at lower wavelengths in the red and NIR region of the electromagnetic spectrum. Chlorophyll fluorescence exhibits two peaks in intensity at ~685 nm and ~740 nm and, in contrast with NPQ, is generally positively correlated with LUE, as increases in NPQ generally lead to simultaneous reductions in both photochemistry and fluorescence (Christian Frankenberg et al., 2011; Van der Tol et al., 2009).

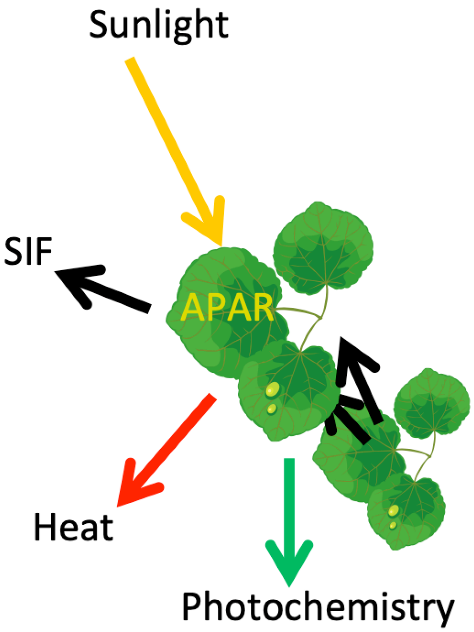

Fig. 1.3. The fate of photons absorbed by vegetation. Absorbed photosynthetically active radiation (APAR) that is not used in photochemistry can be radiated away as heat, or fluoresced as red and near infrared photons in the form of solar-induced chlorophyll fluorescence (SIF). Emitted SIF from lower in the canopy can then be reabsorbed or scattered by other leaves.

1.4 Solar-Induced Chlorophyll Fluorescence (SIF)

Chlorophyll fluorescence has long been used at the leaf level to assess photosystem function. Differences in fluorescence signals under modified light environments can be used to deduce various metrics related to photosystem function (Baker, 2008). For example, while the unmanipulated fluorescence signal from a single light-adapted leaf provides limited information on photosynthetic function, differences between unmanipulated and maximum fluorescence (when the leaf is briefly exposed to a saturating light signal) can be used to estimate the photosystem II operating efficiency. Although light manipulation is not feasible on a large scale, solar-induced chlorophyll fluorescence (SIF) still provides a valuable indicator of photosynthetic activity. However, as chlorophyll fluorescence is only 1-2% of reflected sunlight, quantifying fluorescence via remote sensing is not straightforward. Near the Earth's surface, solar-induced chlorophyll fluorescence can be measured using the infilling of the O2-A band, as fluorescence will decrease the relative depth of atmospheric absorption features. But atmospheric scattering effects weaken the accuracy of such retrievals when using space-based spectra. More recently, techniques have been developed to acquire SIF observations from space using the infilling of solar Fraunhofer lines (Fig. 1.4), which are spectral absorption features originating in the solar atmosphere and, with the exception of aerosol scattering effects, are largely unaffected by interactions with Earth's atmosphere. These developments have lead to a renewed interest in using SIF to monitor and quantify ecosystem productivity on a global scale.

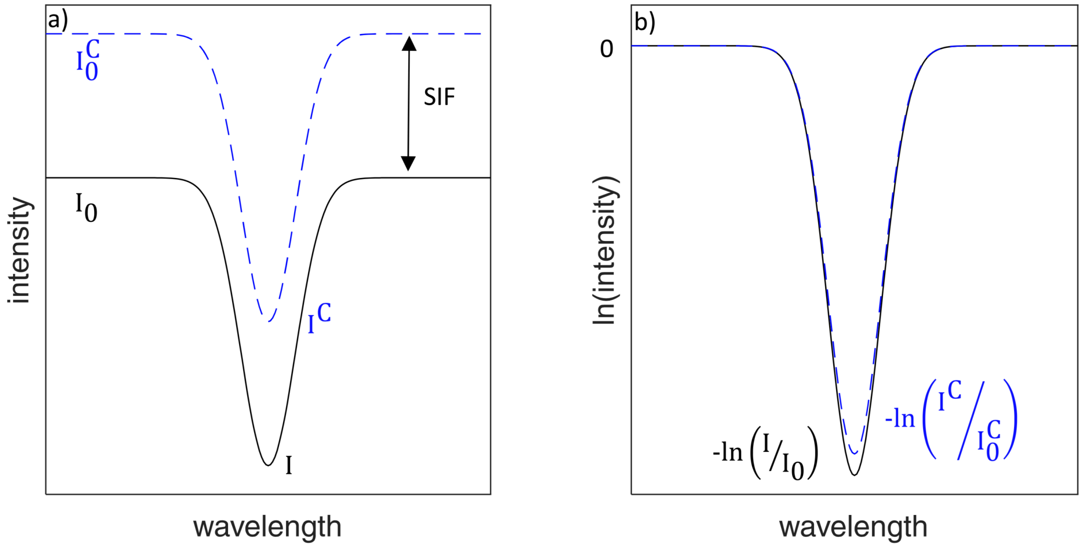

Fig. 1.4. Conceptual illustration of the infilling of an absorption line by SIF. SIF increases the intensity of all wavelengths across an absorption feature (a) and, when line depth is normalized by talking the natural logarithm of intensity (I) divided by maximum intensity outside the line (I_0), the infilling can be observed as the difference between the two spectra (b) (from Grossmann et al., 2018).

Since the first global observations of SIF were reported by J Joiner et al. (2011) and Christian Frankenberg et al. (2011), there has been a proliferation in available space-based SIF data. In addition to GOSAT (Greenhouse gases Observing SATellite), SIF retrievals have been developed for a number of satellite missions including SCIAMACHY (SCanning Imaging Absorption spectroMeter for Atmospheric CHartographY), GOME-2 (Global Ozone Monitoring Instrument), OCO-2 (Orbiting Carbon Observatory), OCO-3 and TROPOMI (TROPospheric Ozone Monitoring Instrument). These SIF datasets have been shown to scale linearly with surface-based eddy flux GPP observations, reflecting geographic and temporal patterns in ecosystem productivity (e.g. Christian Frankenberg et al., 2011; Sun et al., 2017) and providing an opportunity to constrain global carbon uptake (e.g. MacBean et al., 2018). Additionally, SIF observations have been demonstrated to be sensitive to large-scale drought events (Koren et al., 2018; Song et al., 2018; Yoshida et al., 2015), indicating that SIF can be sensitive to stress-induced declines in productivity.

Although initial studies show promising correlations between SIF and GPP, the SIF signal is influenced by a number of factors, including canopy radiative transfer effects and biological function of photosynthetic machinery, that contribute significant unknowns in the exact relationship between SIF and GPP. As SIF is an artifact of photosynthesis, similarly to GPP it is dependent on absorbed PAR. And emitted SIF, especially from lower in the canopy, will subsequently interact with other parts of the canopy, leading to only a fraction of total emitted SIF being observable to top-of-canopy measurements. Thus, SIF is depicted as:

$$\mathrm{SIF} = \mathrm{SIF}_{\mathrm{yield}} \text{ x fPAR x PAR x } f_{\mathrm{esc}} \tag{1.5}$$

where f_{esc} represents the escape fraction of total SIF to top-of-canopy, and $\mathrm{SIF}_{\mathrm{yield}}$ represents the rate per absorbed photon at which SIF is emitted. Because $\mathrm{SIF}_{\mathrm{yield}}$ and f_{esc} are dependent on plant and ecosystem type and canopy structure, most studies separate comparisons between SIF and GPP by ecosystem type (e.g. Guanter et al., 2012), although Sun et al. (2017) found a consistent relationship between both variables across different ecosystems. As satellite observations are generally limited in spatial resolution and temporal frequency, this has presented a need for multi-scale SIF observations for linking satellite observations to local and leaf scales across a variety of ecosystems.

One prominent question for SIF observations is whether or not they reflect information on LUE, as this is an especially difficult facet of GPP to quantify via remote sensing. In Yang et al. (2015) they deployed a tower-based instrument and measured SIF above the temperate deciduous Harvard Forest. They showed a robust linear relationship between SIF and eddy flux GPP on both diurnal and seasonal timescales. And, by dividing both SIF and GPP observations by absorbed PAR, they found a positive, albeit weak, linear relationship between LUE and $\mathrm{SIF}_{\mathrm{yield}}$, suggesting that SIF does provide some information related to LUE. However, other studies have indicated that SIF signals exhibit a much stronger relationship with absorbed PAR than with GPP (Miao et al., 2018; K. Yang et al., 2018). As the strong relationship between SIF and GPP has primarily been demonstrated on seasonal and diurnal timescales that include large swings in available radiation, this brings into question the ability of SIF to reflect changes in GPP on interannual and synoptic timescales where changes in PAR play a less significant role in driving changes in productivity. Additionally, Dechant et al. (2020) demonstrated in cropland ecosystems that seasonal changes in canopy structure and f_{esc} strongly influence the SIF signal and its relationship to GPP. While there has been debate on the advantages of SIF over computationally efficient observations of $\mathrm{NIR}_{\mathrm{V}}$, Zeng et al. (2019) showed that both quantities, despite representing fundamentally different phenomena, are inherently linked through canopy structure as $\mathrm{NIR}_{\mathrm{V}}$ can be related to the escape ratio of far-red SIF:

$$f_{\mathrm{esc}} = \mathrm{NIR}_{\mathrm{V}} / \mathrm{fPAR} \tag{1.6}$$

where fPAR again is the fraction of absorbed PAR. Thus, there is a need to understand how both quantities relate to the other and to ecosystem productivity. In this dissertation, although we touch on $\mathrm{NIR}_{\mathrm{V}}$, we primarily focus on assessing the behavior of SIF signals, particularly above forest ecosystems.

1.5 Goals of This Dissertation

The goal of this dissertation is to improve our understanding of what SIF observations can and can not tell us about ecosystem productivity over northern hemisphere forests. In Chapter 2, I present an intercomparison of GOME-2 SIF observations from 2007 through 2015 with satellite observations of NDVI and NIR_V, and tower-based eddy flux timeseries, to investigate the ability of SIF and other remote sensing data to track variability in GPP specifically on interannual timescales. I further apply a statistical method to satellite observations that allows for the examination of seasonal patterns within interannual timeseries. By comparing these patterns with variability in temperature and moisture availability, I explore the influence that interannual climate variability has on ecosystem productivity and how the influence evolves over the course of the growing season.

Chapters 3 and 4 contains an investigation of SIF signals at a high temporal resolution and small spatial scale, using a PhotoSpec spectrometer system that I built and deployed to the AmeriFlux tower at the University of Michigan Biological Station (US-UMB) throughout the 2018 and 2019 growing seasons. The PhotoSpec system (Grossmann et al., 2018) consists of one broadband and two narrowband spectrometers, allowing for the retrieval of SIF at both the red and far-red regions of the electromagnetic spectrum, as well as NDVI and other vegetation-related parameters. The spectrometer system also uses a telescope with narrow field-of-view (~0.7°) for targeting specific locations within the canopy. Further details can be found in Appendix A.

In Chapter 3 I assess the relationship between SIF signals and eddy flux GPP at the local scale above temperate deciduous forest at US-UMB. Specifically, I track intraseasonal changes in the relationship between SIF and GPP and how both quantities relate to PAR, and explore the response of SIF to stress-induced changes in ecosystem productivity. Further, I investigate differences in the behavior of SIF at red and far-red wavelengths, how these differences evolve over the course of the growing season and differ between years, and if differences in response can improve the ability of SIF observations to detect changes in ecosystem productivity.

In Chapter 4 I focus on diurnal and directional behaviors of the SIF signal. I explore the prominence of diurnal hysteresis patterns in SIF signals and test how diurnal effects influence the ability of instantaneous observations to be scaled to daily values. I then explore the impact that sun-sensor geometry has on observed SIF values, and explore the interplay between both diurnal and geometrical influences. Finally, I discuss the implications these results have for using SIF observations to assess GPP.

Lastly, in Chapter 5, I summarize my findings, discuss gaps in knowledge highlighted by our results, and identify potential directions of future research.

References

Badgley, G., Field, C. B., & Berry, J. A. (2017). Canopy near-infrared reflectance and terrestrial photosynthesis. *Science Advances*, *3*(3), e1602244.

Baker, N. R. (2008). Chlorophyll fluorescence: a probe of photosynthesis in vivo. *Annu. Rev. Plant Biol.*, *59*, 89–113.

Baldocchi, D., Falge, E., Gu, L., Olson, R., Hollinger, D., Running, S., et al. (2001). FLUXNET: A new tool to study the temporal and spatial variability of ecosystem-scale carbon dioxide, water vapor, and energy flux densities. *Bulletin of the American Meteorological Society*, *82*(11), 2415–2434.

Barichivich, J., Briffa, K. R., Osborn, T. J., Melvin, T. M., & Caesar, J. (2012). Thermal growing season and timing of biospheric carbon uptake across the Northern Hemisphere. *Global Biogeochemical Cycles*, *26*(4).

Beer, C., Reichstein, M., Tomelleri, E., Ciais, P., Jung, M., Carvalhais, N., et al. (2010). Terrestrial gross carbon dioxide uptake: global distribution and covariation with climate. *Science*, *329*(5993), 834–838.

Bruhwiler, L., Michalak, A. M., Birdsey, R., Fisher, J. B., Houghton, R. A., Huntzinger, D. N., & Miller, J. B. (2018). Chapter 1: Overview of the global carbon cycle. *Second State of the Carbon Cycle Report (SOCCR2): A Sustained Assessment Report*, 42–70.

Chen, B., Coops, N. C., Fu, D., Margolis, H. A., Amiro, B. D., Barr, A. G., et al. (2011). Assessing eddy-covariance flux tower location bias across the Fluxnet-Canada Research Network based on remote sensing and footprint modelling. *Agricultural and Forest Meteorology*, *151*(1), 87–100.

Cox, P. M., Pearson, D., Booth, B. B., Friedlingstein, P., Huntingford, C., Jones, C. D., & Luke, C. M. (2013). Sensitivity of tropical carbon to climate change constrained by carbon dioxide variability. *Nature*, *494*(7437), 341–344. https://doi.org/10.1038/nature11882

Dechant, B., Ryu, Y., Badgley, G., Zeng, Y., Berry, J. A., Zhang, Y., et al. (2020). Canopy structure explains the relationship between photosynthesis and sun-induced chlorophyll fluorescence in crops. *Remote Sensing of Environment*, *241*, 111733.

Frankenberg, C, & Berry, J. (2018). Solar induced chlorophyll fluorescence: Origins, relation to photosynthesis and retrieval.

Frankenberg, Christian, Fisher, J. B., Worden, J., Badgley, G., Saatchi, S. S., Lee, J., et al. (2011). New global observations of the terrestrial carbon cycle from GOSAT: Patterns of plant fluorescence with gross primary productivity. *Geophysical Research Letters*, *38*(17).

Friedlingstein, P., Jones, M., O'sullivan, M., Andrew, R., Hauck, J., Peters, G., et al. (2019). Global carbon budget 2019. *Earth System Science Data*, *11*(4), 1783–1838.

Grossmann, K., Frankenberg, C., Magney, T. S., Hurlock, S. C., Seibt, U., & Stutz, J. (2018). Remote Sensing of Environment PhotoSpec : A new instrument to measure spatially distributed red and far- red Solar-Induced Chlorophyll Fluorescence. *Remote Sensing of Environment*, *216*(June), 311–327. https://doi.org/10.1016/j.rse.2018.07.002

Guanter, L., Frankenberg, C., Dudhia, A., Lewis, P. E., Gómez-Dans, J., Kuze, A., et al. (2012).

Retrieval and global assessment of terrestrial chlorophyll fluorescence from GOSAT space measurements. *Remote Sensing of Environment*, *121*, 236–251.

Huete, A., Didan, K., Miura, T., Rodriguez, E. P., Gao, X., & Ferreira, L. G. (2002). Overview of the radiometric and biophysical performance of the MODIS vegetation indices. *Remote Sensing of Environment*, *83*(1–2), 195–213.

Joiner, J, Yoshida, Y., Vasilkov, A. P., & Middleton, E. M. (2011). First observations of global and seasonal terrestrial chlorophyll fluorescence from space. *Biogeosciences*, *8*(3), 637–651.

Joiner, Joanna, Yoshida, Y., Zhang, Y., Duveiller, G., Jung, M., Lyapustin, A., et al. (2018). Estimation of terrestrial global gross primary production (GPP) with satellite data-driven models and eddy covariance flux data. *Remote Sensing*, *10*(9), 1346.

Jung, M., Reichstein, M., Schwalm, C. R., Huntingford, C., Sitch, S., Ahlström, A., et al. (2017). Compensatory water effects link yearly global land CO 2 sink changes to temperature. *Nature*, *541*(7638), 516.

Keenan, T. F., Migliavacca, M., Papale, D., Baldocchi, D., Reichstein, M., Torn, M., & Wutzler, T. (2019). Widespread inhibition of daytime ecosystem respiration. *Nature Ecology & Evolution*, *3*(3), 407–415.

Koren, G., van Schaik, E., Araújo, A. C., Boersma, K. F., Gärtner, A., Killaars, L., et al. (2018). Widespread reduction in sun-induced fluorescence from the Amazon during the 2015/2016 El Niño. *Philosophical Transactions of the Royal Society B: Biological Sciences*, *373*(1760), 20170408.

Lasslop, G., Reichstein, M., Papale, D., Richardson, A. D., Arneth, A., Barr, A., et al. (2010). Separation of net ecosystem exchange into assimilation and respiration using a light response curve approach: critical issues and global evaluation. *Global Change Biology*, *16*(1), 187–208.

MacBean, N., Maignan, F., Bacour, C., Lewis, P., Peylin, P., Guanter, L., et al. (2018). Strong constraint on modelled global carbon uptake using solar-induced chlorophyll fluorescence data. *Scientific Reports*, *8*(1), 1973.

Miao, G., Guan, K., Yang, X., Bernacchi, C. J., Berry, J. A., DeLucia, E. H., et al. (2018). Sun-induced chlorophyll fluorescence, photosynthesis, and light use efficiency of a soybean field from seasonally continuous measurements. *Journal of Geophysical Research: Biogeosciences*, *123*(2), 610–623.

Piao, S., Liu, Z., Wang, T., Peng, S., Ciais, P., Huang, M., et al. (2017). Weakening temperature control on the interannual variations of spring carbon uptake across northern lands. *Nature Climate Change*, *7*(5), 359–363.

Running, S. W., Nemani, R. R., Heinsch, F. A., Zhao, M., Reeves, M., & Hashimoto, H. (2004). A continuous satellite-derived measure of global terrestrial primary production. *AIBS Bulletin*, *54*(6), 547–560.

Ryu, Y., Berry, J. A., & Baldocchi, D. D. (2019). What is global photosynthesis? History, uncertainties and opportunities. *Remote Sensing of Environment*, *223*, 95–114.

Schimel, D., Stephens, B. B., & Fisher, J. B. (2015). Effect of increasing CO2 on the terrestrial carbon cycle. *Proceedings of the National Academy of Sciences*, *112*(2), 436–441.

Sellers, P. J. (1987). Canopy reflectance, photosynthesis, and transpiration, II. The role of biophysics in the linearity of their interdependence. *Remote Sensing of Environment*, *21*(2), 143–183.

Song, L., Guanter, L., Guan, K., You, L., Huete, A., Ju, W., & Zhang, Y. (2018). Satellite sun-induced chlorophyll fluorescence detects early response of winter wheat to heat stress in the Indian Indo-Gangetic Plains. *Global Change Biology*, *24*(9), 4023–4037.

Sun, Y., Frankenberg, C., Wood, J. D., Schimel, D. S., Jung, M., Guanter, L., et al. (2017). OCO-2 advances photosynthesis observation from space via solar-induced chlorophyll fluorescence. *Science*, *358*(6360), eaam5747.

Van der Tol, C., Verhoef, W., & Rosema, A. (2009). A model for chlorophyll fluorescence and photosynthesis at leaf scale. *Agricultural and Forest Meteorology*, *149*(1), 96–105.

Tucker, C. J., Pinzon, J. E., Brown, M. E., Slayback, D. A., Pak, E. W., Mahoney, R., et al. (2005). An extended AVHRR 8-km NDVI dataset compatible with MODIS and SPOT vegetation NDVI data. *International Journal of Remote Sensing*, *26*(20), 4485–4498.

Welp, L. R., Keeling, R. F., Meijer, H. A. J., Bollenbacher, A. F., Piper, S. C., Yoshimura, K., et al. (2011). Interannual variability in the oxygen isotopes of atmospheric CO 2 driven by El Niño. *Nature*, *477*(7366), 579–582.

Wohlfahrt, G., & Galvagno, M. (2017). Revisiting the choice of the driving temperature for eddy covariance CO2 flux partitioning. *Agricultural and Forest Meteorology*, *237*, 135–142.

Wunch, D., Wennberg, P. O., Messerschmidt, J., Parazoo, N. C., Toon, G. C., Deutscher, N. M., et al. (2013). The covariation of Northern Hemisphere summertime CO2with surface temperature in boreal regions. *Atmospheric Chemistry and Physics*, *13*(18), 9447–9459. https://doi.org/10.5194/acp-13-9447-2013

Yang, K., Ryu, Y., Dechant, B., Berry, J. A., Hwang, Y., Jiang, C., et al. (2018). Sun-induced chlorophyll fluorescence is more strongly related to absorbed light than to photosynthesis at half-hourly resolution in a rice paddy. *Remote Sensing of Environment*, *216*, 658–673.

Yang, X., Tang, J., Mustard, J. F., Lee, J., Rossini, M., Joiner, J., et al. (2015). Solar-induced chlorophyll fluorescence that correlates with canopy photosynthesis on diurnal and seasonal scales in a temperate deciduous forest. *Geophysical Research Letters*, *42*(8), 2977–2987.

Yoshida, Y., Joiner, J., Tucker, C., Berry, J., Lee, J.-E., Walker, G., et al. (2015). The 2010 Russian drought impact on satellite measurements of solar-induced chlorophyll fluorescence: Insights from modeling and comparisons with parameters derived from satellite reflectances. *Remote Sensing of Environment*, *166*, 163–177.

Zeng, Y., Badgley, G., Dechant, B., Ryu, Y., Chen, M., & Berry, J. A. (2019). A practical approach for estimating the escape ratio of near-infrared solar-induced chlorophyll fluorescence. *Remote Sensing of Environment*, *232*, 111209.

Chapter 2

Satellite Observations Reveal Seasonal Redistribution of Northern Ecosystem Productivity in Response to Interannual Climate Variability[1]

Abstract

Interannual variability (IAV) in ecosystem productivity may reveal vulnerabilities of vegetation to climate stressors. We analyzed IAV of northern hemisphere ecosystems using several remote sensing datasets, including longstanding observations of the normalized difference vegetation index (NDVI) and more novel metrics for productivity including solar-induced chlorophyll fluorescence (SIF) and the near-infrared reflectance of vegetation (NIR_v). Although previous studies have suggested SIF better tracks variations in ecosystem productivity at seasonal timescales, we found that satellite datasets (including SIF) and eddy covariance flux tower observations were subject to significant uncertainty when assessing IAV at fine spatial scales. Even when observations were aggregated regionally, IAV in productivity estimated by the various satellite products were not always well correlated. In response to these inconsistencies, we applied a statistical method on regionally aggregated productivity data in four selected North

---

[1] Published as Butterfield, Z., Buermann, W., & Keppel-Aleks, G. (2020) in *Remote Sensing of Environment*, *242*, 111755.

American ecoregions and identified two dominant modes of IAV—seasonal redistribution and amplification—that were consistent across satellite datasets. The seasonal redistribution mode, which played a stronger role at lower latitudes, associated high (low) spring productivity with warm (cold) spring and summer temperatures, but also with lower (higher) productivity and water availability in summer and fall, indicating that enhanced growth in spring may contribute to an earlier depletion of water resources. The amplification mode associated an increase (decrease) in productivity across the growing season with above-average (below-average) summer moisture conditions. Even though our statistical analysis at large spatial scales revealed meaningful links between terrestrial productivity and climate drivers, our analysis does suggest that IAV and long-term trends in presently available novel and more established satellite observations must be interpreted cautiously, with careful attention to the spatial scales at which a robust signal emerges.

2.1. Introduction

The terrestrial sink for anthropogenic CO_2 is about 30% of anthropogenic emissions (Le Quéré et al., 2018), but its sensitivity to interannual climate variations has implications for the long-term land carbon sink (Cox et al., 2013). While variations in the total land sink may arise from variations in productivity, respiration, or disturbance, quantifying interannual variability in ecosystem productivity is especially important, since vegetation photosynthesis represents the ultimate formation pathway for all carbon in above and below ground biomass (Running et al., 2004). Climate impacts on productivity can occur via coincident responses of vegetation to temperature and moisture. For example, Zhao and Running (2010) used global satellite observations and meteorological reanalysis data to show that large-scale droughts were the main cause of reduced annual productivity at the regional scale between 2000 and 2009, resulting in a 0.55 Pg C/y or 1% total decline in global net primary production (NPP). Climate can also induce lagged effects on ecosystem productivity later in the growing season. For example, several studies have suggested that earlier spring leaf out is followed by decreased summer productivity in northern boreal forests (Buermann et al., 2018, 2013), likely because earlier growth can coincide with conditions (e.g. shallow snowpack) that lead to drought later in the year (Richardson et al., 2010) or contribute to earlier depletion of water resources through increases in evapotranspiration (Payne et al., 2004). In addition to decreased summer productivity, water stress can also prompt earlier senescence in some ecosystems (Piao et al., 2007). Such relationships may act as a stabilizing mechanism to damp the growing season integrated response to climate variability, since high (low) productivity in spring is compensated for by low (high) productivity in late summer and fall.

Space-based estimates of ecosystem productivity provide data across heterogeneous ecosystems and climate zones. Longstanding observations of vegetation indices (VIs), which combine spectral radiances at different wavelengths, have been used to infer ecosystem productivity at seasonal, interannual, and decadal timescales (Guay et al., 2015; Huete et al., 2002; Running et al., 2004). For example, NDVI quantifies the difference in surface reflectivity between wavelengths in the red and near infrared, providing a measure of vegetation greenness (Running et al., 2004). Since the NDVI record began in1981, with the early generations of the Advanced Very High Resolution Radiometer (AVHRR) instruments (Guay et al., 2015), these satellite observations have provided substantial insight into the links between climate variations and vegetation productivity (e.g. Buermann et al., 2018, 2013; Nemani et al., 2003; Zhou et al., 2001).

Although VIs capture the absorbed fraction of photosynthetically active radiation in plant canopies (Running et al., 2004), they provide limited information related to the efficiency at which that light is used for photochemical processes (Rossini et al., 2015; Yang et al., 2015). In fact, previous studies have indicated that photosynthesis and carbon uptake may shut down prior to changes in chlorophyll content (as inferred from NDVI) due to other limiting factors (Eitel et al., 2011; Walther et al., 2016). A recent study has proposed a modified VI from the product of NDVI and near-infrared reflectance, deemed NIR_V, to estimate GPP (Badgley et al., 2017). This and other studies indicate that the NIR_V may be more directly related to plant photosynthesis than NDVI alone (Badgley et al., 2017; see also Sellers, 1987, 1985; Sellers et al., 1992)

Novel observations of SIF may provide information that is directly related to photosynthetic processes (Frankenberg et al., 2011; Guanter et al., 2012; Joiner et al., 2011). As plants absorb sunlight, the absorbed photons can be used to drive photochemistry (photosynthesis), radiated as heat, or re-emitted back to the environment as far-red and near-infrared fluorescence (Baker, 2008) which can be detected by satellites. Satellite-based SIF observations are now available from several sensors, including GOSAT (Guanter et al., 2012), SCIAMACHY (Joiner et al., 2012), GOME-2 (Joiner et al., 2013), OCO-2 (Frankenberg et al., 2014), and TROPOMI (Köhler et al., 2018). Several studies have verified that SIF observations are proportional to GPP for similar vegetation types at diurnal and seasonal timescales, and that SIF observations provide information about light use efficiency (LUE; Guanter et al., 2014; Sun et al., 2017; Yang et al., 2015; Zhang et al., 2016). While initial results assessing the relationship between SIF and GPP are promising (Li et al., 2018), there are potential complications in using the data to infer vegetation productivity. Because above-canopy SIF is dependent on leaf and canopy structure, the conversion from SIF to GPP is dependent on the type of vegetation being observed (e.g. Frankenberg et al., 2011; Guanter et al., 2014; Sun et al., 2017). Additionally, vegetation stress, such as that introduced by interannual climate variations, can introduce nonlinearities into the relationship between SIF and GPP that require further assessment (Van der Tol et al., 2014). Finally, uncertainties in SIF (as well as VI) IAV may also arise from atmospheric disturbances and limited sensor capabilities (Koren et al., 2018).

Given the promise, but also the potential limitations, of SIF observations, it is necessary to probe variations in SIF across a broader range of timescales. To this point, many studies comparing VIs and SIF have focused on differences at intraseasonal or seasonal timescales (e.g. Jeong et al., 2017; Walther et al., 2016) while fewer have examined interannual timescales (e.g. Koren et al., 2018; Song et al., 2018). These studies have demonstrated a large-scale decoupling of SIF and NDVI across deciduous and evergreen forests in boreal and temperate ecosystems during the beginning and end of the growing season, which in part may be explained by initial leaf growth preceding the beginning of photosynthesis in the spring, and the ramping down of photosynthesis that precedes changes in leaf coloration in the fall (Jeong et al., 2017; Walther et al., 2016). Yoshida et al. (2015) also showed a faster autumn decline in SIF relative to NDVI in several ecosystems including mixed forest and cropland, likely due to decreasing leaf photosynthetic capacity that does not affect the spectral information used to calculate VIs (see also Bauerle et al., 2012). At interannual timescales, SIF-based studies are more limited and have primarily focused on large-scale droughts, but have demonstrated that SIF successfully tracks extreme drought impacts in cropland, mixed forest, and tropical forest (Koren et al., 2018; Song et al., 2018; Yoshida et al., 2015).

In this study, we examined IAV in both novel (SIF, NIRv) and traditional (NDVI) satellite-based metrics of plant productivity and evaluated their consistency with GPP data from eddy covariance flux towers. Our work was premised on the hypothesis that the demonstrated seasonal differences among remote sensing metrics will carry forward to interannual timescales, and that inferences about IAV in productivity will be quantitatively different across remote sensing datasets. While our study domain spanned the northern hemisphere, we examined the relatively well-studied temperate and boreal North American forests as well as North American croplands in more detail to get additional insights at the regional scale.

The objectives of our analysis are to first explore the potential for novel observations of SIF to be used for constraining IAV in productivity, and to assess how SIF compares to longer standing optical satellite data and in situ flux observations. Second, we explore how IAV in productivity as measured by satellite remote sensing relates to variability in climate drivers, including temperature and moisture. Third, we look at how relationships between climate anomalies and productivity change over the course of a growing season, and quantify the growing season integrated effect of these relationships on plant productivity. Additionally, we introduce a statistical method (Singular Vector Decomposition, SVD) through which we quantified the influence of climate drivers on IAV in the satellite vegetation data.

2.2. Data and Methods

2.2.1. Data

We analyzed several datasets, including remote sensing, eddy covariance flux, and climate observations. We applied a consistent method to calculate IAV in each of these datasets, by first linearly detrending and second removing a mean annual cycle from each timeseries. Because the satellite datasets studied have different native spatial resolutions, we averaged finer scale data to that of the coarsest resolution dataset for the relevant analysis. Descriptions of each dataset and its treatment (including rationale for the spatial scale of the analysis) are provided below.

2.2.1.1. Solar-Induced Chlorophyll Fluorescence

We used SIF data from the Global Ozone Monitoring Experiment (GOME-2) aboard the MetOp-A satellite (Joiner et al., 2013), which launched in October 2006 and provides the longest satellite-derived SIF dataset to date. The GOME-2 instrument is an optical spectrometer and scan mirror that measures in the 240-790nm spectral range at a resolution of 0.2-0.5 nm (www.eumetsat.int/website/home/Satellites/CurrentSatellites/Metop/MetopDesign/GOME2/index.html; Munro et al., 2006). GOME-2 aboard MetOp-A has an overpass time of 9:30 local time and achieves global coverage every 1.5 days (Loyola et al., 2011; Munro et al., 2006) with a 40x80 km footprint before July 15, 2013 and a 40x40 km footprint afterwards. While more recent satellite instruments obtain SIF observations at improved spatial and temporal resolutions, GOME-2 currently provides the highest quality observations across timespans suitable for studies of IAV.

We used the daily average SIF from the level 3 data product, in which the 9:30 AM sounding has been converted to a daily average using a simple clear sky photosynthetically active radiation (PAR) proxy to account for diurnal variability in SIF. The clear sky PAR proxy is based on the cosine of the solar zenith angle at the time of observation weighted against the full day. The L3 data were provided in a 0.5° resolution grid of daily-averaged monthly values referenced to 740nm (avdc.gsfc.nasa.gov/pub/data/satellite/MetOp/GOME_F/README_GOME-F_v27.pdf; Joiner et al., 2013). In the Northern Hemisphere ecoregions we analyzed, the 0.5° grid cells typically contain 10-25 soundings, and grid cell level error is estimated to be 0.1-0.4 $mW/m^2/nm/sr$ (Joiner et al., 2013). As the GOME-2 instrument suffers from a long-term radiometric degradation (Joiner et al., 2016), we linearly detrended the data (Section 2.2.2) to minimize influence from this drift or other long-term changes. While we note that this degradation is not linear over time, the use of a more complex drift correction method did not significantly affect our results. For consistency, we similarly removed a linear trend from all other datasets.

2.2.1.2. Vegetation Indices

We analyzed NDVI and NIR_V for comparison with SIF observations. NDVI represents the differences between reflected red and near-infrared (NIR) wavelengths and thus is a measure of chlorophyll absorption (Running et al., 2004). NDVI has been used extensively in models for terrestrial uptake (Running and Zhao, 2015; Schaefer et al., 2008), and can be related to GPP via scaling with available sunlight and a light-use efficiency factor that is dependent on both vegetation and climate factors (Running et al., 2004). NIR_V represents the near infrared reflectance from vegetation and a recent study has shown that this metric may be more directly related to GPP than more traditional VIs (Badgley et al., 2017). NIR_V is calculated as

$$NIR_V = (NDVI - 0.08) \times NIR_T \qquad (2.1)$$

where NDVI is offset by 0.08 to account for the signal from the bare soil and NIR_T represents total near infrared reflectance.

We used NDVI and NIR_V data from the Moderate Resolution Imaging Spectroradiometer (MODIS), which launched aboard the Terra Satellite in 1999. MODIS has a 2330-km-wide viewing swath with 250 m horizontal resolution, resulting in global coverage every 1-2 days. For this study, we used the MOD13C2 Versions 6 product that consists of 16 day composites with a native spatial resolution of 0.05° (Didan, 2015).

We also analyzed NDVI derived from AVHRR, as several studies suggest different seasonal patterns between MODIS and AVHRR NDVI (e.g. Walther et al., 2016). Several generations of AVHRR instruments have resided aboard NOAA satellites, the first launching in 1981, and observe Earth's surface using five spectral bands. We used data calculated from the third generation Global Inventory Modeling and Mapping Studies (GIMMS 3g) dataset (Pinzon and Tucker, 2014) that combines observations from multiple generations of AVHRR sensors to produce a long-term (1982-2015) NDVI dataset. The original bi-monthly data were available at a resolution of 8 km.

2.2.1.3. Eddy Covariance Flux Data

To compare the satellite datasets with ground observations, we analyzed GPP data from FLUXNET2015 (Baldocchi et al., 2001; Pastorello et al., 2017) at 12 sites from North America and Europe comprising deciduous broadleaf forest (DBF), evergreen needle leaf forest (ENF), and mixed forest (MF) locations. These datasets reflect a flux footprint around 1-5 km^2 (Chen et al., 2011). We analyzed sites with at least six years of data during the 2007-2014 period, whereby all but two sites encompassed the full eight growing seasons within this timespan. FLUXNET2015 provides GPP estimates using daytime (DT) and nighttime (NT) partitioning methods to separate the GPP and ecosystem respiration signals imbedded within the measured net ecosystem exchange (Lasslop et al., 2010; Reichstein et al., 2005; Wohlfahrt and Galvagno, 2017). We analyzed correlations between satellite plant productivity and FLUXNET GPP using both the DT and NT partitioning, but show primarily results for NT GPP since the results were qualitatively similar.

2.2.1.4. Climate Datasets

We explored relationships between the productivity metrics described above and climate variables using surface temperature data from the Hadley Center Climate Research Unit Timeseries (CRU-TS v. 4.00; Harris et al., 2014). The CRU-TS dataset interpolates surface temperature observed at meteorological stations into a monthly 0.5° resolution global grid.

We accounted for moisture stress using terrestrial water storage (TWS) data from GRACE (Swenson and Wahr, 2006; Swenson, 2012). The GRACE mission consisted of twin satellites, active from March 2002 through October 2017, that mapped changes in terrestrial water resources by detecting changes in gravity. GRACE data are available at 1° resolution and near monthly timescales as an anomaly in TWS thickness using the 2004-2009 mean as a baseline (Landerer and Swenson, 2012; Swenson and Wahr, 2006; Swenson, 2012). While GRACE observations are sensitive to any changes in ground water, including water below the root zone, they are inherently linked to water fluxes dominated by precipitation, runoff, and evapotranspiration (Long et al., 2014; Swann and Koven, 2017), and have been used by a number of studies to assess dynamics between soil moisture and vegetation (e.g. Green et al., 2019; Guan et al., 2015; Humphrey et al., 2018; Long et al., 2013; Zhang et al., 2015). As forest ecosystems have complex root systems that can access deeper groundwater (Domec et al., 2015; Nepstad et al., 1994; Penuelas and Filella, 2003), GRACE may provide an advantage over microwave remote sensing products for surface soil moisture, which are typically only sensitive to the top few centimeters (Lv et al., 2018) and are further limited within forest ecosystems due to high canopy moisture content (Wigneron et al., 2017).

2.2.2. Methods

2.2.2.1. Timeseries Analysis

For the site-level comparisons between satellite SIF, NDVI, and NIRv and FLUXNET2015 data, we calculated IAV by first detrending all datasets (flux tower and satellite data) across the 2007-2014 study period. We then calculated monthly anomalies for each dataset by subtracting the eight-year mean annual cycle. In a next step, we defined single seasons within the vegetation growth period using a monthly 0° C temperature threshold (for start of spring and end of fall), and a threshold of 85% of maximum monthly tower-based GPP (for start and end of summer). When this definition resulted in spring and fall seasons longer than three months, we further constrained spring (fall) to the latest (earliest) three months. For example, if the mean monthly temperature reached 0° C in February but GPP did not reach 85% of its maximum value until June, spring was defined as March-May instead of February-May. We then aggregated satellite data to a 0.5° resolution, the original resolution of the gridded GOME-2 SIF dataset, by averaging together pixels of higher resolution datasets. Finally, we calculated seasonal and annual correlation coefficients for flux tower GPP IAV with the respective satellite observations. Because the timeseries overlapped for a relatively short period, we used $p<0.10$ to indicate statistically significant correlations throughout the manuscript.

2.2.2.2. Regional Analysis

We analyzed vegetation productivity IAV and links to climate factors in four representative ecoregions in North America (Fig. B1) in order to explore more robust large-scale patterns (through suppressing observational noise and localized anomalies). For regional (and subsequent) analysis, we regridded all data to a common 1°x1° grid, which was limited by the resolution of GRACE data, by simply averaging higher resolution data. While this scale of spatial resolution did not allow for local-scale analysis of ecosystem productivity, analysis of productivity at larger spatial scales is relevant for comparison with CO_2 observations (which reflect regional patterns of net carbon exchange) or carbon cycle models that generally have similar spatial resolution. We constrained the regions both geographically (maximum extent of 5° latitude and 10° longitude) and by land cover type (see below) in order to isolate signals from relatively homogeneous climate and ecosystem conditions. We included two contrasting North American forest regions: temperate mixed forest (43°-48° N, 84°-94° W) and boreal coniferous forest (54°-59° N, 94°-104° W). Both regions have been the focus of previous studies aimed at understanding ecosystem carbon responses to climate conditions (e.g. Kimball et al., 1997; Noormets et al., 2008). For comparison with land cover types where SIF has been more extensively studied, we also included two cropland regions: Midwest cropland (39°-44° N, 86°-

96° W), which is largely corn and soy, and Canadian Great Plains (50°-55° N, 105°-115° W), which is largely wheat. Carbon uptake in the Midwest cropland region has been previously studied using methods including satellite SIF observations (Guanter et al., 2014; Yongguang Zhang et al., 2018) and atmospheric inversion studies (Lauvaux et al., 2012). The Canadian Great Plains region provided a second crop-dominated region, but is colder and drier than the other crop region and thus vegetation may experience different interannual climate stressors. We note that IAV in crop productivity may result from climate variability and variations in management practices that are themselves tied to climate conditions (e.g. Grassini et al., 2009; Porter and Semenov, 2005). We also note that the aggregation of observations into larger ecoregions insulates IAV signals from abrupt changes due to crop management (e.g. harvest), as regional averages will reflect the average of heterogeneous local patterns.

For each region, we masked for the vegetation type of interest using the 1° AVHRR Land Cover Classification (Hansen et al., 1998). Thus, while the entire temperate mixed forest region spanned the latitude and longitude listed above, the regional average was comprised only of satellite vegetation data from the 1°x1° grid cells that were predominantly mixed forest and woodland. Similarly, we masked the boreal coniferous forest region to only include coniferous forest and woodland, and the two cropland regions to only include crops (see Fig. B1). After masking for the respective land cover type, each region encompassed at least 70% of the 1°x1° pixels within the respective 5°x10° area.

The GOME-2 SIF record overlapped with other satellite datasets from 2007 through 2015, so we limited the regional analysis to this nine-year period. We calculated IAV as described for the FLUXNET data (Section 2.2.2.1), but applied this method to the regional average of all grid cells. This same method was used to calculate detrended monthly anomalies in the CRU-TS temperature and in GRACE TWS. Finally, we defined the growing season for each region based on months with mean average temperature above 0° C. This resulted in a growing season of March though November for Midwest cropland, April through November for temperate mixed forest, April through October for Canadian Great Plains, and May through October for boreal coniferous forest. To define summer months, we also used a similar methodology as described in Section 2.2.2.1, except that we used an 85% SIF threshold in place of GPP (Table B1).

2.2.2.3. Singular Value Decomposition

We analyzed the patterns of IAV and their relationship to climate drivers using an SVD method (Golub and Reinsch, 1971) that allows for the holistic examination of interannual variations across a full growing season. We used the SVD method to decompose the multi-year, monthly resolution IAV timeseries from vegetation data into weighted sums of orthogonal modes, called singular vectors (SVs). In our case, the elements of any given SV reflect the month of the growing season, and all SVs are ranked based on the fraction of variance in the original timeseries that they explain. The weights (w_i) resulting from this decomposition, one per year per SV, quantify the contribution from an individual SV ($\mathbf{SV_i}$) to the observed IAV in any given year. Thus the observed IAV timeseries can be fully reconstructed as a weighted sum of singular vectors:

$$\mathbf{IAV}(y,m) = w_1(y) \times \mathbf{SV_1}(m) + w_2(y) \times \mathbf{SV_2}(m) + \ldots \qquad (2.2)$$

where, for a given year (y), **IAV** and **SV_i** are vectors resolved by month (m) of year and w_i are scalars (see Fig. B2). We analyzed the two most common modes of IAV represented by the first two SVs, which accounted for roughly 80-90% of the variance.

Using SVD to isolate dominant modes of variability allowed us to extract meaningful patterns from noisy satellite vegetation data and to identify emergent behaviors across the growing season that are representative of interannual variability. This statistical analysis also made it possible to examine the influence of climate on IAV by correlating temperature and moisture anomalies with the annual SV weights.

2.2.2.4. Redistribution Metric

To quantify the extent to which observed and decomposed anomalies represented a redistribution of productivity within the growing season, as opposed to a more uniform net increase or decrease in productivity, we calculated a metric for redistribution potential (θ) based on monthly satellite (**S**) anomalies:

$$\theta = \frac{\sum_m \boldsymbol{S}(m)}{\sum_m |\boldsymbol{S}(m)|} \tag{2.3}$$

where the summations act on a timeseries of IAV that covers a single growing season. In our analysis, we applied this equation in two ways: (1) for the SVD analysis, we separately applied Equation 2.3 to the first two SVs (i.e., **SV_1** and **SV_2** were substituted for **S** in Equation 2.3) in order to quantify the impact of particular modes on integrated growing season productivity; (2) we applied Equation 2.3 to pixel-level IAV observations throughout the Northern Hemisphere (e.g., **IAV** was substituted for **S** in Equation 3), discussed below. For both cases, a θ value of 0 indicated that productivity was simply redistributed within the growing season without a net change in productivity when integrated across the growing season. In contrast, θ = 1 indicated that the vector represented a consistent positive anomaly in productivity across all months of the growing season relative to the multi-year mean, while θ = -1 indicated a consistent negative anomaly across all months. This metric allowed us to categorize the modes resulting from SVD analysis as either primarily seasonal redistribution or seasonal amplification.

To assess large-scale spatial patterns in redistribution versus amplification throughout the Northern Hemisphere, we calculated θ from the observed IAV timeseries (independent from SVD results) at each 1°x1° pixel. We then categorized pixels as either predominantly forest or grassland and calculated the root mean square of θ across all pixels of a given landcover type for individual latitudinal bands. Since the root mean square is only influenced by the absolute value of θ across pixels, the zonal result indicated whether seasonal amplification (either positive or negative) or seasonal redistribution predominated within a given latitude band.

2.3. Results

2.3.1. Local IAV in Satellite Vegetation Data and Comparison with GPP Flux Tower Data

In a first step, we compared year-to-year correlations between SIF, VIs, and GPP derived from eddy covariance flux tower measurements at twelve North American and European flux tower sites encapsulating evergreen, deciduous, and mixed forests. For the most part, neither SIF nor MODIS NDVI showed a significant correlation with field-based GPP when integrated over the growing season at a 0.5° spatial scale (Fig. 2.1a). In general, SIF was better correlated with GPP in deciduous broadleaf forests, whereas the NDVI-GPP correlations did not exhibit clear differences between forest types (Fig. 2.1a). However, in the case for SIF, robust correlations (p<0.1) with GPP were only found for two sites, whereas for NDVI-GPP links none were statistically robust (Fig. 2.1a). The site-level correlations with eddy covariance GPP were more

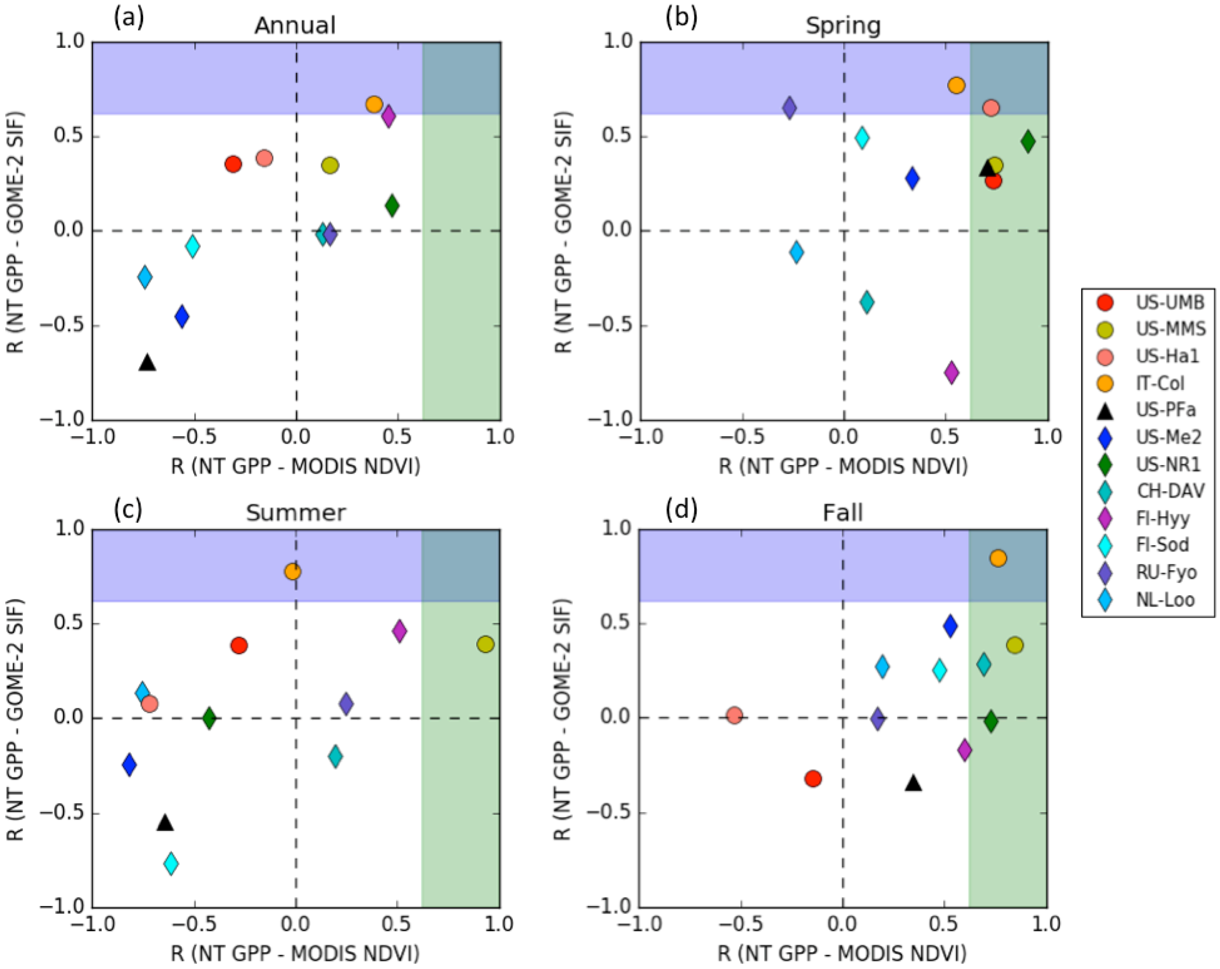

Fig. 2.1. Correlation coefficients of interannual anomalies in FLUXNET NT GPP against those from GOME-2 SIF and MODIS NDVI. Satellite data were averaged over a 0.5° grid cell containing the respective FLUXNET site at annual (a) and seasonal (b-d) timescales from 2007 through 2014. Spring, summer, and fall seasons are defined by using a 0° C temperature threshold to determine the beginning of spring and end of fall, and an 85% GPP threshold to determine summer months. Round symbols indicate sites in deciduous broadleaf forest, diamonds indicate evergreen needleleaf forest, and triangles indicate mixed forest. Shaded regions indicate statistically significant (p<0.1) positive correlations.

robust for both SIF and NDVI in spring (Fig. 2.1b), as compared to annual or summer seasons (Fig. 2.1a, c). For fall, site-level correlations for SIF were generally lower than site-level correlations for NDVI (Fig. 2.1d). The low correlations between SIF and GPP may have resulted from the relatively low precision of SIF data (as high as 0.4 mW m^{-2} sr^{-1} nm^{-1} for 0.5° grid cells; Joiner et al., 2013). Additionally, due to a larger footprint size and different sensor characteristics, gridded GOME-2 data are more strongly influenced by conditions outside pixel boundaries. For the 0.5° gridded data, we used a Monte Carlo approach to estimate that at 45° latitude about 39% (for 40km x 40km soundings obtained after July 2013) or 60% (for 40km x 80km soundings obtained prior to July 2013) of the signal from an individual pixel may originate from surrounding pixels. For 1.0° gridded data these influences decrease to 21% and 33%, respectively (see Table B2). Outside-pixel influences largely disappear for MODIS data at spatial resolutions larger than 10km (Weiss et al., 2007). Taken together, these results indicated that the interannually varying component of the SIF signal was within the noise of the observations for a 0.5° grid cell, an issue that may be alleviated by spatially averaging GOME-2 SIF observations. Comparisons of tower-based GPP with AVHRR NDVI and MODIS NIR_V yielded qualitatively similar results as with MODIS NDVI (Fig. 2.1, B3, B4).

Since estimating formal uncertainties for IAV in satellite and FLUXNET signals entails high uncertainty due to systematic covariances between climate factors that both affect variations in productivity and influence the observation (e.g., IAV in cloud cover), we instead ran several sensitivity studies to demonstrate the robustness of our results. We first tested the robustness of the correlations between satellite and tower-based productivity measures against uncertainties in FLUXNET GPP, by using an alternative GPP estimate (calculated using the DT partitioning algorithm; e.g. Lasslop et al., 2010). Based on this DT GPP, we found that across all sites, the correlation coefficients shifted by +/-0.15 for NDVI and by +/-0.2 for SIF (relative to the results based on NT GPP) and that correlations at individual sites were mostly weak as well ($p>0.1$).

These results suggest that the correlations between satellite data and eddy covariance data were sensitive not only to the characteristics of the satellite dataset, but also to uncertainties in the eddy covariance data themselves (Fig. B5). As such, comparison with eddy covariance GPP did not provide a definitive answer as to which satellite product most accurately tracks IAV in productivity in temperate and boreal forests.

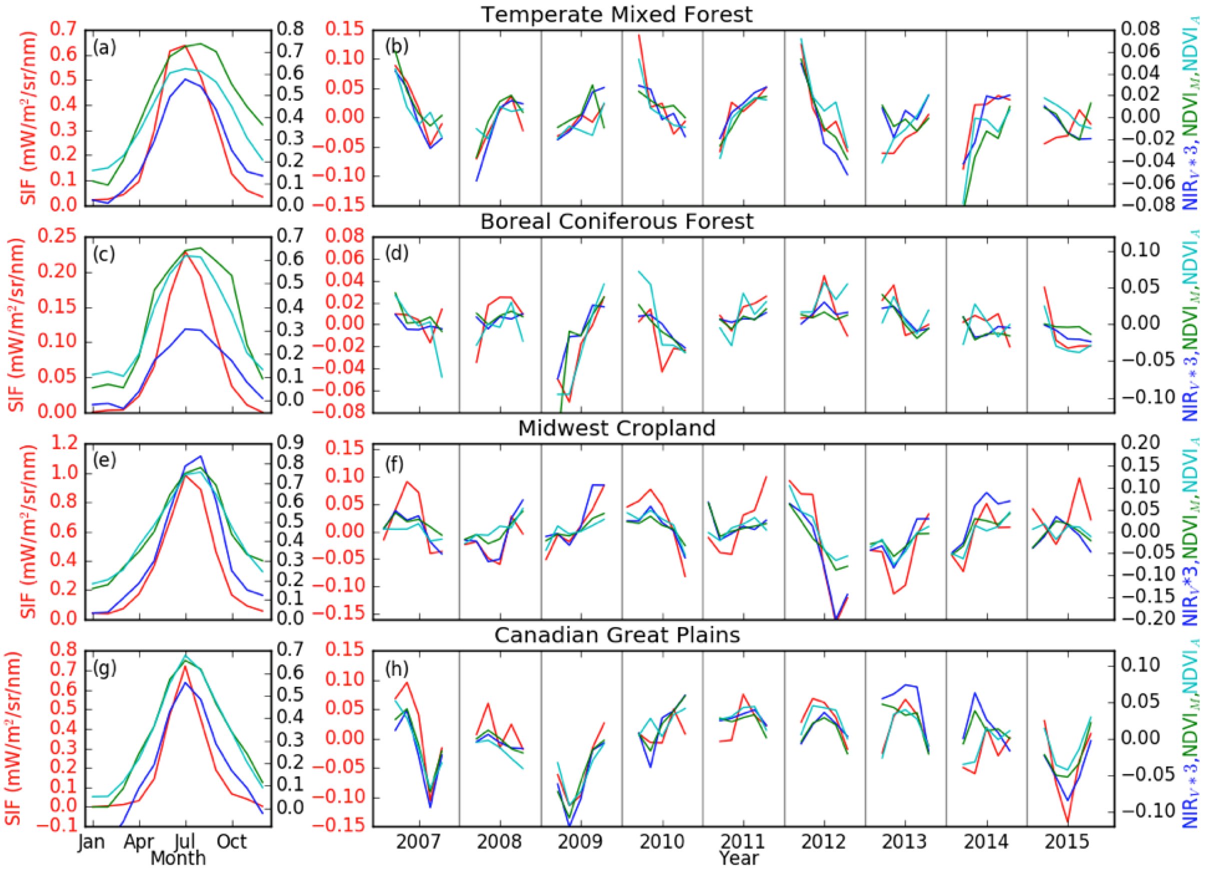

Fig. 2.2. Multi-year mean annual cycles (left) and interannual monthly anomalies, relative to the multi-year mean annual cycle, from 2007 through 2015 (right) for (a-b) Temperate Mixed Forest, (c-d) Boreal Coniferous Forest, (e-f) Midwest Cropland, and (g-h) Canadian Great Plains. Growing seasons are defined using a 0° C temperature threshold. SIF (red) corresponds with the axes on the left, while MODIS NIR_V (blue), MODIS NDVI (green), and AVHRR NDVI (teal) correspond with the axes on the right. Note that y-axis limits vary by region and that NIR_V is multiplied by a factor of three.

We note that using eddy covariance GPP as ground truth presented challenges since the flux footprint for these towers is about 1 km^2, substantially smaller than the 0.5° resolution at which SIF are available, and that the spatial mismatch between the datasets increases as the satellite data are aggregated to larger spatial scales. We therefore also tested correlations of satellite observations with FLUXCOM GPP (Jung et al., 2017), which uses machine learning algorithms with satellite and meteorological data in order to scale tower-based GPP to a global grid, at each of the twelve flux tower sites. As the FLUXCOM data are available through 2013, this analysis covered the seven-year 2007-2013 timespan. Relative to FLUXNET GPP, the upscaled FLUXCOM GPP showed weaker correlations with both GOME-2 SIF and MODIS NDVI during spring, and had limited impact on GOME-2 SIF correlations during other seasons (Fig. B6). Correlations of MODIS NDVI with FLUXCOM GPP for summer, fall, and annual timescales were stronger than with FLUXNET GPP, but most correlations remained statistically weak ($p>0.1$). The mostly insignificant ($p>0.1$) correlations of satellite observations with both FLUXNET and FLUXCOM GPP products highlight the difficult nature of validating satellite observations of vegetation at interannual timescales with independent ground-based data.

2.3.2. Regional Patterns of IAV in Satellite Vegetation Data

As a next step, we analyzed IAV of regionally aggregated satellite vegetation data in an attempt to overcome the noise in GOME-2 SIF that was apparent at fine scales. Through regional aggregation, we expected that the signal-to-noise ratio of the IAV would improve for all datasets by damping random noise, but we note that the magnitude of seasonal mean IAV was still small relative to the multi-year mean annual cycle of the respective satellite vegetation timeseries (Fig. 2.2), with coefficients of variation generally less than 3% (calculated as the ratio of the interannual standard deviation to the seasonal peak-to-trough amplitude; Table B3).

At the four focus regions, IAV among the four datasets was generally better correlated at seasonal timescales than it was when integrated over the entire growing season (Fig. 2.3). In

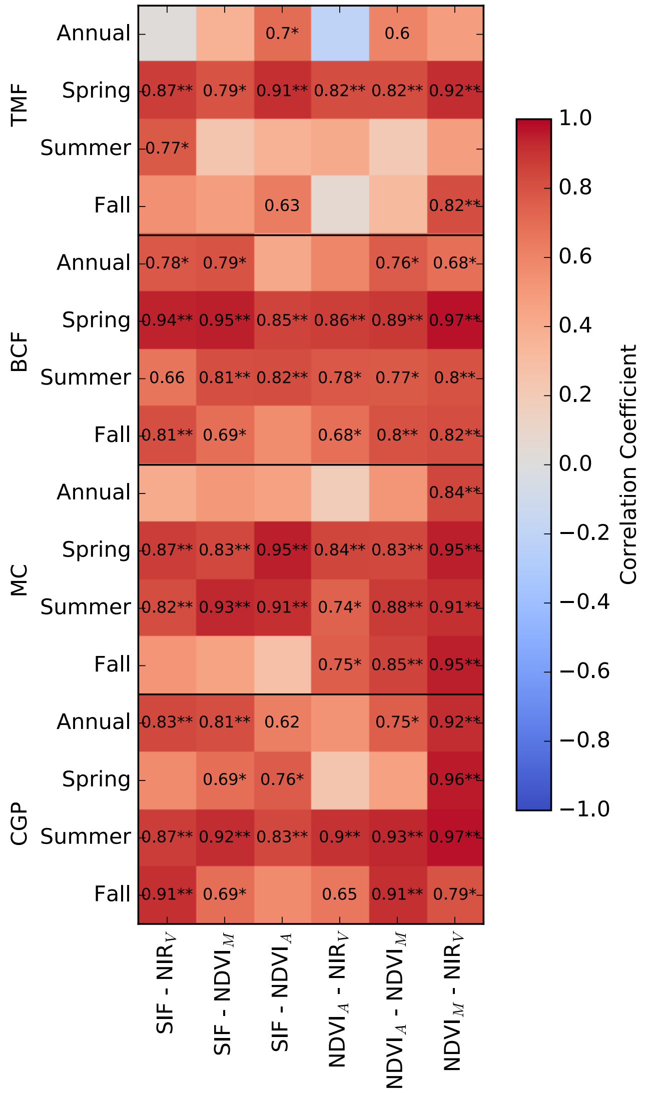

Fig. 2.3. Correlation coefficients for annual and seasonal anomalies between GOME-2 SIF, MODIS NIR$_V$, MODIS NDVI, and AVHRR NDVI in the four focus regions: Temperate Mixed Forest (TMF), Boreal Coniferous Forest (BCF), Midwest Cropland (MC), and Canadian Great Plains (CGP). Spring, summer, and fall seasons are defined by using a 0° C temperature threshold to determine the beginning of spring and end of fall, and an 85% SIF threshold to determine summer months. Numbers within grid cells indicate statistically significant correlation coefficients with $p<0.1$, single asterisks indicate $p<0.05$, and double asterisks indicate $p<0.01$.

three of the four regions (Midwest cropland and forest regions), correlation patterns of IAV among all datasets were robust in spring ($p<0.1$). In the cropland and boreal forest regions, summer and fall correlations among the datasets were also mostly robust ($p<0.1$). Surprisingly, when integrated over the growing season, the datasets were often not well correlated even in cases when the data showed robust links in individual seasons. This likely occurred because seasonal anomalies offset one another (e.g., above average productivity in spring is followed by below average productivity in fall, discussed in more detail in Section 2.4.2), leading to a low magnitude in growing season IAV that, again, may fall within the noise of even the regionally averaged signal. For the four study regions, the two MODIS datasets (NDVI and NIRv) were more highly correlated with each other than were the two NDVI products based on MODIS and AVHRR (Fig. 2.3). Similarly, Badgley et al. (2017) showed that GOME-2 SIF and MODIS NIR_V exhibited much weaker correlation than did GOME-2 SIF and GOME-2 NIR_V (their Figures 1b and S5b), although that study focused on absolute signals rather than IAV.

2.3.3. Mode Decomposition of Regional IAV in Satellite Vegetation Data

Given the exposed inconsistencies in the IAV at local to regional scales in both novel and long-standing satellite vegetation data, we applied a statistical method (SVD; Section 2.2.2.3) to isolate and compare dominant modes of IAV in these datasets and to further investigate links to climate drivers. This analysis revealed two dominant modes of IAV that were remarkably consistent across the satellite datasets: (1) redistribution of productivity within the growing season and (2) net amplification (which either increases or decreases the amplitude of the seasonal cycle, depending on the sign of the weight) of the mean annual cycle (Fig. 2.4). The shape of the redistribution mode of IAV typically resembled a sinusoid with the positive lobe centered over spring, and the negative lobe centered over late summer (or vice versa), meaning that a more (or less) productive spring is followed by a less (or more) productive late summer.

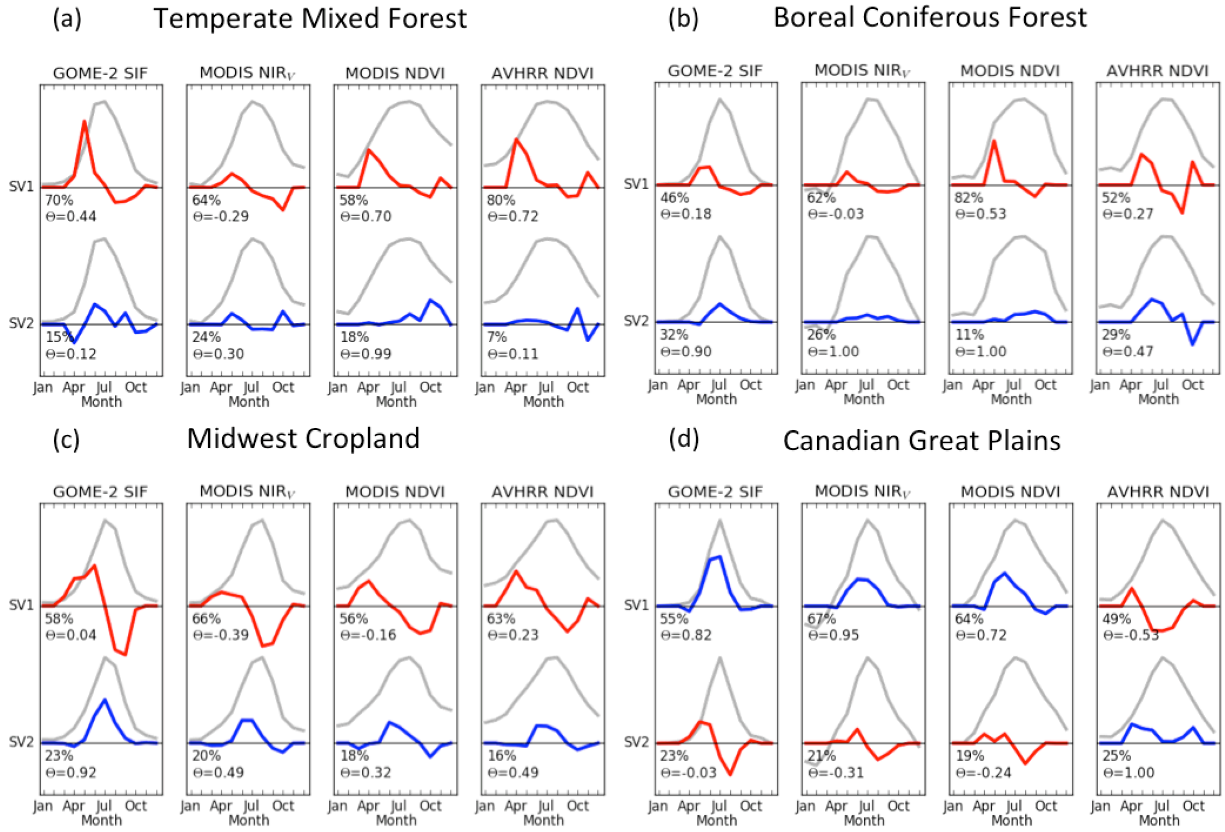

Fig. 2.4. First and second singular vectors resulting from the decomposition of the interannual variability in the (a) Temperate Mixed Forest, (b) Boreal Coniferous Forest, (c) Midwest Cropland, and (d) Canadian Great Plains regions using GOME-2 SIF, MODIS NIR$_V$ and NDVI, and AVHRR NDVI. Gray lines show the multi-year mean annual cycle. Red vectors indicate a temporal redistribution of productivity within the growing season, while blue vectors usually indicate an amplification of peak seasonal signal. The magnitude of the singular vectors are arbitrary, but each singular vector has an associated percentage of interannual variability that is described by the respective vector, and a θ value that indicates net impact on the integrated seasonal signal.

We found that this mode accounted for nearly half or more of the IAV signal in three of the four focus regions (the two forest regions and Midwest cropland; Fig. 2.4). Over the Canadian Great Plains region, redistribution of productivity within the growing season accounted for about 20% of the IAV signal. Redistribution of productivity has been noted previously; for example, Buermann et al. (2018) showed that across much of temperate and boreal ecosystems, anomalously high (low) spring productivity resulted in decreased (increased) productivity in summer and fall. Additionally, we found that at selected North American FLUXNET sites (encompassing temperate forest sites) seasonal redistribution of GPP was the primary driver of IAV and accounted for as much as 60% of the observed IAV (Fig. B7).

In order to quantify the balance of early versus late growing season anomalies, we defined a redistribution metric, θ, which takes a value of 0 if early season gains (losses) in productivity are perfectly balanced with late season losses (gains), but whose magnitude increases (or decreases) towards 1 (or -1) when productivity uniformly increases (or decreases) over the growing season (Section 2.2.2.4). For three of the four regions, we found that the magnitude of θ was less than about 0.2 for the SIF redistribution vectors (Fig. 2.4), meaning that enhanced productivity in spring was similar in magnitude to associated decreases during summer and fall. For the remaining temperate mixed forest region, the higher θ value (0.44; Fig. 2.4a) may indicate that this ecosystem can maintain photosynthetic activity later into the growing season despite higher early season productivity. Some subtle differences in these results with respect to choice of satellite vegetation data were observed. For example, both SIF and NDVI showed redistribution vectors with high (>0.44) θ values for the temperate mixed forest region, but MODIS NDVI was also large (0.53) in the boreal conifer forest region where the SIF redistribution vector was more balanced (Fig. 2.4b). The NIR_V redistribution vectors had θ values of less than 0.3 in both of these regions. In contrast, both cropland regions saw SIF redistribution vectors with low (<0.05) θ values while NIR_V saw values greater than 0.3. These differences may in part be due to different sensor characteristics (e.g. spatial and spectral resolution), differences in the observations themselves (SIF vs passive optical VIs), and effects of non-vegetation artifacts in the shoulder seasons (e.g. snow cover, see Beck et al., 2006).

Our SVD analysis also revealed a second dominant mode of IAV related to increases or decreases in the magnitude of seasonal productivity; in this mode of variability, the shape of the singular vector often resembled the shape of the mean annual cycle, with a peak in mid summer (e.g., Fig. 2.4c), indicating a more (or less) productive summer, independent from substantial behavior in shoulder seasons. In some cases, this SV had a large positive (negative) lobe during the peak summer growing period with smaller negative (positive) lobes in the shoulder seasons, indicating that this mode of variability was associated with either a highly seasonal summer peak or a lower, broader summer peak depending on the sign of the weighting value for any given year. In other cases, what we have assigned to be the "amplification" mode in Fig. 2.4 does not easily fit either of these two descriptions (e.g. VI results over temperate mixed forest; Fig. 2.4a). This lack of clear structure in the singular vectors potentially stems from saturation of the VI values over more dense canopies (Yang et al., 2015). For this mode of variability, θ values were generally closer to 1, indicating a consistent productivity increase (or decrease) throughout the growing season for any given year (e.g. Fig. 2.4c, d). The amplification mode of variability was the dominant mode of IAV only in the Canadian Great Plains region, consistent with this region showing relatively larger variability during mid-summer when compared to the other three focus regions (coefficient of variability of 4.1-9.4%; Table B3). In the other three focus regions, the fraction of IAV explained by this vector was smaller. For example, over forested regions, the amplification vector was not a significant contributor to IAV measured by VIs (fraction of IAV explained was less than 30%, Fig. 2.4a, b),

2.3.3.1. Climatic Drivers of IAV in Satellite Vegetation Data

To characterize the relationship of the seasonal redistribution and amplification modes of vegetation productivity to interannual variations in climate, we calculated correlations between the annual weights of these two dominant SVs and the anomalies in CRU-NCEP temperature and TWS from GRACE. As these annual weights quantify the influence of a specific SV for any given year (see Fig. B2), the correlations help to elucidate which season-specific climate anomalies drive productivity patterns across the growing season. We found that across all our four focal regions, above average temperatures in spring and summer were positively correlated

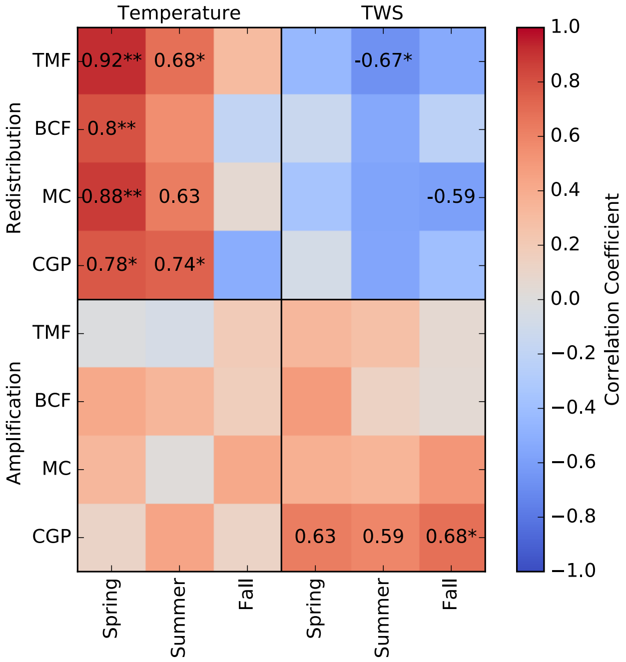

Fig. 2.5. Correlation coefficients between SIF redistribution and amplification vectors and seasonal climate anomalies in temperature and TWS for the Temperate Mixed Forest (TMF), Boreal Coniferous Forest (BCF), Midwest Cropland (MC), and Canadian Great Plains (CGP) regions. Red shading indicates that positive anomalies in temperature or moisture are positively correlated with redistribution of productivity towards earlier in the growing season (for Redistribution) or with an increase in peak growing season signal (for Amplification); blue shading indicates negative correlations. Numbers within grid cells indicate correlation coefficients with $p<0.1$, single asterisks indicate $p<0.05$, and double asterisks indicate $p<0.01$.

with the seasonal redistribution mode of IAV, which suggests that warming in the early part of the growing season is driving synchronous enhanced plant productivity that is linked to lower productivity in late summer and fall (Fig. 2.5 for SIF; Fig. B8 for VIs). The same seasonal redistribution mode was also negatively correlated with water availability (TWS) during summer (Fig. 2.5). These patterns of high spring and summer productivity and below-average summer TWS may be due to earlier and enhanced spring growth depleting soil water resources; in other words, rather than the climate anomaly driving a productivity anomaly, this pattern may indicate that early spring productivity can contribute to a low summer TWS anomaly. We note that the correlations between spring temperature and summer TWS anomalies themselves were statistically insignificant ($p>0.1$; Fig. B9). These interdependent relationships underscore the value in our SVD approach, which allowed for the holistic analysis of growing season patterns and did not treat productivity or climate variability as being independent across months. Additionally, that the links to climate anomalies show consistent patterns across both novel and long-standing vegetation datasets (Fig. 2.5, B8) highlights the strength of this SVD approach in unravelling common information about vegetation productivity.

Correlations between the amplification mode and TWS anomalies were predominantly positive across the study regions, suggesting that water limitations act as key constraint on integrated growing season productivity. This was especially true for the Canadian Great Plains, where moisture availability in summer and fall was positively correlated ($p<0.1$) with concurrent productivity (Fig. 2.5). The Canadian Great Plains is also the drier of the two crop regions in our study, with average annual precipitation of approximately 700 mm (Fig. B10). While the relationship between the amplification mode and TWS was less robust for the two forest regions, moisture and summer productivity were positively correlated across all regions (Fig. 2.5). In contrast, there was not a consistent significant relationship between the amplification mode and temperature (Fig. 2.5, B8). This could be reconciled by the fact that year-to-year variations in moisture might indeed be more important than those in temperature in modulating net gains or losses in integrated growing season productivity, while temperature limitations in these ecosystems are primarily limited to the shoulder seasons where ecosystem behavior is captured by the redistribution mode.

2.3.3.2. Zonal Characteristics of IAV in Satellite Vegetation Data

A zonal analysis of the multiple satellite vegetation datasets revealed that seasonal redistribution of productivity played a stronger role in the NH subtropical and midlatitude forests than in boreal forests, since the θ value (a measure of redistribution potential) of direct observations increased with latitude for both SIF and VI data (Fig. 2.6a). While this zonal pattern for forest was qualitatively consistent across datasets (Fig. 2.6a), spatial maps where θ was calculated for individual 1° pixels rather than aggregated across latitudinal bands did not show consistent patterns between SIF and VIs (Fig. B11). In addition, although the overall zonal patterns were similar, there was an offset in the zonal θ values among the three datasets, with SIF showing the greatest redistribution potential within the growing season (lower θ values; see Fig. 2.6a). These quantitative differences are important for inferences about climate-driven ecosystem variability, with the SIF-based analysis suggesting a greater role of seasonal redistribution, which acts as a damping mechanism on the impact of IAV in carbon uptake, in ecosystem response to IAV in climate.

A similar analysis for grasslands did not reveal the same meridional dependence in regards to seasonal redistribution potential that was seen over forests (Fig. 2.6). However, this analysis did also indicate a substantially higher redistribution potential based on SIF when compared to the NDVI based metrics especially in the Northern Hemisphere sub-tropics and midlatitudes (Fig. 2.6b). Further, a spatial analysis suggested that west-east gradients in climatological moisture may be also important in shaping the seasonal redistribution potential (Fig. B11 and B12). Among the four vegetation datasets (Fig. B11), this pattern is least clear for SIF, which we hypothesize reflects local noise in the SIF data, consistent with the FLUXNET comparison that revealed GOME-2 SIF data as being too noisy for inference of IAV at finer spatial resolutions.

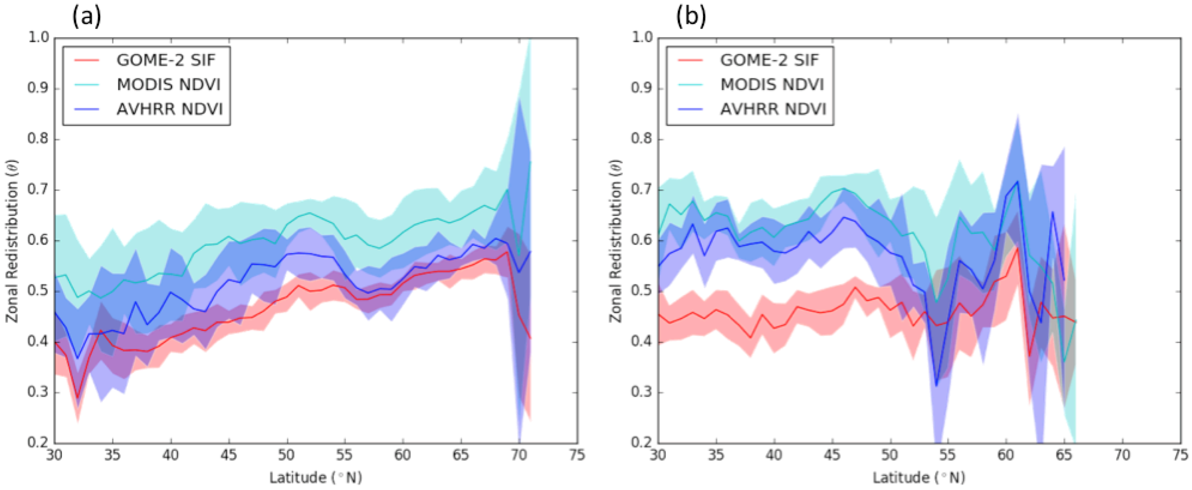

Fig. 2.6. The zonal root mean square of observational θ values at each 1° latitudinal band for (a) forested and (b) non-crop grassland grid cells. Solid lines represent the mean θ across the 2007-2015 timespan, while the shaded regions indicate ±1 standard deviation across the nine study years for GOME-2 SIF (red), MODIS NDVI (teal), and AVHRR NDVI (blue). Large spreads in standard deviation occur at latitudinal bands where the respective land type includes relatively few grid cells (> 65N).

2.4. Discussion

2.4.1. Potential for SIF to Quantify Interannual Variations in Productivity

While several studies have shown favorable comparisons between SIF and field-based GPP (Guanter et al., 2014; Sun et al., 2017; Yao Zhang et al., 2018), these studies generally leveraged the large seasonality of Northern Hemisphere fluxes. In this study, we focused on the interannually varying component of vegetation productivity to investigate how well diverse satellite observations track anomalies in productivity independent of seasonal dynamics. We note that other studies have shown that GOME-2 SIF observations respond to climate stress (Koren et al., 2018; Sun et al., 2015; Wu et al., 2018; Yoshida et al., 2015), but these analyses have primarily focused on extreme drought conditions. A key result of our study is that the GOME-2 SIF data were too noisy to meaningfully quantify typical levels of climate-driven IAV at spatial scales close to the native resolution of GOME-2. This assessment was based both on an evaluation against eddy covariance flux tower observations in Northern Hemisphere forests (e.g. Fig. 2.1) and a pixel-based analysis of seasonal redistribution as an important component of IAV (Fig. B11). However, the general consistency of the dominant seasonal redistribution and amplification modes of IAV across the four satellite datasets (Fig. 2.4), the broadly consistent links with climate drivers (Fig. 2.5, B8), as well as the zonal analysis on redistribution potential over forested regions (Fig. 2.6a) underscore that, even with relatively noisy satellite observations as a basis, it was possible to extract meaningful patterns and relationships through our SVD analysis. In the future, with SIF sensors such as TROPOMI (Köhler et al., 2018) and OCO-2 (Frankenberg et al., 2014) providing long-term data with improved signal-to-noise performances and at higher spatial and temporal resolutions it may be more feasible to validate SIF as a metric for IAV of ecosystem productivity. At present, however, these results may indicate a limited capacity for current satellite observing systems to record relatively small IAV signals at fine scale, with implications for trend analyses of satellite vegetation data where corresponding signals are even smaller (e.g. Xu et al., 2013).

At regional scales, IAV in SIF was often most highly correlated with IAV in other satellite metrics during spring. Previous studies showed that the mean annual cycle of NDVI in Northern Hemisphere forests was generally broader than that of SIF, with faster ramp up in spring and slower decline in fall (e.g. Jeong et al., 2017; Walther et al., 2016). We found, however, that these obvious differences at seasonal timescales did not necessarily translate to differences in IAV anomalies. Thus, even though the shape of the seasonal cycle differed with a relatively higher VI signal in the shoulder seasons, the interannually varying component of the signal was most highly correlated during these periods amongst the multiple satellite data. In contrast, peak-summer variability in temperate forests and annually integrated variability was not well correlated across the four analyzed remote sensing datasets, or when compared to flux tower based GPP. These results may reflect the dominant influence of seasonal redistribution, which had larger impacts (both absolute and relative) on productivity in the shoulder seasons, leading to a stronger interannual signal during these portions of the growing season, but also lend credence to studies such as Wohlfahrt et al. (2018) that question the relationship between SIF, GPP, and VIs during periods without significant changes in absorbed PAR. On the other hand, for regions such as the Canadian Great Plains where the amplification mode of variability was dominant, both peak summer and annually integrated IAV were well correlated across datasets.

2.4.2. Relationship of IAV to Climate Drivers

Based on our SVD analysis, we found that redistribution of productivity within the growing season was the dominant mode of IAV in the temperate and boreal ecosystems we analyzed. This mode is characterized by above-average spring productivity that was driven by high spring temperatures and was subsequently associated with below average summer and fall productivity as well as TWS. This pattern is consistent with the summer browning trend discussed by Wang et al. (2011) and Buermann et al. (2018, 2013), where earlier leaf out and greener springs were found to correlate with lower NDVI signals during summer and fall. Here, we used independent observations of TWS from GRACE and the holistic SVD analysis to show that the reduction in fall productivity may be self-induced via vegetation draw down of available soil water, contributing to increased evapotranspiration earlier in the growing season (Barnett et al., 2005; Parida and Buermann, 2014), consistent with lower available moisture in the late summer and fall as measured by GRACE. Conversely, we found that below-average spring productivity due to low spring temperatures was associated with above-average productivity later in the growing season as ecosystems ramped up photosynthesis to meet their annual carbon requirements. The redistribution mode therefore provided a mechanism by which vegetation damped the impact of spring temperature variability by redistributing the timing of productivity within the growing season, making ecosystems more resilient to variability in climate. Without such redistribution, annual ecosystem responses to climate anomalies would be larger and have a stronger impact on interannual variations in plant carbon uptake and the net carbon sink.

A novel finding from our regional SVD and zonal redistribution analysis is that seasonal redistribution of plant productivity was more prominent in forests at lower latitudes. These results suggest that depletion of water resources in response to above average spring productivity is less likely at higher latitude regions with shorter growing seasons. Likewise, it may be more difficult for high latitude ecosystems to recover from low spring productivity within the limited seasonal window where radiation and mean temperature are favorable for growth, or where vegetation is more strongly regulated by photoperiod (Bauerle et al., 2012). This is consistent with Walther et al. (2019) where vegetation in northern ecosystems was shown to be less susceptible to productivity losses under negative moisture anomalies. We note that zonal analysis of SIF observations indicated a greater role for seasonal redistribution across all ecosystems when compared to results based on VI observations. A potential explanation for this disparity is that SIF may capture aspects of water stress on plant productivity that are not detected by more traditional VIs (e.g. Sun et al., 2015). That different satellite datasets yielded quantitatively different interpretations regarding the role of seasonal redistribution versus amplification further underscores the need for improving satellite-based vegetation data (including SIF) so they can be used to study IAV more reliably. This also warrants caution when using VI observations to extend SIF datasets backwards in time (e.g. Li and Xiao, 2019).

Another key result born out from our statistical analysis (and consistent across satellite vegetation data) was the identification of an amplification mode (second most dominant mode of IAV), which was characterized by growing season-integrated increases or decreases in productivity that were more strongly tied to IAV in moisture availability, rather than temperature. This result is consistent with Humphrey et al. (2018), who showed that the atmospheric CO_2 growth rate slowed globally (implying greater terrestrial uptake) when TWS was anomalously high, and with Keppel-Aleks et al. (2014) who showed that interannual variations in Northern Hemisphere net fluxes were more closely tied to drought severity than to temperature. Our approach, however, may move us closer to regional attribution and towards developing a mechanistic understanding of these patterns, since we can use spatially explicit satellite observations at regional, rather than global scale, to quantify the impact of moisture availability on gross uptake rather than net exchange. We note that growing season integrated IAV in the analyzed satellite vegetation data was much less than the seasonal amplitude, underscoring that large variations in the growth rate of atmospheric CO_2 result from relatively small changes in component fluxes (i.e., gross and net productivity and respiration).

2.4. Conclusions

We showed that quantifying IAV in satellite vegetation data at fine spatial resolution is challenging given the low magnitudes in IAV and the relatively low signal-to-noise performances of newly available (SIF) and long-standing satellite (MODIS, AVHRR) vegetation data. While our study showed that IAV of such diverse satellite vegetation data are difficult to validate against ground-based eddy covariance carbon flux observations, we also demonstrated that meaningful insights on IAV in vegetation productivity can be gained from these datasets at regional scales. At these scales, IAV patterns in SIF were generally more in agreement with satellite observations of VIs (MODIS, AVHRR). Yet, our analysis did highlight some key differences, including that SIF-based patterns indicate a generally stronger role of seasonal redistribution of plant productivity. These results underscore that improved satellite observation capabilities on longer timescales are required to fully characterize and validate IAV patterns (and by inference long-term trends) in vegetation productivity, and that the limitations of currently available long-term satellite datasets need to be carefully considered when contrasting the advantages and disadvantages of different types of vegetation observations.

Our SVD analysis at regional scales yielded two dominant modes that were remarkably consistent across the more novel SIF and long-standing VI datasets. The first most dominant mode of IAV in vegetation productivity was dominated by a seasonal redistribution of productivity towards earlier (later) in the growing season, and was associated both with warmer (colder) spring temperatures and drier (wetter) summer and fall conditions. Our results showed that seasonal redistribution was more prevalent at lower latitudes, suggesting that these regions, which are characterized by longer growing seasons, are more likely to experience a summer depletion of water resources and reduced plant productivity following an earlier and more productive spring. As the vegetation seasonality in the northern continents is already diminishing (Xu et al., 2013), this may suggest that this redistribution mode may become more dominant under climate change. A second dominant mode born out of our SVD analysis (termed amplification) was associated with a uniform increase (decrease) in plant productivity across the growing season. This mode, which likely contributes more efficiently to annual productivity, was shown to be more closely tied to moisture (especially during the peak growing season) rather than temperature. These results show that moisture availability, as opposed to temperature, may play a stronger role in IAV of growing season integrated vegetation productivity. The different roles through which temperature and moisture variability influence seasonally integrated vegetation productivity IAV must be carefully considered when assessing the consequences of climate change and variability on the long-term carbon sink.

References

Badgley, G., Field, C.B., Berry, J.A., 2017. Canopy near-infrared reflectance and terrestrial photosynthesis. Sci. Adv. 3, e1602244.

Baker, N.R., 2008. Chlorophyll fluorescence: a probe of photosynthesis in vivo. Annu. Rev. Plant Biol. 59, 89–113.

Baldocchi, D., Falge, E., Gu, L., Olson, R., Hollinger, D., Running, S., Anthoni, P., Bernhofer, C., Davis, K., Evans, R., 2001. FLUXNET: A new tool to study the temporal and spatial variability of ecosystem-scale carbon dioxide, water vapor, and energy flux densities. Bull. Am. Meteorol. Soc. 82, 2415–2434.

Barnett, T.P., Adam, J.C., Lettenmaier, D.P., 2005. Potential impacts of a warming climate on water availability in snow-dominated regions. Nature 438, 303.

Bauerle, W.L., Oren, R., Way, D.A., Qian, S.S., Stoy, P.C., Thornton, P.E., Bowden, J.D., Hoffman, F.M., Reynolds, R.F., 2012. Photoperiodic regulation of the seasonal pattern of photosynthetic capacity and the implications for carbon cycling. Proc. Natl. Acad. Sci. 109, 8612–8617. https://doi.org/10.1073/pnas.1119131109

Beck, P.S.A., Atzberger, C., Høgda, K.A., Johansen, B., Skidmore, A.K., 2006. Improved monitoring of vegetation dynamics at very high latitudes: A new method using MODIS NDVI. Remote Sens. Environ. 100, 321–334.

Buermann, W., Bikash, P.R., Jung, M., Burn, D.H., Reichstein, M., 2013. Earlier springs decrease peak summer productivity in North American boreal forests. Environ. Res. Lett. 8, 24027.

Buermann, W., Forkel, M., O'Sullivan, M., Sitch, S., Friedlingstein, P., Haverd, V., Jain, A.K., Kato, E., Kautz, M., Lienert, S., Lombardozzi, D., Nabel, J.E.M.S., Tian, H., Wiltshire, A.J., Zhu, D., Smith, W.K., Richardson, A.D., 2018. Widespread seasonal compensation effects of spring warming on northern plant productivity. Nature 562, 110–114. https://doi.org/10.1038/s41586-018-0555-7

Chen, B., Coops, N.C., Fu, D., Margolis, H.A., Amiro, B.D., Barr, A.G., Black, T.A., Arain, M.A., Bourque, C.P.-A., Flanagan, L.B., 2011. Assessing eddy-covariance flux tower location bias across the Fluxnet-Canada Research Network based on remote sensing and footprint modelling. Agric. For. Meteorol. 151, 87–100.

Cox, P.M., Pearson, D., Booth, B.B., Friedlingstein, P., Huntingford, C., Jones, C.D., Luke, C.M., 2013. Sensitivity of tropical carbon to climate change constrained by carbon dioxide variability. Nature 494, 341–344. https://doi.org/10.1038/nature11882

Didan, K., 2015. MOD13C2 MODIS/Terra vegetation indices monthly L3 global 0.05 deg CMG V006. NASA EOSDIS L. Process. DAAC, doi 10.

Domec, J.-C., King, J.S., Ward, E., Oishi, A.C., Palmroth, S., Radecki, A., Bell, D.M., Miao, G., Gavazzi, M., Johnson, D.M., 2015. Conversion of natural forests to managed forest plantations decreases tree resistance to prolonged droughts. For. Ecol. Manage. 355, 58–71.

Eitel, J.U.H., Vierling, L.A., Litvak, M.E., Long, D.S., Schulthess, U., Ager, A.A., Krofcheck, D.J., Stoscheck, L., 2011. Broadband, red-edge information from satellites improves early stress detection in a New Mexico conifer woodland. Remote Sens. Environ. 115, 3640–3646.

Frankenberg, C., Fisher, J.B., Worden, J., Badgley, G., Saatchi, S.S., Lee, J., Toon, G.C., Butz, A., Jung, M., Kuze, A., 2011. New global observations of the terrestrial carbon cycle from GOSAT: Patterns of plant fluorescence with gross primary productivity. Geophys. Res. Lett. 38.

Frankenberg, C., O'Dell, C., Berry, J., Guanter, L., Joiner, J., Köhler, P., Pollock, R., Taylor, T.E., 2014. Prospects for chlorophyll fluorescence remote sensing from the Orbiting Carbon Observatory-2. Remote Sens. Environ. 147, 1–12.

Golub, G.H., Reinsch, C., 1971. Singular value decomposition and least squares solutions, in: Linear Algebra. Springer, pp. 134–151.

Grassini, P., Yang, H., Cassman, K.G., 2009. Limits to maize productivity in Western Corn-Belt: a simulation analysis for fully irrigated and rainfed conditions. Agric. For. Meteorol. 149, 1254–1265.

Green, J.K., Seneviratne, S.I., Berg, A.M., Findell, K.L., Hagemann, S., Lawrence, D.M., Gentine, P., 2019. Large influence of soil moisture on long-term terrestrial carbon uptake. Nature 565, 476.

Guan, K., Pan, M., Li, H., Wolf, A., Wu, J., Medvigy, D., Caylor, K.K., Sheffield, J., Wood, E.F., Malhi, Y., 2015. Photosynthetic seasonality of global tropical forests constrained by hydroclimate. Nat. Geosci. 8, 284.

Guanter, L., Frankenberg, C., Dudhia, A., Lewis, P.E., Gómez-Dans, J., Kuze, A., Suto, H., Grainger, R.G., 2012. Retrieval and global assessment of terrestrial chlorophyll fluorescence from GOSAT space measurements. Remote Sens. Environ. 121, 236–251.

Guanter, L., Zhang, Y., Jung, M., Joiner, J., Voigt, M., Berry, J.A., Frankenberg, C., Huete, A.R., Zarco-Tejada, P., Lee, J.-E., 2014. Global and time-resolved monitoring of crop photosynthesis with chlorophyll fluorescence. Proc. Natl. Acad. Sci. 201320008.

Guay, K.C., Beck, P.S.A., Goetz, S.J., 2015. Long-Term Arctic Growing Season NDVI Trends from GIMMS 3g, 1982-2012. ORNL DAAC.

Hansen, M., DeFries, R., Townshend, J.R.G., Sohlberg, R., 1998. Land cover classification derived from AVHRR. Coll. Park. MD Glob. L. Cover Facil.

Harris, I., Jones, P.D., Osborn, T.J., Lister, D.H., 2014. Updated high-resolution grids of monthly climatic observations–the CRU TS3. 10 Dataset. Int. J. Climatol. 34, 623–642.

Huete, A., Didan, K., Miura, T., Rodriguez, E.P., Gao, X., Ferreira, L.G., 2002. Overview of the radiometric and biophysical performance of the MODIS vegetation indices. Remote Sens. Environ. 83, 195–213.

Humphrey, V., Zscheischler, J., Ciais, P., Gudmundsson, L., Sitch, S., Seneviratne, S.I., 2018. Sensitivity of atmospheric CO2 growth rate to observed changes in terrestrial water storage. Nature 560, 628–631. https://doi.org/10.1038/s41586-018-0424-4

Jeong, S.-J., Schimel, D., Frankenberg, C., Drewry, D.T., Fisher, J.B., Verma, M., Berry, J.A., Lee, J.-E., Joiner, J., 2017. Application of satellite solar-induced chlorophyll fluorescence to understanding large-scale variations in vegetation phenology and function over northern high latitude forests. Remote Sens. Environ. 190, 178–187.

Joiner, J., Guanter, L., Lindstrot, R., Voigt, M., Vasilkov, A.P., Middleton, E.M., Huemmrich, K.F., Yoshida, Y., Frankenberg, C., 2013. Global monitoring of terrestrial chlorophyll fluorescence from moderate-spectral-resolution near-infrared satellite measurements: methodology, simulations, and application to GOME-2. Atmos. Meas. Tech. 6, 2803–2823.

Joiner, J., Yoshida, Y., Guanter, L., Middleton, E.M., 2016. New methods for the retrieval of chlorophyll red fluorescence from hyperspectral satellite instruments: simulations and application to GOME-2 and SCIAMACHY. Atmos. Meas. Tech. 9.

Joiner, J., Yoshida, Y., Vasilkov, A.P., Middleton, E.M., 2011. First observations of global and seasonal terrestrial chlorophyll fluorescence from space. Biogeosciences 8, 637–651.

Joiner, J., Yoshida, Y., Vasilkov, A.P., Middleton, E.M., Campbell, P.K.E., Kuze, A., 2012. Filling-in of near-infrared solar lines by terrestrial fluorescence and other geophysical effects: simulations and space-based observations from SCIAMACHY and GOSAT. Atmos. Meas. Tech. 5, 809–829.

Jung, M., Reichstein, M., Schwalm, C.R., Huntingford, C., Sitch, S., Ahlström, A., Arneth, A., Camps-Valls, G., Ciais, P., Friedlingstein, P., 2017. Compensatory water effects link yearly global land CO 2 sink changes to temperature. Nature 541, 516.

Keppel-Aleks, G., Wolf, A.S., Mu, M., Doney, S.C., Morton, D.C., Kasibhatla, P.S., Miller, J.B., Dlugokencky, E.J., Randerson, J.T., 2014. Separating the influence of temperature, drought, and fire on interannual variability in atmospheric CO2. Global Biogeochem. Cycles 28, 1295–1310. https://doi.org/doi:10.1002/2014GB004890

Kimball, J.S., Thornton, P.E., White, M.A., Running, S.W., 1997. Simulating forest productivity and surface–atmosphere carbon exchange in the BOREAS study region. Tree Physiol. 17, 589–599.

Köhler, P., Frankenberg, C., Magney, T.S., Guanter, L., Joiner, J., Landgraf, J., 2018. Global Retrievals of Solar-Induced Chlorophyll Fluorescence With TROPOMI: First Results and Intersensor Comparison to OCO-2. Geophys. Res. Lett. 45, 10–456.

Koren, G., van Schaik, E., Araújo, A.C., Boersma, K.F., Gärtner, A., Killaars, L., Kooreman, M.L., Kruijt, B., van der Laan-Luijkx, I.T., von Randow, C., 2018. Widespread reduction in sun-induced fluorescence from the Amazon during the 2015/2016 El Niño. Philos. Trans. R. Soc. B Biol. Sci. 373, 20170408.

Landerer, F.W., Swenson, S.C., 2012. Accuracy of scaled GRACE terrestrial water storage estimates. Water Resour. Res. 48.

Lasslop, G., Reichstein, M., Papale, D., Richardson, A.D., Arneth, A., Barr, A., Stoy, P., Wohlfahrt, G., 2010. Separation of net ecosystem exchange into assimilation and respiration using a light response curve approach: critical issues and global evaluation. Glob. Chang. Biol. 16, 187–208.

Lauvaux, T., Schuh, A.E., Uliasz, M., Richardson, S., Miles, N., Andrews, A.E., Sweeney, C., Diaz, L.I., Martins, D., Shepson, P.B., 2012. Constraining the CO 2 budget of the corn belt:

exploring uncertainties from the assumptions in a mesoscale inverse system. Atmos. Chem. Phys. 12.

Le Quéré, C., Andrew, R.M., Friedlingstein, P., Sitch, S., Pongratz, J., Manning, A.C., Korsbakken, J.I., Peters, G.P., Canadell, J.G., Jackson, R.B., Boden, T.A., Tans, P.P., Andrews, O.D., Arora, V.K., Bakker, D.C.E., Barbero, L., Becker, M., Betts, R.A., Bopp, L., Chevallier, F., Chini, L.P., Ciais, P., Cosca, C.E., Cross, J., Currie, K., Gasser, T., Harris, I., Hauck, J., Haverd, V., Houghton, R.A., Hunt, C.W., Hurtt, G., Ilyina, T., Jain, A.K., Kato, E., Kautz, M., Keeling, R.F., Klein Goldewijk, K., Körtzinger, A., Landschützer, P., Lefèvre, N., Lenton, A., Lienert, S., Lima, I., Lombardozzi, D., Metzl, N., Millero, F., Monteiro, P.M.S., Munro, D.R., Nabel, J.E.M.S., Nakaoka, S.-I., Nojiri, Y., Padin, X.A., Peregon, A., Pfeil, B., Pierrot, D., Poulter, B., Rehder, G., Reimer, J., Rödenbeck, C., Schwinger, J., Séférian, R., Skjelvan, I., Stocker, B.D., Tian, H., Tilbrook, B., Tubiello, F.N., Van Der Laan-Luijkx, I.T., Van Der Werf, G.R., Van Heuven, S., Viovy, N., Vuichard, N., Walker, A.P., Watson, A.J., Wiltshire, A.J., Zaehle, S., Zhu, D., 2018. Global Carbon Budget 2017. Earth Syst. Sci. Data 10, 405–448. https://doi.org/10.5194/essd-10-405-2018

Li, X., Xiao, J., 2019. A Global, 0.05-Degree Product of Solar-Induced Chlorophyll Fluorescence Derived from OCO-2, MODIS, and Reanalysis Data. Remote Sens. 11, 517.

Li, X., Xiao, J., He, B., Altaf Arain, M., Beringer, J., Desai, A.R., Emmel, C., Hollinger, D.Y., Krasnova, A., Mammarella, I., 2018. Solar-induced chlorophyll fluorescence is strongly correlated with terrestrial photosynthesis for a wide variety of biomes: First global analysis based on OCO-2 and flux tower observations. Glob. Chang. Biol. 24, 3990–4008.

Long, D., Longuevergne, L., Scanlon, B.R., 2014. Uncertainty in evapotranspiration from land surface modeling, remote sensing, and GRACE satellites. Water Resour. Res. 50, 1131–1151.

Long, D., Scanlon, B.R., Longuevergne, L., Sun, A.Y., Fernando, D.N., Save, H., 2013. GRACE satellite monitoring of large depletion in water storage in response to the 2011 drought in Texas. Geophys. Res. Lett. 40, 3395–3401.

Loyola, D.G., Koukouli, M.E., Valks, P., Balis, D.S., Hao, N., Van Roozendael, M., Spurr, R.J.D., Zimmer, W., Kiemle, S., Lerot, C., 2011. The GOME-2 total column ozone product: Retrieval algorithm and ground-based validation. J. Geophys. Res. Atmos. 116.

Lv, S., Zeng, Y., Wen, J., Zhao, H., Su, Z., 2018. Estimation of penetration depth from soil effective temperature in microwave radiometry. Remote Sens. 10, 519.

Munro, R., Eisinger, M., Anderson, C., Callies, J., Corpaccioli, E., Lang, R., Lefebvre, A., Livschitz, Y., Albinana, A.P., 2006. GOME-2 on MetOp, in: Proc. of The 2006 EUMETSAT Meteorological Satellite Conference, Helsinki, Finland. p. 48.

Nemani, R.R., Keeling, C.D., Hashimoto, H., Jolly, W.M., Piper, S.C., Tucker, C.J., Myneni, R.B., Running, S.W., 2003. Climate-driven increases in global terrestrial net primary production from 1982 to 1999. Science (80-.). 300, 1560–1563.

Nepstad, D.C., de Carvalho, C.R., Davidson, E.A., Jipp, P.H., Lefebvre, P.A., Negreiros, G.H., da Silva, E.D., Stone, T.A., Trumbore, S.E., Vieira, S., 1994. The role of deep roots in the hydrological and carbon cycles of Amazonian forests and pastures. Nature 372, 666.

Noormets, A., Desai, A.R., Cook, B.D., Euskirchen, E.S., Ricciuto, D.M., Davis, K.J., Bolstad, P. V, Schmid, H.P., Vogel, C. V, Carey, E. V, 2008. Moisture sensitivity of ecosystem respiration: comparison of 14 forest ecosystems in the Upper Great Lakes Region, USA. Agric. For. Meteorol. 148, 216–230.

Parida, B.R., Buermann, W., 2014. Increasing summer drying in North American ecosystems in response to longer nonfrozen periods. Geophys. Res. Lett. 41, 5476–5483.

Pastorello, G., Papale, D., Chu, H., Trotta, C., Agarwal, D., Canfora, E., Baldocchi, D., Torn, M., 2017. The FLUXNET2015 dataset: The longest record of global carbon, water, and energy fluxes is updated. Eos (Washington. DC). 98.

Payne, J.T., Wood, A.W., Hamlet, A.F., Palmer, R.N., Lettenmaier, D.P., 2004. Mitigating the effects of climate change on the water resources of the Columbia River basin. Clim. Change 62, 233–256.

Penuelas, J., Filella, I., 2003. Deuterium labelling of roots provides evidence of deep water access and hydraulic lift by Pinus nigra in a Mediterranean forest of NE Spain. Environ. Exp. Bot. 49, 201–208.

Piao, S., Friedlingstein, P., Ciais, P., Viovy, N., Demarty, J., 2007. Growing season extension and its impact on terrestrial carbon cycle in the Northern Hemisphere over the past 2 decades. Global Biogeochem. Cycles 21.

Pinzon, J., Tucker, C., 2014. A non-stationary 1981–2012 AVHRR NDVI3g time series. Remote Sens. 6, 6929–6960.

Porter, J.R., Semenov, M.A., 2005. Crop responses to climatic variation. Philos. Trans. R. Soc. B Biol. Sci. 360, 2021–2035.

Reichstein, M., Falge, E., Baldocchi, D., Papale, D., Aubinet, M., Berbigier, P., Bernhofer, C., Buchmann, N., Gilmanov, T., Granier, A., 2005. On the separation of net ecosystem exchange into assimilation and ecosystem respiration: review and improved algorithm. Glob. Chang. Biol. 11, 1424–1439.

Richardson, A.D., Andy Black, T., Ciais, P., Delbart, N., Friedl, M.A., Gobron, N., Hollinger, D.Y., Kutsch, W.L., Longdoz, B., Luyssaert, S., 2010. Influence of spring and autumn phenological transitions on forest ecosystem productivity. Philos. Trans. R. Soc. B Biol. Sci. 365, 3227–3246.

Rossini, M., Nedbal, L., Guanter, L., Ač, A., Alonso, L., Burkart, A., Cogliati, S., Colombo, R., Damm, A., Drusch, M., 2015. Red and far red Sun-induced chlorophyll fluorescence as a measure of plant photosynthesis. Geophys. Res. Lett. 42, 1632–1639.

Running, S.W., Nemani, R.R., Heinsch, F.A., Zhao, M., Reeves, M., Hashimoto, H., 2004. A continuous satellite-derived measure of global terrestrial primary production. AIBS Bull. 54, 547–560.

Running, S.W., Zhao, M., 2015. Daily GPP and annual NPP (MOD17A2/A3) products NASA Earth Observing System MODIS land algorithm. MOD17 User's Guid.

Schaefer, K., Collatz, G.J., Tans, P., Denning, A.S., Baker, I., Berry, J., Prihodko, L., Suits, N., Philpott, A., 2008. Combined simple biosphere/Carnegie-Ames-Stanford approach terrestrial carbon cycle model. J. Geophys. Res. Biogeosciences 113.

Sellers, P.J., 1987. Canopy reflectance, photosynthesis, and transpiration, II. The role of biophysics in the linearity of their interdependence. Remote Sens. Environ. 21, 143–183.

Sellers, P.J., 1985. Canopy reflectance, photosynthesis and transpiration. Int. J. Remote Sens. 6, 1335–1372.

Sellers, P.J., Berry, J.A., Collatz, G.J., Field, C.B., Hall, F.G., 1992. Canopy reflectance, photosynthesis, and transpiration. III. A reanalysis using improved leaf models and a new canopy integration scheme. Remote Sens. Environ. 42, 187–216.

Song, L., Guanter, L., Guan, K., You, L., Huete, A., Ju, W., Zhang, Y., 2018. Satellite sun-induced chlorophyll fluorescence detects early response of winter wheat to heat stress in the Indian Indo-Gangetic Plains. Glob. Chang. Biol. 24, 4023–4037.

Sun, Y., Frankenberg, C., Wood, J.D., Schimel, D.S., Jung, M., Guanter, L., Drewry, D.T., Verma, M., Porcar-Castell, A., Griffis, T.J., 2017. OCO-2 advances photosynthesis observation from space via solar-induced chlorophyll fluorescence. Science (80-.). 358, eaam5747.

Sun, Y., Fu, R., Dickinson, R., Joiner, J., Frankenberg, C., Gu, L., Xia, Y., Fernando, N., 2015. Drought onset mechanisms revealed by satellite solar-induced chlorophyll fluorescence: Insights from two contrasting extreme events. J. Geophys. Res. Biogeosciences 120, 2427–2440.

Swann, A.L.S., Koven, C.D., 2017. A direct estimate of the seasonal cycle of evapotranspiration over the Amazon basin. J. Hydrometeorol. 18, 2173–2185.

Swenson, S., Wahr, J., 2006. Post-processing removal of correlated errors in GRACE data. Geophys. Res. Lett. 33.

Swenson, S.C., 2012. GRACE monthly land water mass grids NETCDF RELEASE 5.0. Phys. Oceanogr. Distrib. Act. Arch. Cent. (PO. DAAC), California, doi 10.

Van der Tol, C., Berry, J.A., Campbell, P.K.E., Rascher, U., 2014. Models of fluorescence and photosynthesis for interpreting measurements of solar-induced chlorophyll fluorescence. J. Geophys. Res. Biogeosciences 119, 2312–2327.

Walther, S., Duveiller, G., Jung, M., Guanter, L., Cescatti, A., Camps-Valls, G., 2019. Satellite Observations of the Contrasting Response of Trees and Grasses to Variations in Water Availability. Geophys. Res. Lett. 46, 1429–1440.

Walther, S., Voigt, M., Thum, T., Gonsamo, A., Zhang, Y., Köhler, P., Jung, M., Varlagin, A., Guanter, L., 2016. Satellite chlorophyll fluorescence measurements reveal large-scale decoupling of photosynthesis and greenness dynamics in boreal evergreen forests. Glob. Chang. Biol. 22, 2979–2996.

Wang, X., Piao, S., Ciais, P., Li, J., Friedlingstein, P., Koven, C., Chen, A., 2011. Spring temperature change and its implication in the change of vegetation growth in North America from 1982 to 2006. Proc. Natl. Acad. Sci. 108, 1240–1245.

Weiss, M., Baret, F., Garrigues, S., Lacaze, R., 2007. LAI and fAPAR CYCLOPES global products derived from VEGETATION. Part 2: validation and comparison with MODIS collection 4 products. Remote Sens. Environ. 110, 317–331.

Wigneron, J.-P., Jackson, T.J., O'neill, P., De Lannoy, G., De Rosnay, P., Walker, J.P., Ferrazzoli, P., Mironov, V., Bircher, S., Grant, J.P., 2017. Modelling the passive microwave signature from land surfaces: A review of recent results and application to the L-band SMOS & SMAP soil moisture retrieval algorithms. Remote Sens. Environ. 192, 238–262.

Wohlfahrt, G., Galvagno, M., 2017. Revisiting the choice of the driving temperature for eddy covariance CO2 flux partitioning. Agric. For. Meteorol. 237, 135–142.

Wohlfahrt, G., Gerdel, K., Migliavacca, M., Rotenberg, E., Tatarinov, F., Müller, J., Hammerle, A., Julitta, T., Spielmann, F.M., Yakir, D., 2018. Sun-induced fluorescence and gross primary productivity during a heat wave. Sci. Rep. 8, 14169.

Wu, X., Xiao, X., Zhang, Y., He, W., Wolf, S., Chen, J., He, M., Gough, C.M., Qin, Y., Zhou, Y., 2018. Spatiotemporal Consistency of Four Gross Primary Production Products and Solar-Induced Chlorophyll Fluorescence in Response to Climate Extremes Across CONUS in 2012. J. Geophys. Res. Biogeosciences 123, 3140–3161.

Xu, L., Myneni, R.B., Chapin Iii, F.S., Callaghan, T. V, Pinzon, J.E., Tucker, C.J., Zhu, Z., Bi, J., Ciais, P., Tømmervik, H., 2013. Temperature and vegetation seasonality diminishment over northern lands. Nat. Clim. Chang. 3, 581.

Yang, X., Tang, J., Mustard, J.F., Lee, J., Rossini, M., Joiner, J., Munger, J.W., Kornfeld, A., Richardson, A.D., 2015. Solar-induced chlorophyll fluorescence that correlates with canopy photosynthesis on diurnal and seasonal scales in a temperate deciduous forest. Geophys. Res. Lett. 42, 2977–2987.

Yoshida, Y., Joiner, J., Tucker, C., Berry, J., Lee, J.-E., Walker, G., Reichle, R., Koster, R., Lyapustin, A., Wang, Y., 2015. The 2010 Russian drought impact on satellite measurements of solar-induced chlorophyll fluorescence: Insights from modeling and comparisons with parameters derived from satellite reflectances. Remote Sens. Environ. 166, 163–177.

Zhang, Yongguang, Guanter, L., Joiner, J., Song, L., Guan, K., 2018. Spatially-explicit monitoring of crop photosynthetic capacity through the use of space-based chlorophyll fluorescence data. Remote Sens. Environ. 210, 362–374.

Zhang, Yao, Xiao, X., Jin, C., Dong, J., Zhou, S., Wagle, P., Joiner, J., Guanter, L., Zhang, Yongguang, Zhang, G., 2016. Consistency between sun-induced chlorophyll fluorescence and gross primary production of vegetation in North America. Remote Sens. Environ. 183, 154–169.

Zhang, Yao, Xiao, X., Zhang, Yongguang, Wolf, S., Zhou, S., Joiner, J., Guanter, L., Verma, M., Sun, Y., Yang, X., Paul-Limoges, E., Gough, C.M., Wohlfahrt, G., Gioli, B., van der Tol, C., Yann, N., Lund, M., de Grandcourt, A., 2018. On the relationship between sub-daily instantaneous and daily total gross primary production: Implications for interpreting satellite-based SIF retrievals. Remote Sens. Environ. 205, 276–289. https://doi.org/10.1016/j.rse.2017.12.009

Zhang, Z., Chao, B.F., Chen, J., Wilson, C.R., 2015. Terrestrial water storage anomalies of Yangtze River Basin droughts observed by GRACE and connections with ENSO. Glob. Planet. Change 126, 35–45.

Zhao, M., Running, S.W., 2010. Drought-Induced Reduction in Global Terrestrial Net Primary Production from 2000 Through 2009. Science (80-.). 329, 940–943. https://doi.org/10.1126/science.1192666

Zhou, L., Tucker, C.J., Kaufmann, R.K., Slayback, D., Shabanov, N. V, Myneni, R.B., 2001. Variations in northern vegetation activity inferred from satellite data of vegetation index during 1981 to 1999. J. Geophys. Res. Atmos. 106, 20069–20083. https://doi.org/10.1029/2000JD000115

Chapter 3

Tower-Based Observations of Red and Far-Red SIF over Temperate Deciduous Forest Reveal Challenges in Assessing Stress-Induced Losses in Summer GPP

Abstract

As global observations of Solar-Induced chlorophyll Fluorescence (SIF) become available from multiple satellite platforms, SIF is increasingly used as a proxy for photosynthetic activity and ecosystem productivity. Because the relationship between SIF and gross primary productivity (GPP) depends on a variety of factors including ecosystem type and environmental conditions, it is necessary to assess SIF observations across a variety of temporal and spatial scales and ecosystems. To explore how SIF signals relate to productivity over a temperate deciduous forest, we deployed a PhotoSpec spectrometer system to the University of Michigan Biological Station AmeriFlux site (US-UMB) in the northern Lower Peninsula of Michigan during the 2018 and 2019 growing seasons. The PhotoSpec system comprises two narrowband spectrometers, allowing for the retrieval of SIF in both the red and far-red regions of the electromagnetic spectrum, and a broadband spectrometer for the assessment of various vegetation indices. We found that SIF is more strongly related to radiation than to GPP, and that the quantitative relationship of SIF to GPP decreases over the course of the growing season. Additionally, we show that while SIF irradiances do not respond to synoptic-scale changes in summer productivity

resulting from environmental stress, the red:far-red SIF ratio does exhibit an increase in response to a moderate drought in August 2018. Our results suggest that the combination of SIF observations at multiple wavelengths could improve the ability of SIF to detect stress-induced losses in productivity.

3.1. Introduction

Global ecosystems currently act as a sink for roughly one quarter of anthropogenic carbon emissions (Le Quéré et al., 2018), and the climate-driven variations in this carbon sink therefore have significant implications for long-term changes in climate. Direct quantification of net and gross ecosystem productivity is elusive, however, given the spatial heterogeneity of the global land surface and the lack of direct observations of land-atmosphere carbon exchange, and contributes significant uncertainty to the global carbon budget (Le Quéré et al., 2018).

The unique challenges involved in quantifying the biosphere carbon sink point to the need for satellite-based observations that allow for the inference of ecosystem productivity across a variety of ecosystems and spatial scales. Optical indices such as the normalized difference vegetation index (NDVI) have been traditionally used to quantify ecosystem productivity (Running et al., 2004), but these signals represent the ‘greenness’ of vegetation and lack a direct tie to photosynthetic machinery, thus requiring the inclusion of meteorological data for inferring environmental stressors and estimating light use efficiency (LUE), or the efficiency at which sunlight is used to drive photochemistry and carbon fixation. Additionally, vegetation indices can be vulnerable to saturation effects (X. Yang et al., 2015) or influenced by factors unrelated to vegetation such as snow cover (Beck et al., 2006).

Solar-induced Chlorophyll Fluorescence (SIF) is a novel measurement from space-based platforms that is directly tied to the photosynthetic machinery, since it represents an emission of excess photons from photosystems in the red and far-red region of the electromagnetic spectrum. Satellite observations of far-red SIF have been shown to scale with spatial and seasonal patterns of gross primary productivity (GPP; Frankenberg et al., 2011; Sun et al., 2017), indicating a potential for SIF as a more direct proxy of carbon uptake through photosynthesis. There has been a recent proliferation of satellite-based observations of far-red SIF (e.g. Frankenberg et al., 2014; Joiner et al., 2013; Köhler, Frankenberg, et al., 2018) and, more recently, red SIF (e.g. Köhler et al., 2020) and quantitative assessments of SIF signals above a range of ecosystems and spatial and temporal scales are needed to inform the interpretation of these data.

The strong relationship between SIF and GPP in part stems from a shared dependence on solar radiation. As leaves absorb solar photons of sunlight for use in photosynthesis, excess energy is either radiated away as heat via non-photochemical quenching (NPQ) or is fluoresced back to the environment as SIF. Top-of-canopy SIF can be expressed as:

$$\text{SIF} = \text{SIF}_{\text{yield}} \text{ x PAR x fPAR x } \text{f}_{\text{esc}} \qquad (3.1)$$

(Zeng et al., 2019) where fluorescence yield ($\text{SIF}_{\text{yield}}$) represents the efficiency at which the photosystems emit photons, photosynthetically active radiation (PAR) indicates downwelling radiation available for photosynthesis, and fPAR indicates the fraction of PAR absorbed by the canopy, which depends primarily on green leaf area, chlorophyll content, and canopy structure. The fluorescence escape ratio (f_{esc}) represents the fraction of total emitted fluorescence that escapes the top of canopy, rather than being deflected or reabsorbed by leaves deeper within the canopy ((Dechant et al., 2020; Zeng et al., 2019). Similarly, GPP can be expressed as the product of PAR, fPAR, and LUE (e.g. X. Yang et al., 2015):

$$\text{GPP} = \text{LUE} \times \text{PAR} \times \text{fPAR} \tag{3.2}$$

As LUE is the most difficult component of GPP to estimate using remote sensing and is traditionally inferred from models (Porcar-Castell et al., 2014), there is much interest in characterizing its relationship with SIF (and $\text{SIF}_{\text{yield}}$). Yang et al. (2015) used tower-based observations over a temperate deciduous forest to show a correlation of far-red SIF with GPP on diurnal and seasonal timescales and, by dividing SIF and GPP by total absorbed PAR, likewise showed a weak correlation between LUE and $\text{SIF}_{\text{yield}}$, indicating that SIF observations do contain some level of information on LUE.

Observations of SIF over evergreen forest have shown further promise for assessing GPP on seasonal timescales. Magney et al. (2019) showed a strong relationship between SIF and GPP over a northern hemisphere evergreen forest under minimal changes in canopy structure and absorbed PAR, when more traditional observations such as NDVI which depend on changes in chlorophyll content cannot capture productivity dynamics. The demonstrated seasonality in SIF even when greenness remains constant suggests that the SIF signal is sensitive to seasonal changes in photoprotective pigments and LUE, and provides a robust proxy of GPP.

While strong relationships between SIF and GPP have been reported at seasonal and diurnal timescales, uncertainties remain in the exact nature of how SIF relates to GPP (Ryu et al., 2019), and in how that relationship changes across different ecosystems. Several studies have found that SIF over cropland is more closely tied to APAR than to GPP (Miao et al., 2018; K. Yang et al., 2018), and Zeng et al. (2019) demonstrated that SIF is strongly influenced by canopy structure and changes in f_{esc}. SIF is also dependent on the fluorescence yield of the photosystems. Furthermore, GPP is sensitive to ecosystem stress through changes in LUE, but it is not understood how fluorescence yield, and therefore SIF irradiances, respond to stress-induced changes and how closely the SIF response is tied to changes in GPP. Several satellite-based studies have used SIF to observe the impacts of moderate to severe drought (Song et al., 2018; Yoshida et al., 2015), but summer observations tend to be less sensitive to interannual variability as would be driven by mild stress (Butterfield et al., 2020). At the local scale, Wohlfahrt et al. (2018) showed that the SIF-GPP relationship in a Mediterranean pine forest decouples under environmental stress and suggests that much of the strong correlation between SIF and GPP in this ecosystem is driven by a shared dependence on APAR. This study brings into question the detectability of stress-induced changes in GPP from SIF irradiance, but also notes an increase in the red:far-red SIF ratio aligning with peak stress conditions. The contrasting behaviors of red and far-red SIF signals during an ecosystem stress event warrant further investigations into what can be learned from simultaneous observations of SIF at both wavelengths.

To assess the relationship between SIF and GPP and their responses to environmental variables, specifically above a temperate deciduous forest, we deployed a tower-based PhotoSpec spectrometer system (Grossmann et al., 2018) to the AmeriFlux tower at the University of Michigan Biological Station (US-UMB). We present results from the first two years of observations during the 2018 and 2019 growing seasons, during which we collected SIF observations in both the red and far-red at a high temporal frequency (~20 s), providing an opportunity to quantify diurnal and intraseasonal influences on the SIF signal. In the following analysis, our goals were to 1) explore the dependence of SIF on APAR and test how this influenced the ability of SIF to track intraseasonal changes in GPP, 2) characterize the relationship between SIF and GPP and test how it changes over the course of the growing season and during periods of stress, and 3) explore the behavior of the red:far-red SIF ratio and test if it responds to periods of environmental stress. In Section 3.2 we introduce the datasets used in this study, followed by a presentation of our results in Section 3.3, showing how our SIF observations relate to and are influenced by GPP and other environmental data. In Section 3.4 we present a discussion of caveats in using SIF to assess GPP over temperate forest and potential applications of the red:far-red SIF ratio. Lastly, a brief summary of our conclusions is included in Section 3.5.

3.2. Data and Methods

3.2.1. AmeriFlux Data at University of Michigan Biological Station

We conducted our study at the University of Michigan Biological Station (US-UMB) AmeriFlux site within a deciduous broadleaf forest comprised primarily of aspen, oak, maple, and beech, with some understory pine. The canopy height is approximately 20 m. This site was chosen in part because it is a well-studied forest ecosystem, with long-standing observations of eddy covariance water and carbon fluxes (Aron et al., 2019; C. M. Gough et al., 2013), canopy structure (Fotis et al., 2018), soil moisture (He et al., 2014), and sap flow (Matheny et al., 2017). For this study, we relied primarily on ecosystem flux observations from the AmeriFlux tower, a 46 m tower from which CO_2 and H_2O flux data have been obtained since 1999. For our analysis, we used the AmeriFlux-processed half-hourly eddy-flux GPP data from 2007 through 2019 (C. Gough et al., 2016) which uses nighttime observations and a neural network to partition daytime fluxes into respiration and GPP (see Barr et al., 2013; Wolf et al., 2016).

In addition to GPP data, we used meteorological observations from the AmeriFlux dataset included air temperature, precipitation, vapor pressure deficit (VPD), volumetric soil water content (SWC) at a depth of 30 cm, and downwelling PAR. From the half-hourly AmeriFlux data we calculated 90-minute and daily values for each variable either by simple summation (precipitation) or averaging (other variables). Leaf area index (LAI) at the site was also measured using leaf litter traps (Table 3.1).

Table 3.1. Leaf area index (LAI) values as observed at the US-UMB AmeriFlux site for 2018 and 2019 using leaf litter traps.

Species	**2018 LAI**	**2019 LAI**
Bigtooth aspen (Populus grandidentata)	1.286	0.981
Red maple (Acer rubrum)	0.891	0.730
American beech (Fagus grandifolia)	0.292	0.281
Red oak (Quercus rubra)	1.073	0.878
Paper birch (Betula papyrifera)	0.238	0.178
White pine (Pinus strobus)	0.587	0.578
Red pine (Pinus resinosa)	0.008	0.011
Total	**4.375**	**3.636**

3.2.2 PhotoSpec Tower-Based Observations

We built and deployed a PhotoSpec spectrometer system (Grossmann et al., 2018) to the US-UMB tower during the 2018 and 2019 growing seasons. The PhotoSpec system consists of two narrowband spectrometers (QEPro, Ocean Optics Inc.): one with a wavelength range of 670-732 nm and a resolution of 0.074 nm/pixel, 0.3 nm full width half maximum (FWHM), for measuring SIF in the red region of the spectrum, and a second QEPro (729-784 nm, 0.067 nm/pixel, 0.3 nm FWHM) optimized for measuring SIF in the far-red. An additional broadband spectrometer (Flame, Ocean Optics Inc.; 177-874 nm, 0.382 nm/pixel, 1.2 nm FWHM) permitted the calculation of vegetation indices such as NDVI from the measured spectra. A 2-D scanning telescope was mounted on the Ameriflux tower at a height of 45 m and could point at various locations in the canopy using a narrow field of view (about 0.7°). Light from the canopy was thus directed light into a fiber optic cable, and subsequently split as input to the three spectrometers.

We acquired observations in three azimuthal directions: 60° east of south, due south, and 60° west of south. For each azimuth angle, we acquired data along an elevation transect by scanning from 90° (nadir) to 45° below the horizon. For each individual location along the transects, we optimized the exposure times for the spectrometers to maintain consistent detector signal level. Multiple exposures were then integrated together into ~ 20 s measurements before moving the telescope to the next location. Reference spectra were collected at least every 10 measurements using an upward-facing diffuser disk. A full cycle through the three azimuth angles took approximately 90 minutes, and we therefore used 90-minute averages for sub-daily comparisons.

SIF irradiances were calculated from the QEPro spectra for the both the red (680-686 nm) and far-red (745-758 nm) regions of the electromagnetic spectrum using a physical retrieval based on the infilling of solar Fraunhofer lines (Grossmann et al., 2018). Relative SIF values were calculated by dividing the observed SIF irradiance by the total reflected irradiance to represent SIF as a percentage of reflected light. The spectra from the broadband Flame spectrometer were used to calculate NDVI and the photochemical reflectance index (PRI), which is sensitive to carotenoid pigments and light use efficiency (Gamon et al., 2001). The SIF observations were radiometrically calibrated using a second broadband Flame spectrometer with a cosine corrector (CC-3-UV-S, Ocean Optics Inc.) that was itself calibrated using radiometric standard lamp (HL-3-P-CAL, Ocean Optics Inc.). We recorded simultaneous measurements alongside the PhotoSpec instrument using a reflective calibration disk (Spectralon Diffuse

Reflectance Standard, Labsphere Inc.). Wavelength calibrations were done using a Mercury-Argon lamp (HG-1, Ocean Optics Inc.)

3.2.3. Satellite Observations of SIF from OCO-2

To compare with satellite-based observations of SIF, we obtained data from the Orbiting Carbon Observatory-2 (OCO-2) instrument (OCO-2 Science Team, 2017). OCO-2 has a local overpass time of 1:30pm and SIF is retrieved from OCO-2 spectra at 757 nm and 771 nm using a non-linear least-squares approach to evaluate the infilling of solar Fraunhofer lines (Sun et al., 2018). We included OCO-2 SIF retrievals at 757 nm (which was within our far-red fitting window of 745-758 nm) from individual OCO-2 soundings that fell within a one-degree gridcell centered at US-UMB. Individual soundings were converted to daily-averages using a clear-sky PAR proxy, which uses the cosine of the solar zenith angle to account for diurnal variability in the SIF signal. We subsequently calculated a single mean and standard deviation for each day with available overpass data, resulting in nine individual data points across the 2018 and 2019 growing seasons.

3.3. Results

3.3.1 Climatological Context of 2018-2019 Growing Seasons

The 2018 and 2019 growing seasons were more productive than the 2007-2019 multi-year mean based on eddy covariance GPP data (Fig. 3.1). For both years, GPP reached a similar seasonal peak value in July of about 11 μmol/m^2/s, about 30% higher than the multi-year mean. In both years, the high summer GPP followed delayed leaf out. In 2018, growing season onset was delayed by about a week relative to the multi-year mean, but GPP increased rapidly (~0.9 μmol/m^2/s/day) in in late May during a period with above average temperatures (Fig. 3.1a-b). In 2019 a wet and cold spring (Fig. 3.1b-c) led to a slower photosynthetic ramp up that was delayed by 2 weeks relative to the climatological mean (Fig. 3.1a).

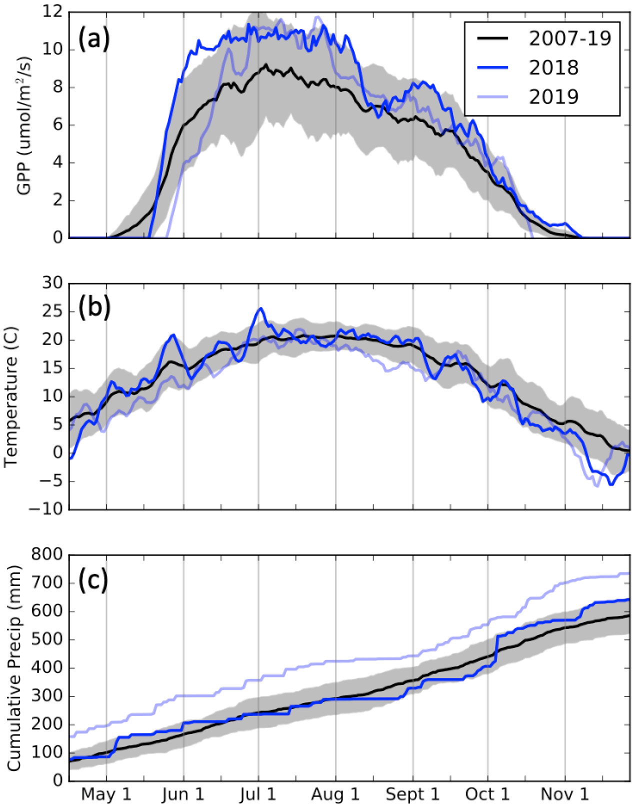

Fig. 3.1. Eddy covariance GPP (a), temperature (b), and cumulative precipitation (c) at US-UMB during the 2018 (dark blue) and 2019 (light blue) growing seasons. The 2007-2019 multi year means are included as black lines, with shading representing ±1 standard deviation. GPP and temperature are plotted as 7-day running means.

Both years experienced stress-induced declines in GPP during late summer that occurred with moderate to severe drought conditions. In 2018, there was a drought in mid August that followed dry spells in early June, early July, and in August (Fig. 3.1c). While the first of these dry periods did not lead to dry soil moisture conditions, the cumulative influence of the two later dry periods led to soil water content falling below 5% and coincided with local maxima in VPD of about 9 hPa (Fig. 3.2g). GPP levels were relatively robust during the first period of dry soil conditions from late June through July 11, but during the second dry period from late July through August 18, productivity ultimately declined by about 30%, to levels around the multi-year mean. Interestingly, GPP recovered towards the end of August, back to about 25% above the climatological mean. That GPP is increasingly sensitive to dry soil conditions over time is consistent with the fact that the soil matric potential, or the hydraulic tension of soil moisture, can continue to increase even as SWC approaches a lower limit (e.g. Köcher et al., 2009; Lascano et al., 2007). However, late summer declines in GPP occur roughly every other year at the US-UMB site, and are not always tied to an obvious drought signal. While 2019 was not characterized by obvious drought stress, GPP observations did decline in late July from about 30% to only 5% above the climatological mean, before recovering to around 15% above the climatological mean at the end of August. This less productive period coincides with low SWC (Fig. 3.2h) and little accumulated precipitation (Fig. 3.1c).

3.3.2 Characteristics of Red and Far-Red SIF Signals

Far-red SIF observations during 2018 and 2019 followed a seasonal cycle similar to that of GPP (Figure 3.2a-b), in that signals reach peak levels in early summer and steadily decline throughout late summer and fall. In contrast, the red SIF signal was relatively higher in early spring and fall (Fig. 3.2a-b). This contrast between red and far-red SIF seasonality results from top-of-canopy red SIF observations being more sensitive to canopy structure and chlorophyll content (Magney, Frankenberg, et al., 2019), such that a smaller fraction of total emitted SIF is scattered or

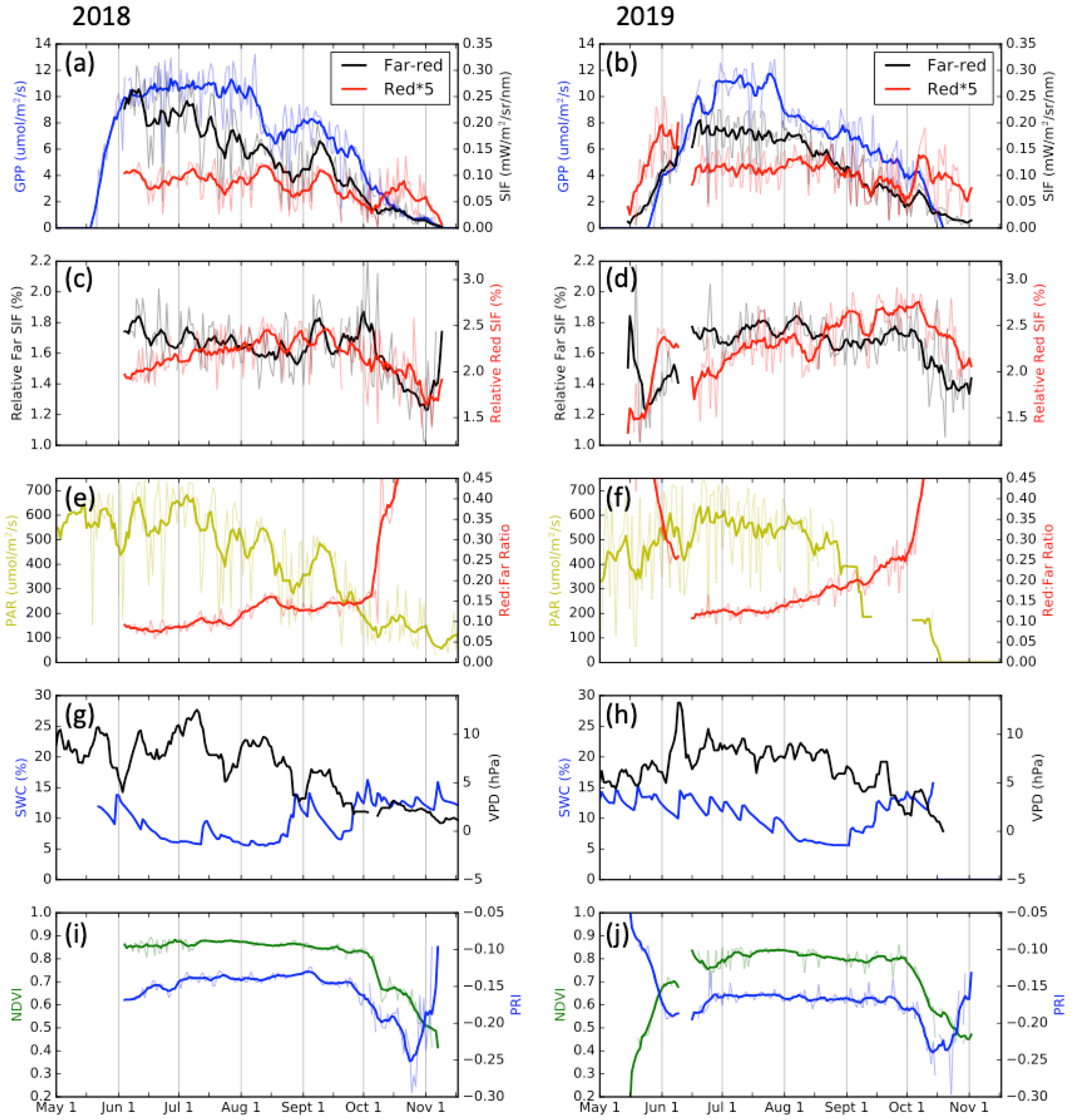

Fig. 3.2. Growing season timeseries of GPP and SIF irradiance (a-b), relative SIF (c-d), photosynthetically active radiation (PAR) and the red:far-red SIF ratio (e-f), soil water content (SWC) and vapor pressure deficit (VPD (g-h), and NDVI and PRI (i-j) during 2018 (left) and 2019 (right). With the exception of SWC and VPD, bold lines represent the 7-day running mean of daily-averaged data (thin lines).

reabsorbed by the canopy during the springtime when the canopy is not yet fully developed or as chlorophyll content decreases in fall. Thus, the red:far-red SIF ratio was much higher in spring and fall (Fig. 3.2e-f), corresponding with lower values in NDVI. In addition to intraseasonal changes in the red SIF signal and the red:far-red ratio, there was evidence of year-to-year variability, with 2018 characterized by both lower red SIF and a lower red:far-red ratio. The interannual relationships of the SIF signals were consistent with changes in other observations including NDVI, which was lower in 2019 compared to 2018 (maximum value of 0.84 compared to 0.88), and LAI, where measurements using leaf litter traps showed a substantial year-to-year contrast (4.38 in 2018 versus 3.64 in 2019; Table 3.1). These results corroborate the hypothesis that a denser canopy reduces red fluorescence. Taken together, these results suggested that far-red SIF better reflected the seasonal cycle of productivity in temperate deciduous forest, and that red SIF was more sensitive to seasonal, and potentially interannual, changes in canopy structure.

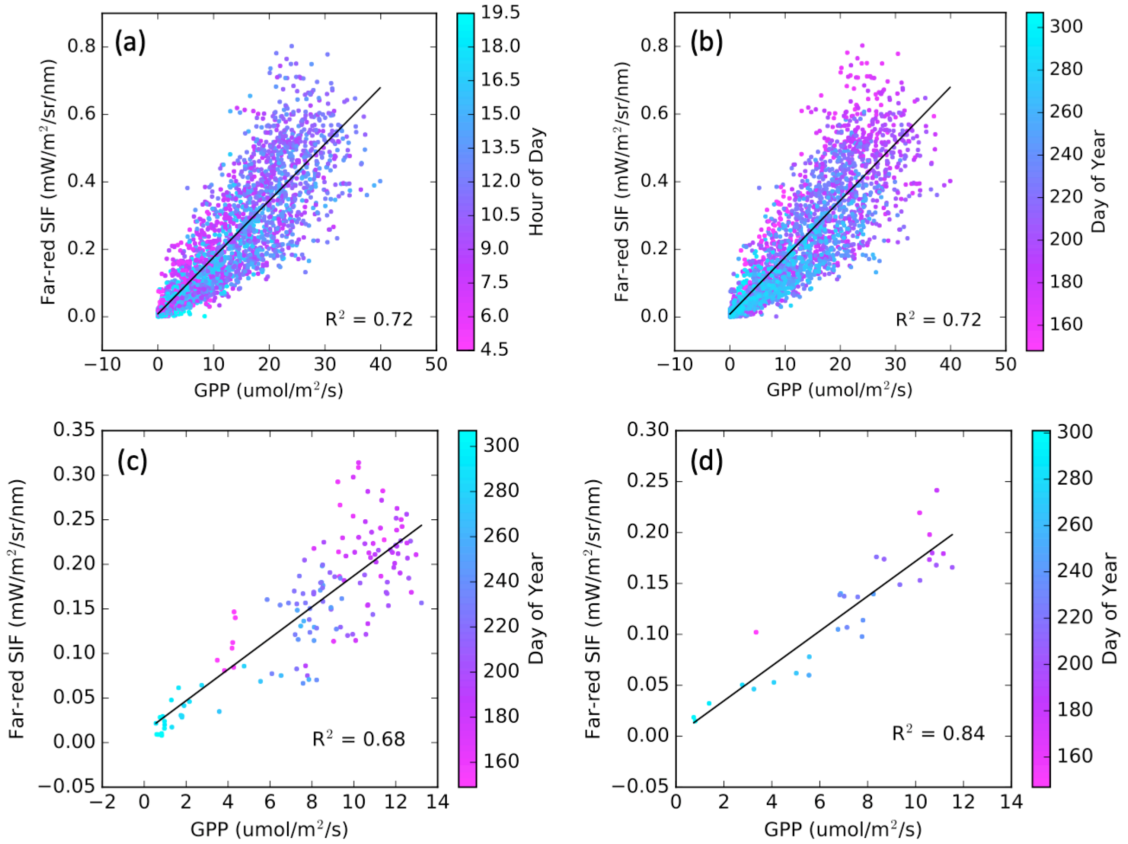

Fig. 3.3. Correlation plots between far-red SIF and GPP at 90 minute (a-b), daily (c), and weekly (d) temporal resolution observations. Color bars indicate hour of day (a) or day of year (b-d).

Direct correlations of far-red SIF with GPP confirmed strong agreement, consistent results with previous studies (e.g. X. Yang et al., 2015). We tested correlations with data aggregated to 90-minute, daily, and weekly timescales (Fig. 3.3). For far-red SIF, weekly-aggregated data had the highest correlation with GPP ($R^2 = 0.84$), while 90-minute- and daily-aggregated data had R^2 values of 0.72 and 0.68, respectively. The correlations between GPP and red SIF were much weaker (R^2 values of 0.33, 0.02, and 0.04 for 90-minute, daily, and weekly timescales; Fig. C1). We hypothesize that the strong correlation of far-red SIF with GPP at weekly timescales arises from the fact that this averaging window retains strong seasonal changes in light availability and absorption but averages out synoptic variability resulting from cloud cover. Over the period we collected observations, weekly values of far-red SIF span the range from near zero during the early and late growing season, to 0.2 mW/m^2/sr/nm during peak growing season in July (Fig. 3.3d). Daily values during the month of July, in contrast, have a standard deviation of ~0.05 mW/m^2/sr/nm and reach as high as 0.3 mW/m^2/sr/nm (Fig. 3.3c), suggesting that cloud-driven variability in PAR may be a significant driver in far-red SIF variability while GPP in this ecosystem may be less sensitive to day-to-day variability in light availability.

To investigate how seasonal changes influence the relationship between GPP and far-red SIF we tested linear correlations during individual months for 2018 and 2019 (Fig. 3.4). In order to approximate the uncertainties both on slopes and R^2 values we applied a bootstrapping approach in which we sampled the monthly data with replacement. Results for daily-averaged data confirmed that the strongest correlations occur in spring and fall, when seasonal dynamics lead to larger range of fPAR values within a given month (Fig. 3.4d; discussed in more detail in section 3.4.1). Correlations between 90-minute data showed that the inclusion of diurnal variations lead to consistently stronger correlations throughout the summer (Fig. 3.4b). The resulting slopes from the linear fits of daily data exhibited large uncertainties and do not exhibit obvious changes over the course of the growing season (Fig. 3.4c). Linear fits of 90-minute data were better constrained to the origin by including near-zero values in morning and evening, resulting in more precise slopes (Fig. 3.4a). These results showed that the far-red SIF:GPP slope declines over the course of the growing season (Fig. 3.4a).

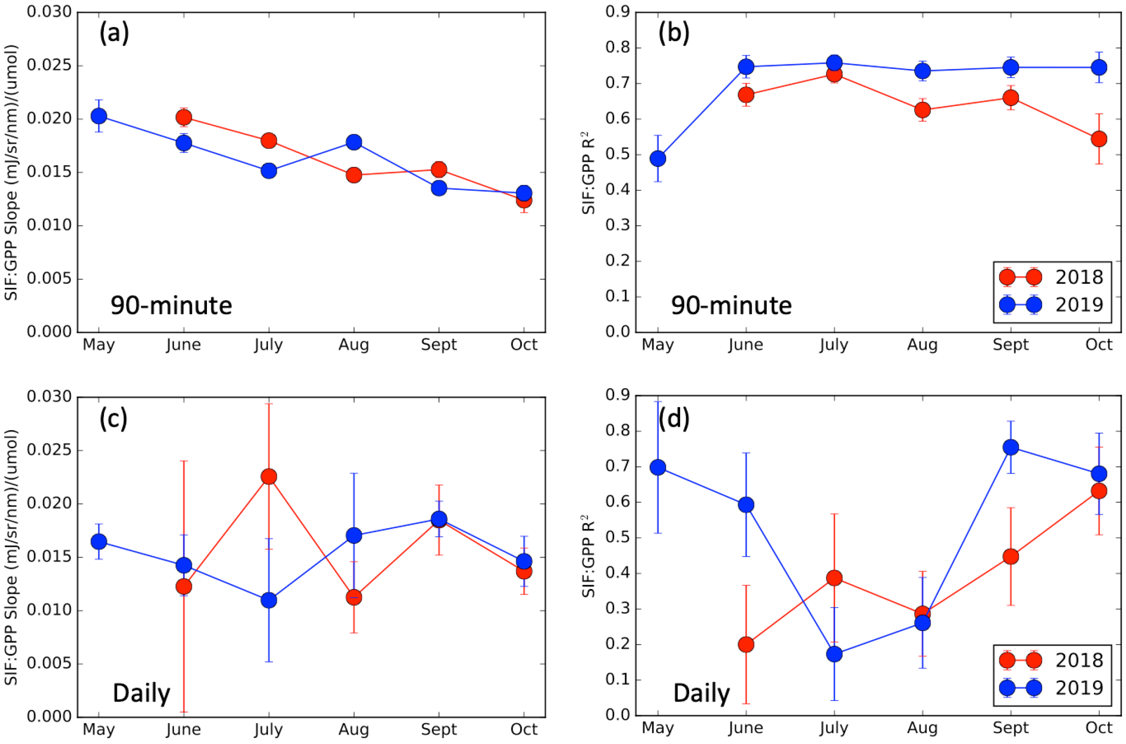

Fig. 3.4. Slopes and R^2 values from monthly linear regressions of 90-minute- (a-b) and daily-averaged (c-d) far-red SIF with GPP. Data from 2018 are in red, while 2019 data are in blue. Error bars represent the standard deviations of results from a bootstrapping method used to test the robustness of the linear regressions.

While both SIF and GPP depend on PAR (Eq. 3.1 and 3.2), correlations of SIF and GPP with downwelling PAR indicated that radiation is a stronger driver of SIF than of GPP (Fig. 3.5). While our site did not include direct observations of fPAR, we assumed that fPAR was near constant under peak growing season conditions when NDVI was stable (see Running et al., 2004;

Fig. 3.2i-j). The close dependence of SIF on radiation was illustrated by shared temporal patterns of SIF and PAR during summer (Fig. 3.2a-b, e-f), and by a strong correlation between daily-aggregated far-red SIF with PAR (R^2 = 0.90, Fig. 3.5a). GPP and PAR exhibited a much weaker correlation (R^2=0.55; Fig. 3.5b). Monthly correlations between far-red SIF and GPP with PAR show that both SIF and GPP exhibit weaker relationships with downwelling PAR during early spring and late fall (Fig. C2b, d), when NDVI (and fPAR) was more variable, as rapid changes in the canopy (i.e. leaf-out and senescence), rather than downwelling radiation, are a stronger driver of absorbed radiation during these periods. Lower NDVI (and fPAR) during spring and fall also led to lower values of SIF/PAR and GPP/PAR (Fig. C2a, c), as a smaller fraction of downwelling radiation is absorbed by vegetation during the shoulder seasons. Similar to far-red SIF, red SIF also exhibited a stronger relationship with PAR (R^2 = 0.37, Fig. C3) than with GPP (R^2 = 0.02, Fig. C1b).

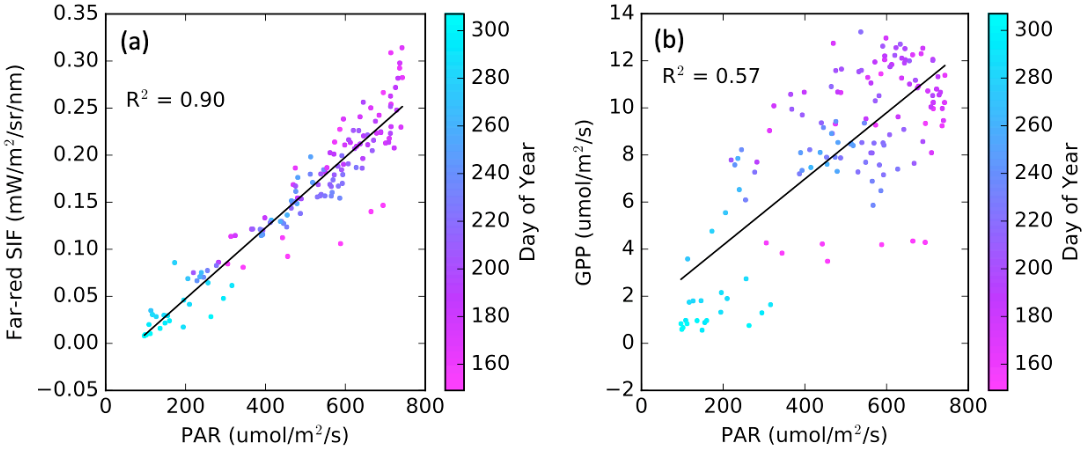

Fig. 3.5. Correlation plots between daily-averaged far-red SIF (a) and GPP (b) with photosynthetically active radiation (PAR). Color bars are weighted by day of year.

To isolate the SIF signal from PAR, we calculated the relative SIF by dividing the observed SIF irradiances by the total reflected irradiance, which provides an estimate of SIF as a percentage of reflected light (Fig. 3.2c-d). During 2018 and 2019, relative far-red SIF signals were generally stable throughout peak growing season conditions, but exhibited lower values during early spring and late fall, when the ecosystem absorbs less (and therefore reflects more) downwelling radiation. In contrast, relative red SIF increased over the course of the growing season, most notably in 2019, before decreasing in fall. This increase in relative red SIF was consistent with similar increases in the red:far-red SIF ratio (Fig. 3.2e-f).

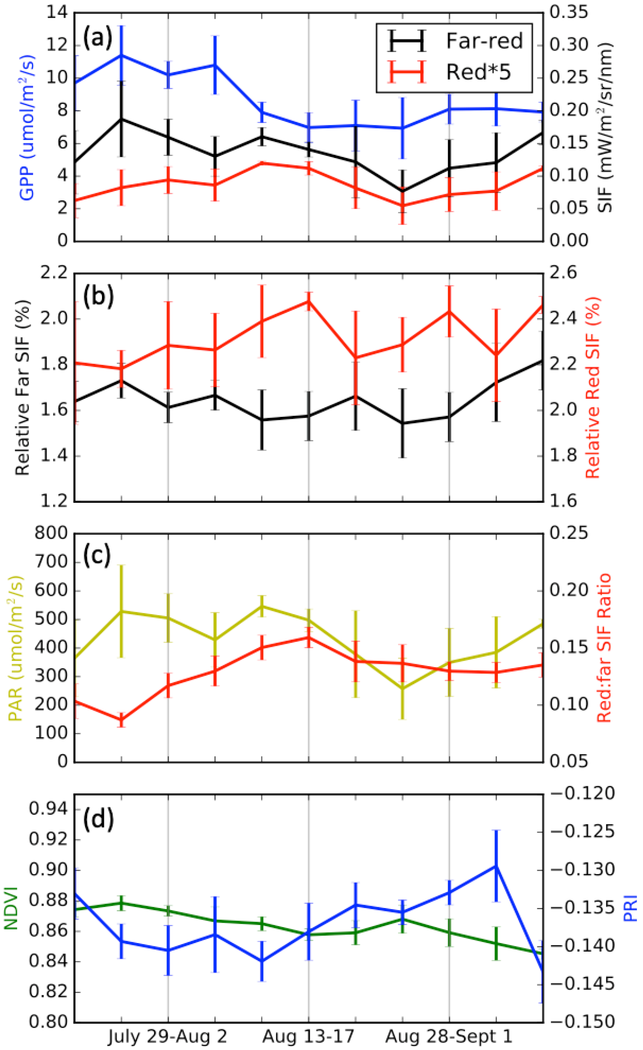

Fig. 3.6. Five-day binned data of GPP and SIF irradiance (a), relative SIF (b), and NDVI and the red:far-red SIF ratio (c) during drought conditions in August 2018. Error bars represent the standard deviation of 5-day bins.

3.3.3 Detectability of Mid-Summer Ecosystem Stress from SIF

While there were stress-induced decreases in GPP inferred from eddy covariance in both 2018 and 2019 (Fig. 3.2a-b; Section 3.1), these intraseasonal stress dynamics were not initially apparent in remote sensing observations made using the PhotoSpec. Both NDVI and PRI remained constant over the course of the growing season (Fig. 3.2i-j), indicating limited changes in chlorophyll and carotenoid pigments within the canopy, and changes in red and far-red SIF irradiances followed synoptic-scale patterns in downwelling PAR (Fig. 3.2a-b, e-f) rather than GPP.

To further investigate potential influences of drought stress on canopy SIF, we calculated 5-day binned averages of observed data over the course of the August 2018 drought (Fig. 3.6). GPP first experiences a decline around August 10 and recovers roughly 20 days later, but the far-red and red SIF irradiances exhibit higher (instead of lower) values over these 20 days (Fig. 3.6a). While higher SIF during a cloud- and precipitation-free period is consistent with the strong relationship with PAR demonstrated above, it was somewhat surprising that relative SIF signals were also insensitive to ecosystem stress and saw similar values during peak drought (August 15) and during recovery (August 30) (Fig. 3.6b). Our observations suggested that a more useful proxy for drought induced stress may be the red:far-red SIF ratio, which exhibited an increase coinciding with the August 2018 drought that was not affected by synoptic-scale noise (Fig. 3.6a, c). However, there was not an obvious signal in the red:far-red ratio during the less intense drought conditions in 2019. We looked at diurnal patterns before, during, and immediately after the August 2018 drought period and found that losses in GPP and increases in the red:far-red SIF ratio primarily stem from changes in the afternoon (Fig. 3.7), corroborating the hypothesis that

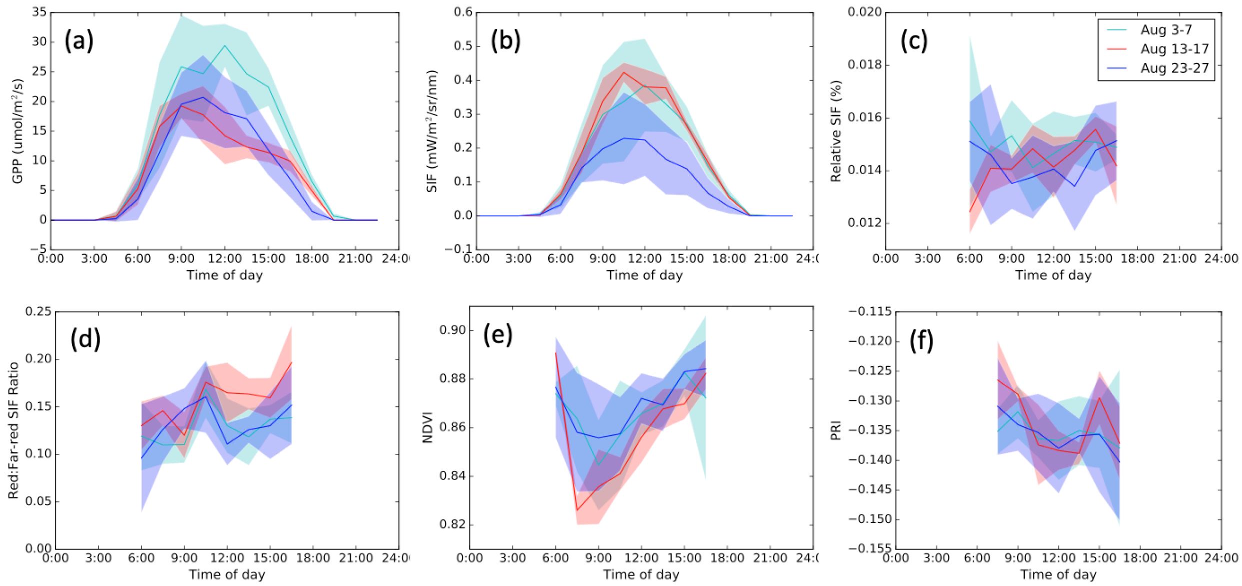

Fig. 3.7. Diurnal patterns of GPP, far-red SIF, relative far-red SIF, the red:far-red SIF ratio, NDVI, and PRI during certain 5-day bins spanning the August 2018 drought period. Included 5-day periods include before the drought (Aug 6-10), mid drought (Aug 16-20), and end of drought (Aug 26-30). Shaded region is +/- one standard deviation of the five days included.

changes in the SIF ratio are tied to ecosystem stress. While NDVI does exhibit lower morning values during the drought period, potentially resulting from leaf wilt, PRI and relative SIF did not show significant diurnal changes before, during, or after the drought period (Fig. 3.7). We note there is a delayed increase in PRI following the drought in early September may indicate an increase in carotenoid pigments resulting from the drought period. In contrast with these results, findings by Magney, Frankenberg, et al. (2019) showed that increased drought stress lead to a lower red:far-red SIF ratio at the leaf level, however they were unable to confirm this phenomenon with canopy-scale observations. Similarly, our 90-minute aggregated data across the full growing seasons do not indicate a clear diurnal response in the red:far-red SIF ratio to photosynthetic downregulation in the afternoon (Fig. C4, their Fig. 7b). However, that we see a higher red:far-red SIF ratio at synoptic scales during drought suggests contrasting behavior at the leaf and canopy scales.

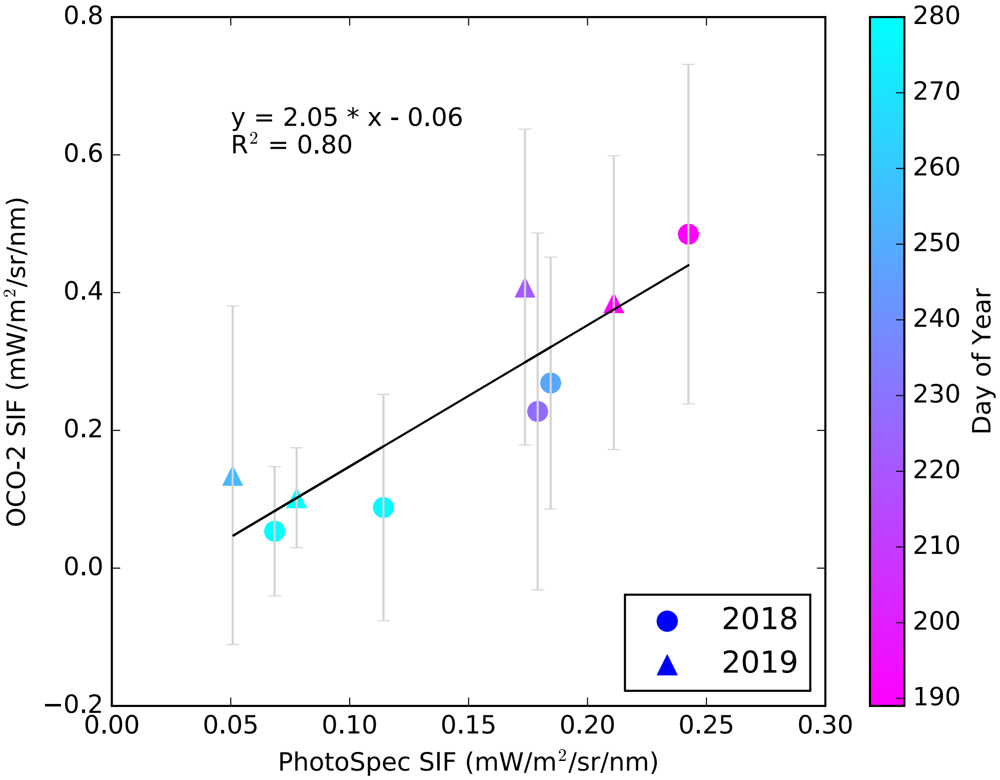

Fig. 3.8. Correlation plot and linear fit results between far-red SIF observations from PhotoSpec and the OCO-2 satellite. OCO-2 data includes soundings within a one-degree gridcell centered at US-UMB. Each sounding was multiplied by a daily correction factor, which uses a clear-sky proxy to account for diurnal changes in the SIF signal. Means were calculated from soundings across individual days, and error bars represent the standard deviation of included observations. Mean daily values from OCO-2 were then correlated with the daily-average SIF signal seen from the PhotoSpec instrument. Circles indicate data from 2018 and triangles indicate 2019. The color bar is weighted by day of year.

3.3.4 Comparison with OCO-2

Ultimately, an important goal of tower-based observations of SIF is to improve the interpretation and leveraging of space-based, global SIF observations. We compared our PhotoSpec observations of far-red SIF against SIF observations from the OCO-2 satellite (Fig. 3.7). The OCO-2 satellite observations were well correlated with our tower observations ($R^2 = 0.80$), but the slope between the two datasets was 2.0, reflecting that the raw SIF irradiance measured by

OCO-2 was twice as high as that measured by PhotoSpec. The lower irradiance values observed by our PhotoSpec instrument likely result from including a larger range of viewing angles in the calculation of daily-averaged SIF.

3.4. Discussion

3.4.1 Dependence of SIF and GPP on PAR

While many studies have emphasized the ability of SIF observations to estimate GPP from either satellite (e.g. Guanter et al., 2012; Sun et al., 2017) or tower (e.g. Magney, Bowling, et al., 2019; X. Yang et al., 2015) data, our results align with several studies that suggest that high correlations between SIF and GPP primarily result from a shared dependence on absorbed radiation or APAR (e.g. Wohlfahrt et al., 2018; K. Yang et al., 2018). That the linear relationship between SIF and GPP is largely driven by absorbed APAR is illustrated by stronger correlations between daily-averaged GPP with far-red SIF during spring and fall months (Fig. 3.4) when canopy changes drive large swings in fPAR. It also likely explains why correlations between far-red SIF and GPP were stronger for weekly-averaged data (which are sensitive to seasonal light variability) than for daily-averaged data, which reflect both seasonal and synoptic scale variations in light (Fig. 3.3).

That SIF is more closely tied to APAR than to GPP at our site was illustrated by daily-averaged SIF data being more strongly correlated with downwelling PAR ($R^2 = 0.90$; Fig. 3.5a), which was roughly proportional to APAR during peak summer conditions, than with GPP ($R^2 = 0.67$; Fig. 3.3b). Given that the correlation between GPP and PAR was significantly weaker (R^2

= 0.55; Fig. 3.5b), these results indicate that direct SIF observations contain limited information on LUE and may not be an effective indicator of synoptic-scale changes in productivity under conditions where canopy structure, chlorophyll content, and fPAR are generally stable. These results contrast with findings in X. Yang et al. (2015) who found only slightly weaker correlations between SIF and GPP than between SIF and APAR over another temperate deciduous location at Harvard Forest (US-Ha1). However, it should be noted that Harvard Forest is more radiation-limited than is our site (Wozniak et al., 2020), which would imply a closer coupling between variations in radiation and GPP at Harvard Forest. Similar to our results, although over a rice paddy rather than temperate forest, K. Yang et al. (2018) also found that SIF is better indicator of APAR rather than GPP. This caveat in the relationship between SIF and GPP indicates that SIF-derived estimates of productivity may not be free from the need for additional inputs, such as meteorological conditions that may signal ecosystem stress, as have been used for NDVI-derived estimates of GPP (see Running et al., 2004).

3.4.2 Relationship Between SIF and Ecosystem Productivity

One key result from this study is we did not find a constant relationship between far-red SIF and GPP over the course of the growing season. This is shown primarily by the slope of 90-minute far-red SIF:GPP linear fits consistently decreasing over the course of the growing season (Fig. 3.4a). While a seasonally changing relationship between SIF and productivity has been noted in previous studies (e.g. K. Yang et al., 2018), these studies occurred over cropland where such changes could be attributed to structural changes between different phenological stages. It is novel that we also see an evolving SIF:GPP relationship above a temperate deciduous forest where changes in canopy structure are minimal between leaf-out and senescence (typically late June through September). The lower ratio of SIF to GPP in fall suggests that assuming both variables are proportional may lead to an underestimate of fall productivity, as well as year-to-year variability. This could partially explain why interannual variability in satellite-based SIF observations is lower in fall than in spring, and exhibits weaker agreement with other vegetation-related remote sensing products (e.g. NDVI; see Butterfield et al., 2020) While some of the temporal behavior of the SIF:GPP relationship can likely be explained by drought and radiation effects (e.g. the higher SIF:GPP slope in August 2019 likely results from stress-induced declines in GPP that were not captured by the SIF signal), the generally decreasing SIF:GPP slope (Fig. 3.4a) may be due to leaf age effects and subtle changes in the canopy. These results are consistent with (Köhler, Guanter, et al., 2018) who hypothesize that leaf age is a key factor in understanding photosynthetic activity and SIF signals in the Amazon. In the future, leaf-level observations of fluorescence and pigment content, as well as long-term tower-based observations, may help to further elucidate the drivers of this behavior.

The challenges of using SIF to estimate productivity under stable canopy conditions were further illustrated by the limited response of red or far-red SIF signals to summer declines in GPP. When GPP declined in response to environmental stress at times during both years, SIF signals continued to reflect changes in radiation. Wohlfahrt et al. (2018) similarly found in a Mediterranean pine forest that SIF signals exhibited poor correlation with GPP during a heat wave, although their data indicated that that top-of-canopy SIF signals eventually declined in response to losses in productivity. At our temperate deciduous site, we did not observe declines in the SIF signal that could be easily attributed to the observed declines in GPP, consistent with Marrs et al. (2020), who demonstrated that SIF signals in individual deciduous species did not immediately respond to induced water stress. A potential explanation for this behavior is a lag between stomatal closure and drought-induced responses in the photosystems (and SIF_{yield}). The divergence in stress response between our results and Wohlfahrt et al. (2018) may reflect differences in timescale, i.e., the heatwave in their study occurred over a period of 8 days while our observations captured the effects of longer-term, cumulative drought stress, or from competing effects (further discussed in Section 3.4.3) that complicate attributing the behavior of relative SIF signals to specific drivers.

3.4.3 Applications of the Red:Far-Red SIF Ratio

Our results show that the red:far-red SIF ratio is sensitive to changes in canopy structure at both seasonal and interannual scales. Similar to Magney, Frankenberg, et al. (2019), we saw considerably higher red:far-red ratios during early spring canopy development, and in late fall as canopy chlorophyll content dropped, as lower leaf area and decreased chlorophyll content lead to decreased reabsorption of red SIF by the canopy. However, we also show that the red:far-red SIF ratio showed significant differences between 2018 and 2019, with 2019 ratios never reaching June 2018 values of <0.10. These year-to-year differences in the red:far-red SIF ratio are likely explained by 2018 having greater NDVI and LAI values (see section 3.3.2), in turn leading to variations in the canopy escape ratio for red fluorescence on interannual timescales. These results highlight the value in simultaneous retrievals of SIF at multiple wavelengths, as are becoming increasingly available from satellites such as TROPOMI (Köhler et al., 2020), but also demonstrate that the interpretation of SIF observations at multiple wavelengths must be cognizant of their sensitivity to ecosystem changes on synoptic, seasonal, and interannual timescales.

Our results suggest that the red:far-red SIF ratio may be more effective at detecting ecosystem stress than is far-red SIF alone, as a temporary increase in this ratio aligned closely with the August 2018 decrease in GPP (see section 3.3.3). Exploiting variations in the red:far-red SIF ratio to infer stress conditions, however, requires that observations be made at high temporal frequency since year-to-year or even month-to-month changes are primarily driven by changes in canopy structure that are independent from environmental stress. The increase in the red:far-red ratio during the drought period is consistent with findings in Wohlfahrt et al. (2018) who hypothesized that the contrasting response of SIF at different wavelengths may be due to a decrease in chlorophyll content leading to less reabsorption of red fluorescence. However, as in their study, this hypothesis is not obviously supported by significant changes in NDVI or PRI (Fig. 3.2i, 6c). This shared result between Wohlfahrt et al. (2018) and our study contrasts with Magney, Frankenberg, et al. (2019) who showed that stressed conditions lead to a lower red:far-red ratio at the leaf level, suggesting competing influences at leaf and canopy scales. These results echo the need for coordinated multi-scale investigation of the influence of ecosystem stress on photosynthetic machinery, the relationship between SIF and GPP under such conditions, and the drivers behind differing behaviors in red and far-red SIF, specifically through combining leaf-level measurements of fluorescence, chlorophyll content, and other parameters with synchronous observations at canopy and ecosystem scales.

3.5. Conclusions

We deployed a PhotoSpec system with two high spectral resolution spectrometers to measure red and far-red SIF to a deciduous forest in northern Michigan. Results from the first two years of data acquisition show that SIF signals over a temperate deciduous forest are more strongly related to radiation than to photosynthetic productivity. While a shared dependence on PAR does result in a significant correlation between SIF and GPP, this relationship gradually decreases over the course of the growing season, indicating that temporal changes in the far-red SIF:GPP ratio should be considered when using SIF to assess ecosystem productivity. We demonstrate challenges in using SIF irradiances to detect stress-induced declines in ecosystem productivity, but also show that simultaneous observations of both red and far-red SIF at high temporal frequency may be a better indicator of ecosystem stress than far-red SIF alone. Additionally, the red:far-red SIF ratio is sensitive to seasonal and interannual changes in canopy structure. Our results point to the need for coordinated multi-scale studies on the relationship between SIF and photosynthesis including at the leaf and canopy level, especially under conditions of environmental stress.

References

Aron, P. G., Poulsen, C. J., Fiorella, R. P., & Matheny, A. M. (2019). Stable Water Isotopes Reveal Effects of Intermediate Disturbance and Canopy Structure on Forest Water Cycling. *Journal of Geophysical Research: Biogeosciences*, *124*(10), 2958–2975.

Barr, A. G., Richardson, A. D., Hollinger, D. Y., Papale, D., Arain, M. A., Black, T. A., et al. (2013). Use of change-point detection for friction–velocity threshold evaluation in eddy-covariance studies. *Agricultural and Forest Meteorology*, *171*, 31–45.

Beck, P. S. A., Atzberger, C., Høgda, K. A., Johansen, B., & Skidmore, A. K. (2006). Improved monitoring of vegetation dynamics at very high latitudes: A new method using MODIS NDVI. *Remote Sensing of Environment*, *100*(3), 321–334.

Butterfield, Z., Buermann, W., & Keppel-Aleks, G. (2020). Satellite observations reveal seasonal redistribution of northern ecosystem productivity in response to interannual climate variability. *Remote Sensing of Environment*, *242*, 111755.

Dechant, B., Ryu, Y., Badgley, G., Zeng, Y., Berry, J. A., Zhang, Y., et al. (2020). Canopy structure explains the relationship between photosynthesis and sun-induced chlorophyll fluorescence in crops. *Remote Sensing of Environment*, *241*, 111733.

Fotis, A. T., Morin, T. H., Fahey, R. T., Hardiman, B. S., Bohrer, G., & Curtis, P. S. (2018). Forest structure in space and time: Biotic and abiotic determinants of canopy complexity and their effects on net primary productivity. *Agricultural and Forest Meteorology*, *250*, 181–191.

Frankenberg, C., Fisher, J. B., Worden, J., Badgley, G., Saatchi, S. S., Lee, J., et al. (2011). New global observations of the terrestrial carbon cycle from GOSAT: Patterns of plant fluorescence with gross primary productivity. *Geophysical Research Letters*, *38*(17).

Frankenberg, C., O'Dell, C., Berry, J., Guanter, L., Joiner, J., Köhler, P., et al. (2014). Prospects for chlorophyll fluorescence remote sensing from the Orbiting Carbon Observatory-2. *Remote Sensing of Environment*, *147*, 1–12.

Gamon, J. A., Field, C. B., Fredeen, A. L., & Thayer, S. (2001). Assessing photosynthetic downregulation in sunflower stands with an optically-based model. *Photosynthesis Research*, *67*(1–2), 113–125.

Gough, C., Bohrer, G., & Curtis, P. (2016). AmeriFlux US-UMB University of Michigan Biological Station. doi: 10.17190. *AMF/1246107*.

Gough, C. M., Hardiman, B. S., Nave, L. E., Bohrer, G., Maurer, K. D., Vogel, C. S., et al. (2013). Sustained carbon uptake and storage following moderate disturbance in a Great Lakes forest. *Ecological Applications*, *23*(5), 1202–1215.

Grossmann, K., Frankenberg, C., Magney, T. S., Hurlock, S. C., Seibt, U., & Stutz, J. (2018). Remote Sensing of Environment PhotoSpec : A new instrument to measure spatially distributed red and far- red Solar-Induced Chlorophyll Fluorescence. *Remote Sensing of Environment*, *216*(June), 311–327. https://doi.org/10.1016/j.rse.2018.07.002

Guanter, L., Frankenberg, C., Dudhia, A., Lewis, P. E., Gómez-Dans, J., Kuze, A., et al. (2012).

Retrieval and global assessment of terrestrial chlorophyll fluorescence from GOSAT space measurements. *Remote Sensing of Environment*, *121*, 236–251.

He, L., Ivanov, V. Y., Bohrer, G., Maurer, K. D., Vogel, C. S., & Moghaddam, M. (2014). Effects of fine-scale soil moisture and canopy heterogeneity on energy and water fluxes in a northern temperate mixed forest. *Agricultural and Forest Meteorology*, *184*, 243–256.

Joiner, J., Guanter, L., Lindstrot, R., Voigt, M., Vasilkov, A. P., Middleton, E. M., et al. (2013). Global monitoring of terrestrial chlorophyll fluorescence from moderate-spectral-resolution near-infrared satellite measurements: methodology, simulations, and application to GOME-2. *Atmospheric Measurement Techniques*, *6*(10), 2803–2823.

Köcher, P., Gebauer, T., Horna, V., & Leuschner, C. (2009). Leaf water status and stem xylem flux in relation to soil drought in five temperate broad-leaved tree species with contrasting water use strategies. *Annals of Forest Science*, *66*(1), 1.

Köhler, P., Guanter, L., Kobayashi, H., Walther, S., & Yang, W. (2018). Assessing the potential of sun-induced fluorescence and the canopy scattering coefficient to track large-scale vegetation dynamics in Amazon forests. *Remote Sensing of Environment*, *204*, 769–785.

Köhler, P., Frankenberg, C., Magney, T. S., Guanter, L., Joiner, J., & Landgraf, J. (2018). Global Retrievals of Solar-Induced Chlorophyll Fluorescence With TROPOMI: First Results and Intersensor Comparison to OCO-2. *Geophysical Research Letters*, *45*(19), 10–456.

Köhler, P., Behrenfeld, M. J., Landgraf, J., Joiner, J., Magney, T. S., & Frankenberg, C. (2020). Global Retrievals of Solar-Induced Chlorophyll Fluorescence at Red Wavelengths With TROPOMI. *Geophysical Research Letters*, *47*(15), e2020GL087541.

Lascano, R., Sojka, R. E., & Evett, S. (2007). Soil Water and Monitoring Technology. https://doi.org/10.2134/agronmonogr30.2ed.c2

Magney, T. S., Frankenberg, C., Köhler, P., North, G., Davis, T. S., Dold, C., et al. (2019). Disentangling changes in the spectral shape of chlorophyll fluorescence: Implications for remote sensing of photosynthesis. *Journal of Geophysical Research: Biogeosciences*, *124*(6), 1491–1507.

Magney, T. S., Bowling, D. R., Logan, B. A., Grossmann, K., Stutz, J., Blanken, P. D., et al. (2019). Mechanistic evidence for tracking the seasonality of photosynthesis with solar-induced fluorescence. *Proceedings of the National Academy of Sciences*, *116*(24), 11640–11645.

Marrs, J. K., Reblin, J. S., Logan, B. A., Allen, D. W., Reinmann, A. B., Bombard, D. M., et al. (2020). Solar-Induced Fluorescence Does Not Track Photosynthetic Carbon Assimilation Following Induced Stomatal Closure. *Geophysical Research Letters*, *47*(15), e2020GL087956.

Matheny, A. M., Fiorella, R. P., Bohrer, G., Poulsen, C. J., Morin, T. H., Wunderlich, A., et al. (2017). Contrasting strategies of hydraulic control in two codominant temperate tree species. *Ecohydrology*, *10*(3), e1815.

Miao, G., Guan, K., Yang, X., Bernacchi, C. J., Berry, J. A., DeLucia, E. H., et al. (2018). Sun-induced chlorophyll fluorescence, photosynthesis, and light use efficiency of a soybean field from seasonally continuous measurements. *Journal of Geophysical Research: Biogeosciences*, *123*(2), 610–623.

Porcar-Castell, A., Tyystjärvi, E., Atherton, J., Van der Tol, C., Flexas, J., Pfündel, E. E., et al. (2014). Linking chlorophyll a fluorescence to photosynthesis for remote sensing applications: mechanisms and challenges. *Journal of Experimental Botany*, *65*(15), 4065–4095.

Le Quéré, C., Andrew, R. M., Friedlingstein, P., Sitch, S., Pongratz, J., Manning, A. C., et al. (2018). Global Carbon Budget 2017. *Earth Syst. Sci. Data*, *10*, 405–448. https://doi.org/10.5194/essd-10-405-2018

Running, S. W., Nemani, R. R., Heinsch, F. A., Zhao, M., Reeves, M., & Hashimoto, H. (2004). A continuous satellite-derived measure of global terrestrial primary production. *AIBS Bulletin*, *54*(6), 547–560.

Ryu, Y., Berry, J. A., & Baldocchi, D. D. (2019). What is global photosynthesis? History, uncertainties and opportunities. *Remote Sensing of Environment*, *223*, 95–114.

Science Team, O.-2, Gunson, M., & Eldering, A. (2017). OCO-2 Level 2 bias-corrected solar-induced fluorescence and other select fields from the IMAP-DOAS algorithm aggregated as daily files, Retrospective processing V8r. Greenbelt, MD, USA: Goddard Earth Sciences Data and Information Services Center (GES DISC). Retrieved from 10.5067/AJMZO5O3TGUR

Song, L., Guanter, L., Guan, K., You, L., Huete, A., Ju, W., & Zhang, Y. (2018). Satellite sun-induced chlorophyll fluorescence detects early response of winter wheat to heat stress in the Indian Indo-Gangetic Plains. *Global Change Biology*, *24*(9), 4023–4037.

Sun, Y., Frankenberg, C., Wood, J. D., Schimel, D. S., Jung, M., Guanter, L., et al. (2017). OCO-2 advances photosynthesis observation from space via solar-induced chlorophyll fluorescence. *Science*, *358*(6360), eaam5747.

Sun, Y., Frankenberg, C., Jung, M., Joiner, J., Guanter, L., Köhler, P., & Magney, T. (2018). Overview of Solar-Induced chlorophyll Fluorescence (SIF) from the Orbiting Carbon Observatory-2: Retrieval, cross-mission comparison, and global monitoring for GPP. *Remote Sensing of Environment*, *209*, 808–823.

Wohlfahrt, G., Gerdel, K., Migliavacca, M., Rotenberg, E., Tatarinov, F., Müller, J., et al. (2018). Sun-induced fluorescence and gross primary productivity during a heat wave. *Scientific Reports*, *8*(1), 14169.

Wolf, S., Keenan, T. F., Fisher, J. B., Baldocchi, D. D., Desai, A. R., Richardson, A. D., et al. (2016). Warm spring reduced carbon cycle impact of the 2012 US summer drought. *Proceedings of the National Academy of Sciences*, *113*(21), 5880–5885.

Wozniak, M. C., Bonan, G. B., Keppel-Aleks, G., & Steiner, A. L. (2020). Influence of Vertical Heterogeneities in the Canopy Microenvironment on Interannual Variability of Carbon Uptake in Temperate Deciduous Forests. *Journal of Geophysical Research: Biogeosciences*, *125*(8), e2020JG005658.

Yang, K., Ryu, Y., Dechant, B., Berry, J. A., Hwang, Y., Jiang, C., et al. (2018). Sun-induced chlorophyll fluorescence is more strongly related to absorbed light than to photosynthesis at half-hourly resolution in a rice paddy. *Remote Sensing of Environment*, *216*, 658–673.

Yang, X., Tang, J., Mustard, J. F., Lee, J., Rossini, M., Joiner, J., et al. (2015). Solar-induced chlorophyll fluorescence that correlates with canopy photosynthesis on diurnal and seasonal scales in a temperate deciduous forest. *Geophysical Research Letters*, *42*(8), 2977–2987.

Yoshida, Y., Joiner, J., Tucker, C., Berry, J., Lee, J.-E., Walker, G., et al. (2015). The 2010 Russian drought impact on satellite measurements of solar-induced chlorophyll fluorescence: Insights from modeling and comparisons with parameters derived from satellite reflectances. *Remote Sensing of Environment*, *166*, 163–177.

Zeng, Y., Badgley, G., Dechant, B., Ryu, Y., Chen, M., & Berry, J. A. (2019). A practical approach for estimating the escape ratio of near-infrared solar-induced chlorophyll fluorescence. *Remote Sensing of Environment*, *232*, 111209.

Chapter 4

Diurnal and Directional Dependencies in SIF Irradiances Above a Temperate Deciduous Forest

Abstract

Solar-Induced chlorophyll Fluorescence (SIF) is increasingly being used as a proxy for photosynthetic activity and gross primary productivity (GPP). However, the SIF signal exhibits a dynamic diurnal cycle, and is sensitive to small-scale variation of vegetation type and canopy structure. Satellite-based remote sensing of SIF is limited in spatial and temporal resolution and may be sensitive to these small-scale effects. Moreover, space-based observation of SIF are generally scaled to a daily average using a clear-sky PAR proxy that neglects any diurnal asymmetries resulting from afternoon downregulation. In this study, we present analysis of tower-based observations of SIF using a PhotoSpec system deployed to the AmeriFlux site at the University of Michigan Biological Station (US-UMB) in the northern Lower Peninsula of Michigan. The PhotoSpec system allows for the observation of SIF at high temporal frequency and fine spatial resolution. We investigate how canopy structure, directional dependencies, and diurnal variations of photosynthesis and its drivers affect the SIF signal, and the implications that these influences have for the interpretation of SIF observations from space. We find that upscaling morning (afternoon) observations of SIF can result in an overestimate (underestimate) of daily average SIF by of 10% or more. Additionally, we demonstrate that SIF signals are

sensitive to sun-sensor geometry, with smaller incident angles between viewing direction and solar position, leading to higher observed SIF irradiances. However, these directional effects exhibit competing effects with afternoon drawdown effects, leading to an obfuscation of directional dependencies in the afternoon. Our findings show that SIF signals are sensitive to both diurnal and directional effects, as well as the interplay between them, and that accounting for these influences will improve our ability to effectively use the recent proliferation of satellite SIF observations.

4.1. Introduction

Carbon uptake via photosynthesis, or gross primary productivity (GPP), is the single largest carbon flux in the Earth system and is key to understanding the global carbon cycle and carbon-climate interactions (Beer et al., 2010), but is subject to significant uncertainty (Le Quéré et al., 2018). As land-atmosphere carbon exchange and GPP exhibit significant variability between different ecosystems and from year to year (e.g. Le Quéré et al., 2018; Running et al., 2004), quantifying GPP on a global scale requires widespread observations that are sensitive to variations across a range of temporal scales. Satellite-based instruments, because they obtain near global coverage with typical temporal return frequencies of 1-16 days, help meet these observational needs and have long been used to estimate ecosystem productivity via metrics such as the normalized difference vegetation index (NDVI) (Running et al., 2004).

Satellite-based observations of solar-induced chlorophyll fluorescence (SIF) provide another vegetation-related remote sensing observation, and have become increasingly available to the scientific community (Frankenberg et al., 2011; Joiner et al., 2013; Köhler et al., 2018;

Sun et al., 2017). SIF occurs as leaves absorb solar photons for use in photosynthesis, and subsequently reemit a fraction (1-2%) of those photons at red and far-red wavelengths. Several studies have shown that SIF scales with GPP over seasonal and daily timescales (Grossmann et al., 2018; Magney et al., 2019; Sun et al., 2017; Yang et al., 2015; Y. Zhang et al., 2016); however, observations of SIF are dependent on satellite- and instrument-specific characteristics that complicate using SIF irradiances to quantify GPP.

One challenge in interpreting satellite-based SIF observations results from dynamic diurnal patterns in both SIF and GPP. As GPP and SIF vary widely throughout the day with available photosynthetically active radiation (PAR), the magnitude of SIF depends strongly on the local time of observation. Thus, instantaneous satellite observations are typically converted to a daily-average signal by using the cosine of the solar zenith angle (SZA) to generate a clear-sky PAR proxy, which is then used to scale the SIF signal (Frankenberg et al., 2011; Köhler et al., 2018). This normalization or upscaling can be expressed as:

$$\overline{SIF} = SIF(t_m) * \frac{1}{\cos\left(SZA(t_m)\right)} \int_{t=t_m-12h}^{t=t_m+12h} \cos\left(SZA(t)\right) * H\left(\cos\left(SZA(t)\right)\right) dt \quad (4.1)$$

where SIF at the time of measurement, t_m, is converted to a daily average by dividing the instantaneous observation by the ratio of cos(SZA) at t_m to the daily average of cos(SZA). *H* is a Heaviside step function that zeros any negative values. This method assumes that the SIF signal is proportional to available radiation. However, afternoon down regulation of GPP has been well documented (Lin et al., 2019; Wagle & Kakani, 2014; Zhou et al., 2014), and diurnal hysteresis of SIF has also been reported, where morning SIF is higher than afternoon SIF at similar levels of PAR (Gu et al., 2019). The presence of asymmetries in diurnal cycles introduces the potential for bias when using a clear-sky PAR proxy to scale satellite-based SIF observations.

Satellite-based SIF data are also influenced by geometrical aspects of observations including canopy structure, solar position, and viewing angle. While SZA influences the intensity of downwelling PAR, the SIF signal is influenced by how sun-sensor geometry and canopy structure affect the ratio of sunlit and shaded vegetation included in observation footprints (He et al., 2017), as smaller incident angles between the direction of observation and incoming sunlight lead to a greater fraction of sunlit vegetation within the observational footprint. Zhang et al. (2018) demonstrated the importance of considering differences in observation angle by showing that the relationship of OCO-2 SIF and tower-based GPP estimates varied between different observational modes (i.e. glint and nadir) of OCO-2, with observations in glint mode having larger viewing zenith angles and exhibiting lower ratios of SIF to GPP. Newer satellites such as OCO-3 (Eldering et al., 2019) and future geostationary satellites (e.g. GeoCarb) (Moore III et al., 2018) observe the same location at different times of day across multiple days or may provide multiple observations of the same location within the same day. These characteristics may improve our ability to assess diurnal aspects of SIF signals, but the observations will also encompass a wider range of viewing angles. Thus, robust assessment of geometrical dependencies within SIF signals is needed for the effective interpretation of the data.

We examine diurnal and directional influences on SIF signals above a temperate deciduous forest using a PhotoSpec tower-based spectrometer system (Grossmann et al., 2018) at the University of Michigan Biological Station AmeriFlux tower (US-UMB). The PhotoSpec instrument obtains observations of SIF and other vegetation parameters at a high temporal resolution (~20 s), providing the opportunity to explore diurnal variability, and incorporates a 2-D scanning telescope allowing for the investigation of directional dependencies in vegetation signals.

In this study, we focus on the following science questions: 1) To what extent do diurnal asymmetries from afternoon downregulation impact the SIF signal, and what potential for bias does this create when scaling instantaneous measurements to daily averages? 2) How dependent are SIF observations on solar and viewing angles, and how does the perception of diurnal patterns in SIF change depending on viewing angle? 3) What implications do the previous questions have for using satellite-based SIF observations to assess GPP? In Section 4.2 we introduce our data and methods. We then present our results in Section 4.3. Section 4.4 contains a discussion of the implications of our findings, followed by a summary of our results in Section 4.5.

4.2. Data and Methods

4.2.1 Study Location and Tower-Based SIF Observations

As described in Chapter 3, SIF and other vegetation-related remote sensing observations were collected using a PhotoSpec spectrometer system (see also Grossmann et al., 2018) during the 2018 and 2019 growing season at the University of Michigan Biological Station AmeriFlux tower (US-UMB) in the Lower Peninsula of Michigan. Two narrowband spectrometers (QEPro, Ocean Optics Inc.) allowed for the retrieval of SIF irradiances at red (670-732 nm, 0.074 nm/pixel, 0.3 nm FWHM) and far-red (729-784 nm, 0.067 nm/pixel, 0.3 nm FWHM) wavelengths, while a broadband spectrometer (Flame, Ocean Optics Inc.; 177-874 nm, 0.382 nm/pixel, 1.2 nm FWHM) was used to calculate other vegetation parameters. Observations of

SIF in the far-red are primarily used for this study. Further information and calibration details are found in Chapter 3 and Appendix A.

The study location was a temperate deciduous forest consisting primarily aspen, maple, and oak, with a canopy height of ~20 m. The PhotoSpec instrument collected light samples using a narrow field-of-view (~0.7°) telescope, which could be moved to sample different locations of the canopy, that was mounted on the tower at a height of ~43 m. Individual observations had a footprint diameter on the order of 30 cm. Our data acquisition routine sequentially directed the telescope along three azimuthal scans (60° East of South, due South, 60° West of South) from nadir to 45° below the horizon, sampling at individual footprints for intervals of 20 s. Observations along each scan ranged between nadir and 45° below the horizon. As each azimuthal scan lasted ~30 minutes, the observation routine repeated every ~90 minutes, or roughly eight times per day.

Because the PhotoSpec telescope repeated azimuthal scans begining at nadir and panning upward to 45° below the horizon, this led to a saw tooth pattern imbedded in a typical diurnal cycle (see Fig. D1). This saw tooth pattern was partially due to local canopy geometry (nadir looked at the base of the tower and included less vegetation), but also contained directional influences (westward scans tended to increase when panning upward during the morning, but decrease when panning upward during the afternoon). Effects of this directional dependence were minimized in Section 4.3.1 and 4.3.2 by calculating 90-minute averages.

4.2.2 Eddy Covariance Flux GPP Observations

Concurrent eddy flux observations were available at the study site through the AmeriFlux network. For this study we used AmeriFlux-processed half-hourly GPP data, which relied on a neural network algorithm to estimate respiration from nighttime flux observations, allowing for the partitioning of daytime observations into respiration and GPP.

4.2.3 Clear-Sky PAR Proxy

Based on Eq. 4.1, we used the SZA associated with individual observations to generate a clear-sky PAR proxy, which was then used to downscale observations to estimates of a daily average. By applying this framework at various times of day and comparing with our actual daily-averaged data, we were able to test how effectively downscaled data estimated daily averages and explore the potential for bias when using this method to interpret satellite observations.

4.3. Results

4.3.1 Diurnal Influences

Tower-based observations of far-red SIF and GPP at US-UMB both exhibited afternoon values that were lower than morning despite similar SZA and PAR availability. When comparing monthly-averaged far-red SIF and GPP (Fig. 4.1) at specific times of day with the cos(SZA) for those observations, afternoon values were lower than morning values at similar SZA. For SIF, afternoon observations were as much as 20% lower than in morning during the middle of the growing season (i.e. July and August; Fig. 4.1a-b). At the beginning and end of the growing season differences between morning and afternoon SIF observations were less pronounced and typically < 10% (Fig. 4.1 a-b). For GPP observations, afternoon hysteresis is similarly more prominent during peak summer months, but exhibited more year-to-year variability between 2018 and 2019. For example, in August 2018 when the study site experienced drought (see Chapter 3), the GPP signal in the morning (cos(SZA) = 0.6) was more than 20 μmol m^{-2} s^{-1}, but dropped more than 25% to 15 μmol m^{-2} s^{-1} at the same SZA during the afternoon (Fig. 4.1c). In 2019, the difference between morning and afternoon GPP observations is < 15% (Fig. 4.1d). In contrast, the SIF signal saw similar differences (~20%) between morning and afternoon observations in both August 2018 and August 2019, suggesting that diurnal asymmetry in SIF signals are less sensitive to ecosystem stress.

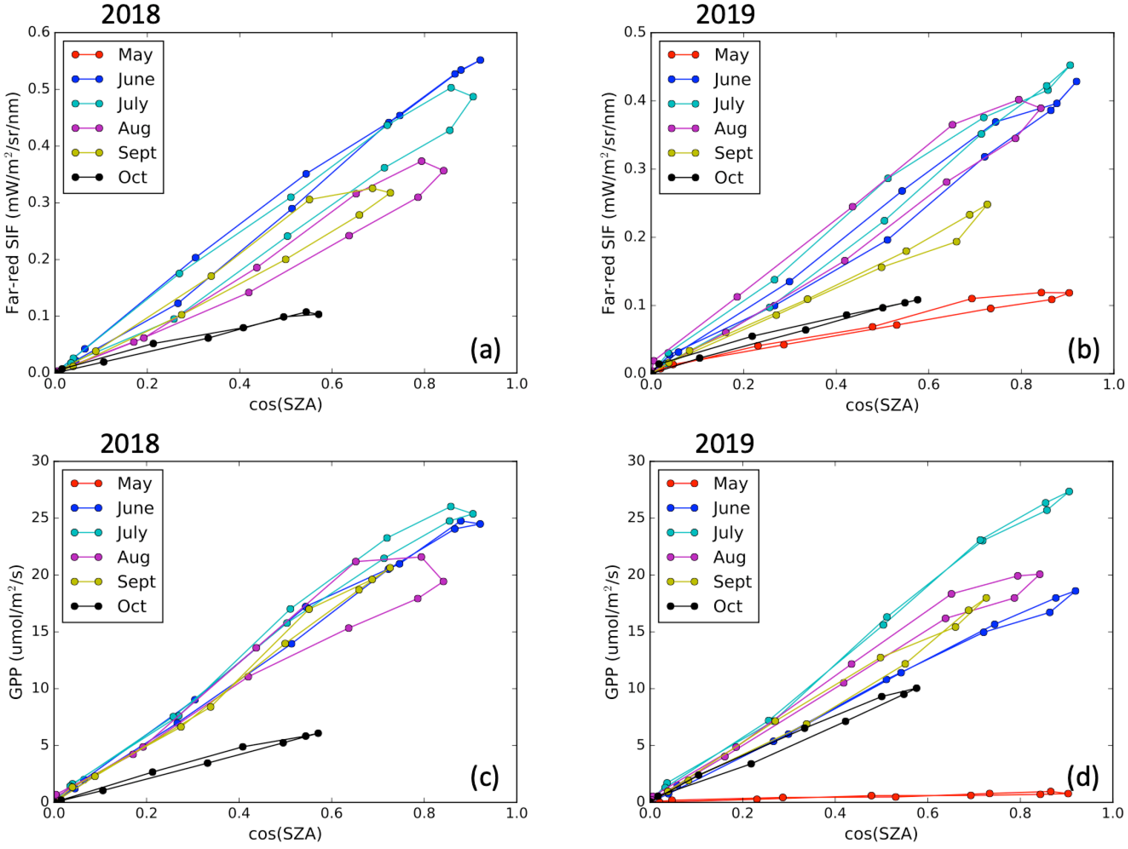

Fig. 4.1. Monthly mean diurnal patterns of far-red SIF (a-b) and GPP (c-d) plotted against the cosine of the solar zenith angle (SZA) for 2018 (left) and 2019 (right).

To explore how diurnal hysteresis influences the interpretation of instantaneous SIF observations, we applied a clear-sky PAR proxy (based on the SZA) to downscale observations at specific times of day and compared with the daily-averaged signal. Due to the dynamic diurnal cycle in SIF, 9:00am and 3:00pm signals are much higher than the 24-hr daily-averaged signal (Fig. D2a). While the upscaled values of SIF were closer to the same magnitude as daily averages (Fig. D2b), morning observations tended to lead to slightly higher daily estimates while afternoon values lead to slightly lower daily estimates. This likely stemmed from the clear-sky PAR normalization not accounting for diurnal hysteresis effects.

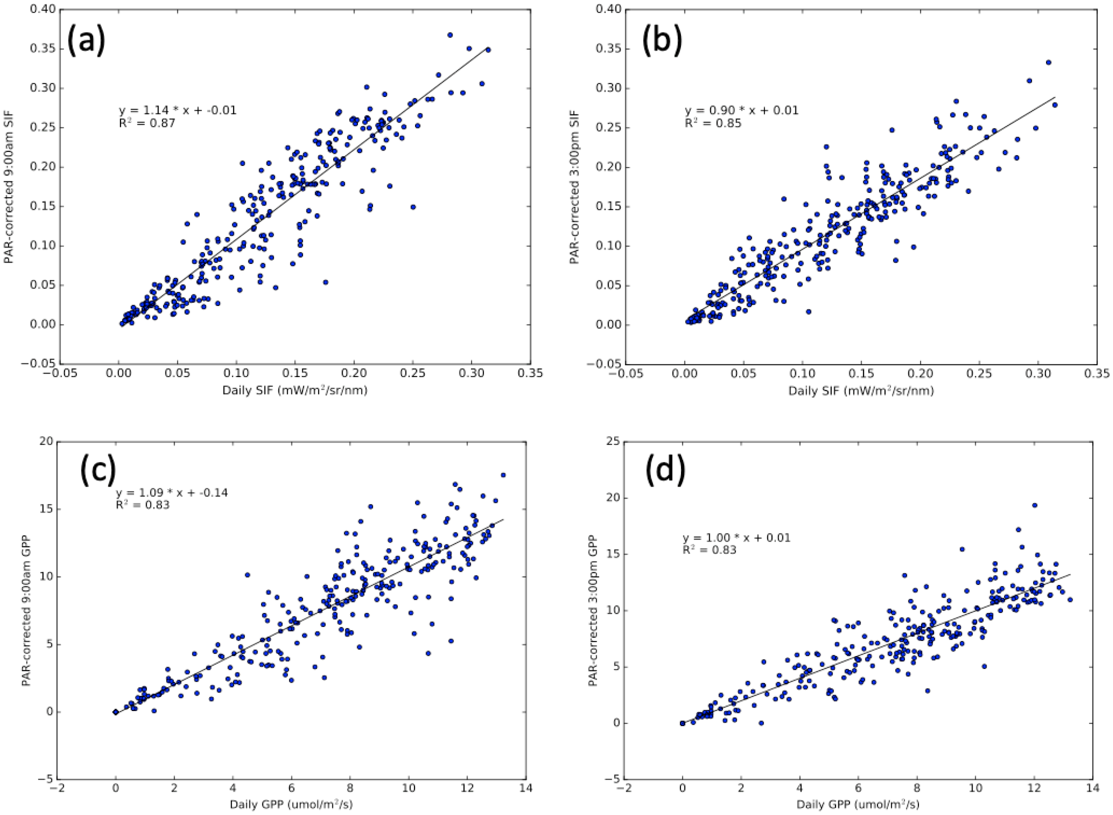

Fig. 4.2. Linear correlations between 9:00am (left panels) and 3:00pm (right panels) SIF (a-b) and GPP (c-d) observations with daily-averaged values. 9:00am and 3:00pm values were upscaled to daily estimates using a clear-sky PAR proxy based on the solar zenith angle.

To quantify the level of bias that clear-sky PAR normalization can induce in estimates of daily averages, we calculated linear regressions between upscaled observations at specific times of day and daily-averaged data. Ideally, the upscaled SIF and GPP would be related to the actual daily averages with a slope of one, but 9:00am and 3:00pm data resulted in slopes of 1.14 and 0.90, respectively (Fig. 4.2a, b). This indicates that applying a simple clear-sky PAR proxy to instantaneous SIF observations could lead to biases in daily average estimates of 10% or larger. When we upscaled morning GPP observations to calculate a daily average, we found a slope of 1.09 based on 9:00am observations (Fig. 4.2c). However, upscaling afternoon observations (3:00 pm) resulted in a slope of 1.0 with daily-averaged GPP (Fig. 4.2d), indicating that despite GPP being more susceptible to drought-induced decreases during the afternoon, upscaled afternoon observations were in good agreement with daily averages.

4.3.2. Diagnosing the Combined Influence of Diurnal and Directional Effects

In addition to being influenced by afternoon downregulation effects, the observed diurnal cycle of SIF can also be influenced by sun-sensor geometry, or the solar position, the viewing direction, and the incident angle between them. To explore the potential for viewing angle to bias the upscaled daily averages, we repeated the methods of Section 4.3.1 but only included observations of SIF at specific viewing angles. We calculated the mean of observations within 15° elevation intervals for each azimuthal scan in order to average out effects from small-scale canopy structure. We then tested the linear correlations from each viewing direction with the daily-averaged data across all elevation and azimuth angles (Fig. 4.3). In the final column, we incorporate all elevation and azimuth angles at specific times of day (compare with Fig 4.3a, b), in order to illustrate the influence of diurnal patterns independent of direction. By averaging across all angles, we found that the slope of upscaled SIF with daily averages decreases throughout the day, from 1.14 at 9:00-10:30am to 0.8 at 4:30-6:00pm (Fig. 4.3).

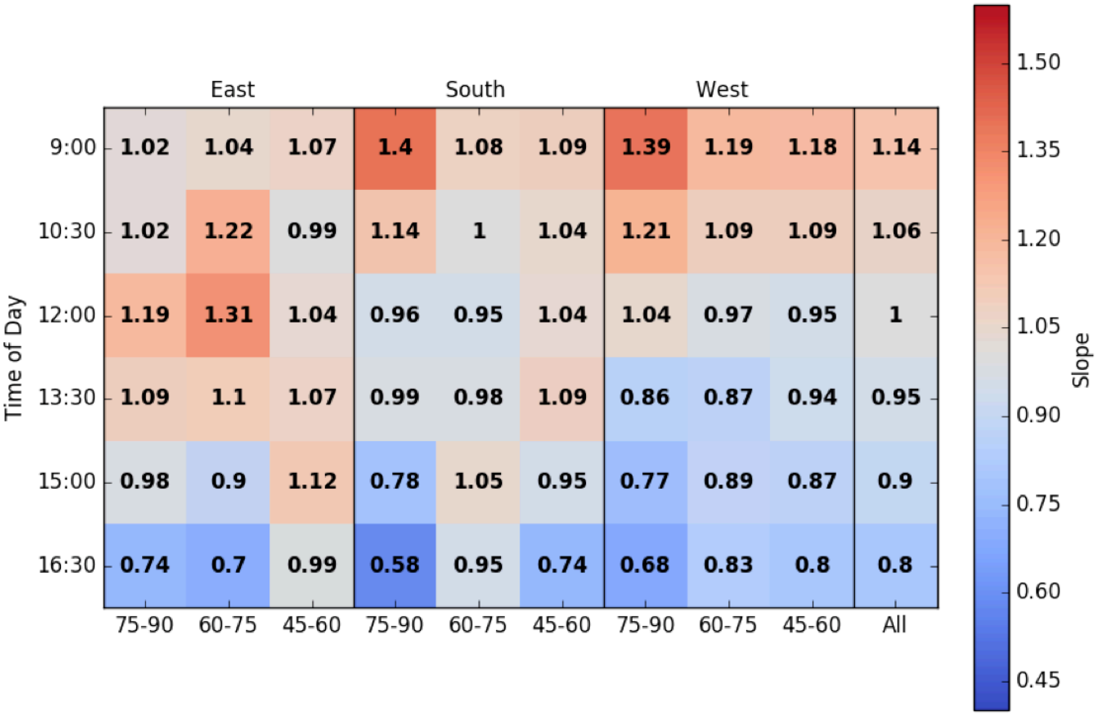

	East			South			West			
	75-90	60-75	45-60	75-90	60-75	45-60	75-90	60-75	45-60	All
9:00	1.02	1.04	1.07	1.4	1.08	1.09	1.39	1.19	1.18	1.14
10:30	1.02	1.22	0.99	1.14	1	1.04	1.21	1.09	1.09	1.06
12:00	1.19	1.31	1.04	0.96	0.95	1.04	1.04	0.97	0.95	1
13:30	1.09	1.1	1.07	0.99	0.98	1.09	0.86	0.87	0.94	0.95
15:00	0.98	0.9	1.12	0.78	1.05	0.95	0.77	0.89	0.87	0.9
16:30	0.74	0.7	0.99	0.58	0.95	0.74	0.68	0.83	0.8	0.8

Fig. 4.3. Slopes resulting from linear fits of PAR-corrected SIF signals at specific viewing angles and times of day against daily-averaged SIF observations. Columns indicate results from 75°-90°, 60°-75°, and 45°-60° below the horizon for three azimuthal scans of 60° east of south, due south, and 60° west of south. The final column includes all angles. Rows indicate time of day of included observations. Listed times of day indicate 90-minute intervals beginning at the time shown (9:00 indicates 9:00-10:30am, while 16:30 indicates 4:30-6:00pm).

Results from the west-facing azimuthal scan confirm that viewing vegetation from a west-facing direction can amplify biases already resulting from diurnal hysteresis, as the sun illuminates the east side of vegetation in morning when the SIF signal is strongest, leading to slopes ranging from > 1.18 at 9:00-10:30am to < 0.83 at 4:30-6:00pm (Fig. 4.3). However, these results are also in part influenced by the local structure of the canopy (i.e. shape of individual trees), which are difficult to separate from directional influences that would hold at larger scales.

These structural influences are indicated by differences in the NDVI signal within each azimuthal scan and are most prominent in the east-facing scan (Fig. D3). The results from the eastward azimuthal scan are subsequently less consistent between viewing angles, due to the less uniform canopy structure. However, morning observations from an east-facing direction are still less likely to overestimate daily-averages because the direction of illumination acts as a competing effect against the influence of diurnal downregulation. In other words, westward viewing angles lead to higher SIF signals in morning when the sun is in the east, whereas east-facing viewing angles exhibit weaker signals in morning as they primarily observe the west-facing, shaded side of vegetation. As discussed further in Section 4.4.2, the interplay between sun-sensor geometry and diurnal patterns should be considered as recent and future satellites (e.g. OCO-3, GeoCarb) allow for the study of diurnal patterns in SIF from space.

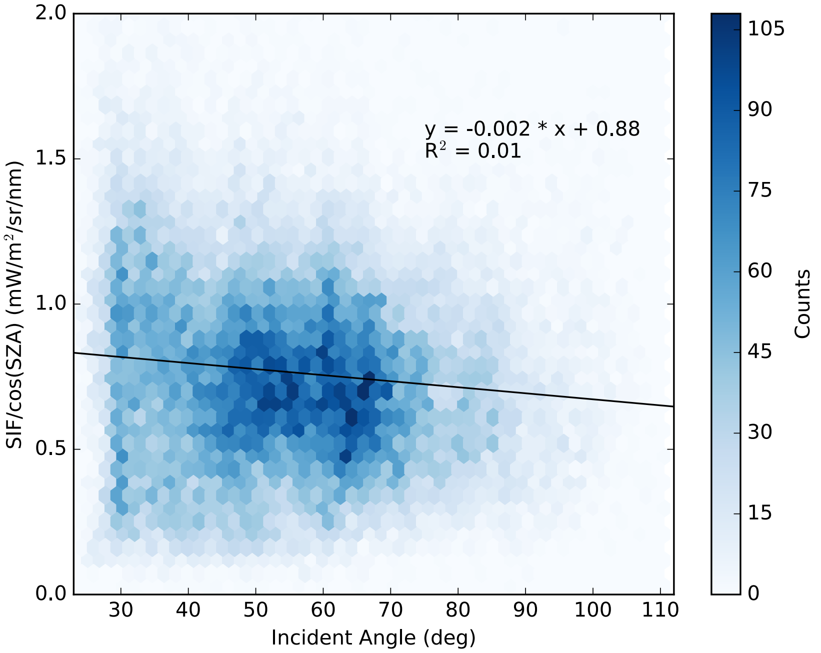

Fig. 4.4. Density scatter plot of far-red SIF divided by the cosine of the SZA against the incident angle between viewing direction and solar position. Data has been filtered to include only observations between 9:00am and 4:30pm, NDVI of greater than 0.82, and sunny conditions.

4.3.3 Directional Influences

To quantify the influence of sun-sensor geometry on our results, we explored how individual data points depended on the incident angle between the observational viewing angle and solar position. As single day timeseries of our original data is influenced both by the diurnal pattern of the SIF signal and by the solar and viewing angles (Fig. D1a), we first divided each data point by cos(SZA) (Fig. D1b). Dividing our SIF observations by cos(SZA) minimized the influence from solar intensity, thereby reducing the diurnal cycle, and isolating differences in signal level due to incident angle and canopy structure. Because we are interested in how observational and solar angles impact the magnitude of SIF observations, we applied a number of filters to remove non-angular effects (e.g. observing leaves vs. bark, seasonal patterns) that impact observed SIF irradiances. Thus, we removed any observations with NDVI values less than 0.8, thereby eliminating observations from early spring and late fall, and footprints directed at ground or bark. We also avoided low-light observations with poor data quality by only including data between 9:00am and 4:30pm local time under clear-sky conditions. The remaining data points have incident angles falling between 30° and 90°, and exhibit a negative slope (-0.002 mW m^{-2} sr^{-1} nm^{-1} deg^{-1}) with higher SIF signals correlating with lower angles between viewing direction and the sun (Fig. 4.4). While the poor R^2 value indicates that incident angle only describes ~1% of the variability in SIF/cos(SZA), the fit is statistically significant ($p<0.001$) owing to the large number of data. As discussed further in Section 4.4.2, an additional factor that may contribute noise in the relationship between SIF and incident angle is local canopy geometry influencing the times of day at which parts of the canopy are sunlit or shaded. For example, when viewing the east or west side of an individual tree, rather then the top, or viewing vegetation at a lower height than the rest of the canopy, incident angle alone can not fully represent how sunlit or shaded an individual observation will be. Despite the poor fit, the statistically significant negative slope demonstrates that smaller incident angles lead to higher SIF signals.

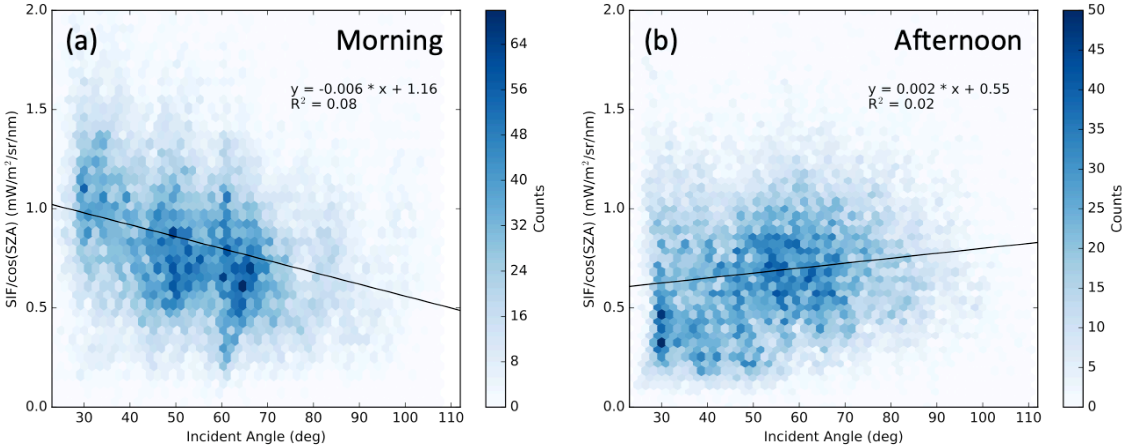

Fig. 4.5. Same as in Fig. 4.4, but separated by morning (a) and afternoon (b). Morning and afternoon were defined by a solar azimuth angle (SAZ) of less than or greater than 270°.

As demonstrated in Section 4.3.1, afternoon downregulation is another competing factor that complicates the perceived dependence of SIF signals on the incident angle of observation. By looking separately at morning (SAZ<180°) and afternoon (SAZ>180°) observations, we found that dependence on incident angle was more significant for morning data (Fig. 4.5). Morning data had a clear negative slope (-0.006 mW m^{-2} sr^{-1} nm^{-1} deg^{-1}) between SZA-normalized SIF with incident angle (Fig. 4.5a), three times greater than when including both morning and afternoon (Fig. 4.4). And although the R^2 value of 0.08 was still small it was more significant than for full day (Fig. 4.4) or afternoon observations (Fig. 4.5b). Illustrating the competing effects of afternoon downregulation, the fit of afternoon data exhibited a positive slope (0.002 mW m^{-2} sr^{-1} nm^{-1} deg^{-1}), likely because downregulation is less prominent as temperatures cool in the evening when observations are more likely to have wide incident angles. However, another complicating factor at our study site is that the forest canopy contained more gaps toward the east and was more uniform towards the west of the tower, as illustrated by lower NDVI values for the east-facing azimuthal scan (Fig. D3). Thus, lower incident angles during the morning are more likely to originate from west of the tower where the canopy is more vertically uniform and sunlit, while lower incident angles during the afternoon are more likely to originate from east of the tower where observations are more likely to include shaded gaps in the canopy.

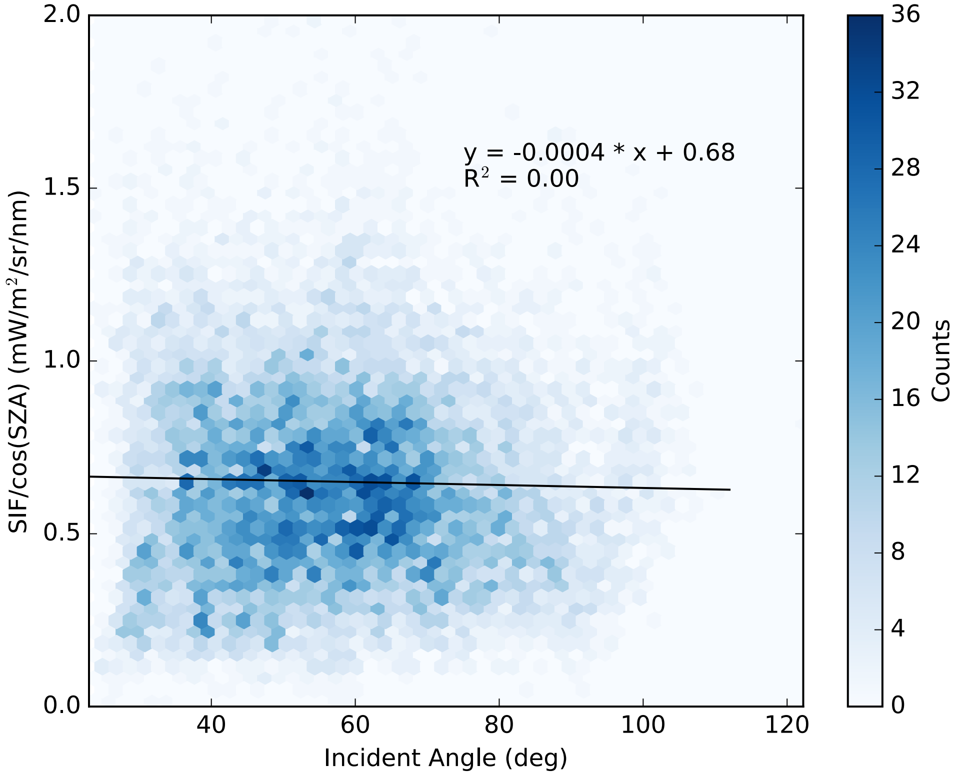

Fig. 4.6. Same as Fig. 4.4, but including moderately cloudy rather than sunny conditions. Moderately cloudy was defined as times when downwelling PAR values were between 75% and 90% of what would be expected under clear-sky conditions.

Finally, to explore how cloud cover influences dependencies on geometry, we also plotted SZA-normalized far-red SIF against the incident angle of observations under moderately cloudy conditions (Fig. 4.6). As clouds lead to more diffuse light and broaden the direction of downwelling radiation, we hypothesized that directional dependencies would be less significant under cloudy conditions relative to clear-sky. Similar to with clear-sky data, we removed footprints with NDVI<0.8. We then removed observations both under clear-sky conditions, and where downwelling PAR was less than 75% of what would be expected with clear sky. Consistent with our hypothesis, resulting data did not exhibit a clear dependence on incident angle with a linear fit resulting in near-zero values for both slope and R^2 value (Fig. 4.6).

4.4. Discussion

4.4.1 Diurnal Effects

A key result from our study is that diurnal hysteresis effects over temperate forest can lead to biases in daily-corrected SIF. As SIF experiences a dynamic diurnal cycle throughout the day, it is necessary to account for diurnal patterns when interpreting instantaneous satellite-based observations and using a clear-sky PAR proxy provides an efficient correction (Frankenberg et al., 2011; Köhler et al., 2018; Y. Zhang et al., 2018). Y. Zhang et al. (2018) demonstrated that these effects diurnal effects become important especially at high latitudes, as these regions see larger differences in length of day throughout the year. However, such methods ignore asymettries within the diurnal cycle. At our site we found that afternoon downregulation of the SIF signal lead to biased upscaled estimates of the daily-average SIF signal ranging from more than 110% in morning to less than 90% in the afternoon. These hysteresis effects should be taken into account when interpreting satellite observations, especially when comparing observations from different instruments or combining datasets to create extended observational timeseries (e.g. Parazoo et al., 2019). For example, as GOME-2 has an overpass time of ~9:30 am while

OCO-2 has an overpass time of ~1:30 (Sun et al., 2018), upscaling GOME-2 data based on PAR would lead to a high bias relative to actual daily mean (if one were observed), which is consistent with findings in Sun et al. (2018) where they found lower values of SIF for GOME-2 relative to OCO-2. While ecosystem modeling and tower-based observations at high temporal frequency provide avenues for evaluating the influence of hysteresis effects, future geostationary satellite missions may also provide opportunities to bridge the gap between satellite SIF observations at different times of day.

While both SIF and GPP values saw overestimates of daily values from upscaled morning observations, only SIF saw underestimates from upscaled afternoon observations, indicating that afternoon observations of SIF and GPP respond differently to drought stress. That GPP has a stronger diurnal response to drought is illustrated by SIF having more consistent diurnal patterns between 2018 and 2019, while GPP saw the most pronounced afternoon hysteresis in August 2018 when the US-UMB site experienced moderate drought (see Section 4.3.1; Chapter 3). The less sensitive diurnal response of SIF to drought underscores the uncertainty in using observations of SIF irradiances to detect drought-induced losses in GPP, supporting the conclusions of Chapter 3.

4.2 Directional Effects

While we found that diurnal hysteresis impacted the accuracy of using a clear-sky PAR proxy to upscale single observations of SIF to daily estimates, we also found that viewing angle of observations could also influence the perception of the diurnal pattern in SIF. This result has implications for the interpretation of observations at fixed viewing angles and suggests the potential for GeoCarb (Moore III et al., 2018), as an example, observing diurnal SIF patterns in its western field of view that skew towards morning, while diurnal SIF patterns in its eastern field of view would skew towards afternoon.

By normalizing SIF observations by the cosine of SZA and comparing with incident angle between viewing direction and solar position, we demonstrated that lower incident angles lead to higher observed SIF signals. While Gu et al. (2019) demonstrated that SIF observations were dependent on sun-sensor geometry, they only accounted for variations in solar and viewing zenith angles, without incorporating azimuth angles, and found varying dependencies on sun-sensor geometry over different ecosystems. We showed that these angular dependencies could be simplified by combining solar and viewing angles into a single incident angle, after accounting for differences in light intensity. Köhler et al. (2018) observed a similar pattern in TROPOMI data in the tropics (see their Fig. S6), and this directional influence was also shown using tropical GOSAT data in Guanter et al. (2012), where the highest observed SIF values were found to correlate with the same zenith angle as the sun (when incident angle was smallest). However, we have demonstrated that the influence that angle has on observations decreases under cloudy conditions when light is dispersed more broadly in the canopy, and have also shown that the relationship between SIF and viewing angle is strongest in morning data. The weaker relationship between incident angle and SIF observations during the afternoon indicates the competing effects between angular dependencies and diurnal hysteresis patterns.

One challenge in using tower-based data to explore directional effects in the SIF signal is that it is difficult to isolate directional influences from the influence of local canopy structure. While footprints that contain ground and bark can be easily filtered out using NDVI values, other aspects of vegetation structure (e.g. viewing the side or the crown of an individual tree) and not easily accounted for. This was demonstrated by differences in Fig. 4.4 that were likely due to our eastward and southward azimuthal scans including more gaps and shaded areas of the forest canopy. These ambiguities highlight the need to incorporate 3D canopy radiative transfer modeling (e.g. DART) (Gastellu-Etchegorry et al., 2015) for understanding the relationship between SIF, sun-sensor geometry, and canopy structure.

5. Conclusions

In this study we used tower-based observations of far-red SIF to demonstrate that the diurnal cycle of SIF over a temperate deciduous forest exhibits afternoon hysteresis patterns that influence how single observations should be upscaled to daily average estimates. As hysteresis leads to lower SIF signals in the afternoon, this can lead to high or low biases when using a clear-sky PAR proxy to scale morning or afternoon observations to 24-hr values. We also demonstrated that SIF observations are sensitive to sun-sensor geometry, and that these effects can interplay with diurnal patterns. While smaller angles between the sun and viewing direction lead to larger observed SIF values, afternoon hysteresis introduces a competing effect, leading to weaker angular dependencies in afternoon observations. Our results highlight the need for using canopy radiative transfer modeling to assess geometrical dependencies of SIF observations, and the need to consider both geometrical and diurnal influences in processing and interpreting satellite observations.

References

Beer, C., Reichstein, M., Tomelleri, E., Ciais, P., Jung, M., Carvalhais, N., et al. (2010). Terrestrial gross carbon dioxide uptake: global distribution and covariation with climate. *Science*, *329*(5993), 834–838.

Eldering, A., Taylor, T. E., O'Dell, C. W., & Pavlick, R. (2019). The OCO-3 mission: measurement objectives and expected performance based on 1 year of simulated data. *Atmospheric Measurement Techniques*, *12*(4).

Frankenberg, C., Fisher, J. B., Worden, J., Badgley, G., Saatchi, S. S., Lee, J., et al. (2011). New global observations of the terrestrial carbon cycle from GOSAT: Patterns of plant fluorescence with gross primary productivity. *Geophysical Research Letters*, *38*(17).

Gastellu-Etchegorry, J.-P., Yin, T., Lauret, N., Cajgfinger, T., Gregoire, T., Grau, E., et al. (2015). Discrete anisotropic radiative transfer (DART 5) for modeling airborne and satellite spectroradiometer and LIDAR acquisitions of natural and urban landscapes. *Remote Sensing*, *7*(2), 1667–1701.

Grossmann, K., Frankenberg, C., Magney, T. S., Hurlock, S. C., Seibt, U., & Stutz, J. (2018). Remote Sensing of Environment PhotoSpec : A new instrument to measure spatially distributed red and far- red Solar-Induced Chlorophyll Fluorescence. *Remote Sensing of Environment*, *216*(June), 311–327. https://doi.org/10.1016/j.rse.2018.07.002

Gu, L., Wood, J. D., Chang, C., Sun, Y., & Riggs, J. S. (2019). Advancing terrestrial ecosystem science with a novel automated measurement system for sun-induced chlorophyll fluorescence for integration with eddy covariance flux networks. *Journal of Geophysical Research: Biogeosciences*, *124*(1), 127–146.

Guanter, L., Frankenberg, C., Dudhia, A., Lewis, P. E., Gómez-Dans, J., Kuze, A., et al. (2012). Retrieval and global assessment of terrestrial chlorophyll fluorescence from GOSAT space measurements. *Remote Sensing of Environment*, *121*, 236–251.

He, L., Chen, J. M., Liu, J., Mo, G., & Joiner, J. (2017). Angular normalization of GOME-2 Sun-induced chlorophyll fluorescence observation as a better proxy of vegetation productivity. *Geophysical Research Letters*, *44*(11), 5691–5699.

Joiner, J., Guanter, L., Lindstrot, R., Voigt, M., Vasilkov, A. P., Middleton, E. M., et al. (2013). Global monitoring of terrestrial chlorophyll fluorescence from moderate-spectral-resolution near-infrared satellite measurements: methodology, simulations, and application to GOME-2. *Atmospheric Measurement Techniques*, *6*(10), 2803–2823.

Köhler, P., Frankenberg, C., Magney, T. S., Guanter, L., Joiner, J., & Landgraf, J. (2018). Global Retrievals of Solar-Induced Chlorophyll Fluorescence With TROPOMI: First Results and Intersensor Comparison to OCO-2. *Geophysical Research Letters*, *45*(19), 10–456.

Lin, C., Gentine, P., Frankenberg, C., Zhou, S., Kennedy, D., & Li, X. (2019). Evaluation and mechanism exploration of the diurnal hysteresis of ecosystem fluxes. *Agricultural and Forest Meteorology*, *278*, 107642.

Magney, T. S., Bowling, D. R., Logan, B. A., Grossmann, K., Stutz, J., Blanken, P. D., et al.

(2019). Mechanistic evidence for tracking the seasonality of photosynthesis with solar-induced fluorescence. *Proceedings of the National Academy of Sciences*, *116*(24), 11640–11645.

Moore III, B., Crowell, S. M. R., Rayner, P. J., Kumer, J., O'Dell, C. W., O'Brien, D., et al. (2018). The potential of the geostationary Carbon Cycle Observatory (GeoCarb) to provide multi-scale constraints on the carbon cycle in the Americas. *Frontiers in Environmental Science*, *6*, 109.

Parazoo, N. C., Frankenberg, C., Köhler, P., Joiner, J., Yoshida, Y., Magney, T., et al. (2019). Towards a harmonized long-term spaceborne record of far-red solar-induced fluorescence. *Journal of Geophysical Research: Biogeosciences*, *124*(8), 2518–2539.

Le Quéré, C., Andrew, R. M., Friedlingstein, P., Sitch, S., Pongratz, J., Manning, A. C., et al. (2018). Global Carbon Budget 2017. *Earth Syst. Sci. Data*, *10*, 405–448. https://doi.org/10.5194/essd-10-405-2018

Running, S. W., Nemani, R. R., Heinsch, F. A., Zhao, M., Reeves, M., & Hashimoto, H. (2004). A continuous satellite-derived measure of global terrestrial primary production. *AIBS Bulletin*, *54*(6), 547–560.

Sun, Y., Frankenberg, C., Wood, J. D., Schimel, D. S., Jung, M., Guanter, L., et al. (2017). OCO-2 advances photosynthesis observation from space via solar-induced chlorophyll fluorescence. *Science*, *358*(6360), eaam5747.

Sun, Y., Frankenberg, C., Jung, M., Joiner, J., Guanter, L., Köhler, P., & Magney, T. (2018). Overview of Solar-Induced chlorophyll Fluorescence (SIF) from the Orbiting Carbon Observatory-2: Retrieval, cross-mission comparison, and global monitoring for GPP. *Remote Sensing of Environment*, *209*, 808–823.

Wagle, P., & Kakani, V. G. (2014). Environmental control of daytime net ecosystem exchange of carbon dioxide in switchgrass. *Agriculture, Ecosystems & Environment*, *186*, 170–177.

Yang, X., Tang, J., Mustard, J. F., Lee, J., Rossini, M., Joiner, J., et al. (2015). Solar-induced chlorophyll fluorescence that correlates with canopy photosynthesis on diurnal and seasonal scales in a temperate deciduous forest. *Geophysical Research Letters*, *42*(8), 2977–2987.

Zhang, Y., Xiao, X., Jin, C., Dong, J., Zhou, S., Wagle, P., et al. (2016). Consistency between sun-induced chlorophyll fluorescence and gross primary production of vegetation in North America. *Remote Sensing of Environment*, *183*, 154–169.

Zhang, Y., Xiao, X., Zhang, Y., Wolf, S., Zhou, S., Joiner, J., et al. (2018). On the relationship between sub-daily instantaneous and daily total gross primary production: Implications for interpreting satellite-based SIF retrievals. *Remote Sensing of Environment*, *205*(December 2017), 276–289. https://doi.org/10.1016/j.rse.2017.12.009

Zhang, Z., Zhang, Y., Joiner, J., & Migliavacca, M. (2018). Angle matters: Bidirectional effects impact the slope of relationship between gross primary productivity and sun-induced chlorophyll fluorescence from Orbiting Carbon Observatory-2 across biomes. *Global Change Biology*, *24*(11), 5017–5020.

Zhou, S., Yu, B., Huang, Y., & Wang, G. (2014). The effect of vapor pressure deficit on water use efficiency at the subdaily time scale. *Geophysical Research Letters*, *41*(14), 5005–5013.

Chapter 5

Conclusions

The terrestrial biosphere at present provides a sink for as much as 30% of anthropogenic CO2 emissions; going forward, sensitivities of biospheric processes to environmental change will drive important feedbacks to climate change. As such, there is a need for observations that allow for the quantification of gross primary productivity (GPP) of ecosystems on regional and global scales. Longstanding satellite-based observations of the normalized difference vegetation index (NDVI) provide one such observation; however, NDVI only measures the fraction of photosynthetically active radiation (PAR) absorbed by vegetation and provides little information on light use efficiency (LUE), or the efficiency at which absorbed PAR is used to drive photosynthesis and carbon fixation. In contrast, solar-induced chlorophyll fluorescence (SIF) originates directly from the photosystems within leaves, and represents a promising remote sensing observation since it has been shown to scale with GPP on diurnal and seasonal timescales (Magney, Bowling, et al., 2019; Sun et al., 2017; X. Yang et al., 2015). While there is debate on whether the strong relationship between SIF and GPP is simply driven by a shared dependence on absorbed PAR (Wohlfahrt et al., 2018; K. Yang et al., 2018), there is evidence that SIF provides some level of information on LUE (X. Yang et al., 2015). However, uncertainties in the relationship between SIF and GPP warrant the assessment of SIF signals across multiple timescales and land cover types. This dissertation addressed the outstanding question of how SIF signals relate to GPP on interannual and intraseasonal timescales, when climate stress may impact the efficiency with which absorbed PAR is used for photosynthesis versus SIF. We focus specifically on SIF in Northern Hemisphere forest ecosystems.

5.1. Summary of Dissertation Conclusions

In Chapter 2, I showed that interannual variability in SIF observations from the GOME-2 (Global Ozone Monitoring Instrument-2) satellite (Joiner et al., 2013) are subject to signficiant uncertainty at the native resolution of GOME-2 observations (40 km x 40 km or 40 km x 80 km). This uncertainty contributes to poor correlations with longstanding satellite-based observations of the normalized difference vegetation index (NDVI) from MODIS (MODerate resolution Imaging Spectroradiometer) (Didan, 2015) and AVHRR (Advanced Very High Resolution Radiometer) (Pinzon & Tucker, 2014), near infrared reflectance of vegetation (NIR_V) (Badgley et al., 2017) from MODIS, and tower-based eddy covariance estimates of GPP (Baldocchi et al., 2001; Pastorello et al., 2017). Even when aggregating observations to a regional scale (5° x 10°), different satellite-based observations often showed poor correlations among their respective IAV timeseries, especially for summer and growing season-integrated values. These findings highlight the need to consider the scales at which SIF observations provide meaningful information, and suggest that currently available datasets do not provide robust measures of interannual variability at less than regional spatial scales.

Despite the challenges in using currently available satellite observations to study interannual variability of vegetation signals, I was able to extract meaningful relationships between vegetation and climate variability using a statistical approach (singular value decomposition; SVD) (Golub & Reinsch, 1971). By applying an SVD framework to regionally aggregated timeseries of SIF, NDVI, and NIR_V, I found two common seasonal modes of variability that were consistent across datasets. The first of these was a redistribution mode, where increases (decreases) in spring productivity were associated with decreases (increases) in productivity during late summer and fall. As spring gains (losses) in productivity balanced with fall losses (gains), this seasonal mode had a limited impact on growing-season integrated signals and was found to correlate with above-average spring and summer temperatures and lower moisture availability in fall. Additionally, redistribution was found to be more prominent at lower latitudes, indicating that it may play a greater role under warmer climate conditions. The second common mode of interannual variability was an amplification effect, representing a broad increase (decrease) of summer productivity. Amplification was more strongly correlated with summer moisture availability, suggesting that GPP when integrated across the growing season may be more sensitive to moisture than to temperature.

While the results shown in Chapter 2 are limited to regional spatial scales, in Chapters 3 and 4 I investigated SIF signals and their relationship to ecosystem productivity at the local scale using a tower-based PhotoSpec spectrometer system (Grossmann et al., 2018; Appendix A). I built and deployed the PhotoSpec instrument above a temperate deciduous forest in the northern Lower Peninsula of Michigan on the AmeriFlux tower at the University of Michigan Biological Station (US-UMB). This allowed for the comparison of PhotoSpec observations of red and far-red SIF, as well as vegetation indices including NDVI, alongside eddy-flux estimates of GPP, soil moisture, and other ancillary data. Additionally, the PhotoSpec instrument acquired observations via a 2-D scanning telescope, allowing for the exploration of directional dependencies within the SIF signals.

In Chapter 3 of this dissertation, I showed that SIF signals were more strongly correlated with downwelling PAR than with GPP, and did not exhibit obvious responses to synoptic-scale changes in summer productivity. This decoupling of SIF and GPP signals during summer lead to weaker correlations relative to those during spring and fall months, echoing the findings of Chapter 2, wherein satellite observations of vegetation exhibited the weakest correlations between datasets during summer. Although SIF irradiances did not exhibit strong responses to water stress, I found that an enhancement in the red:far-red SIF ratio did align with a period of drought. These findings highlight the value in simultaneous retrievals of SIF at multiple wavelengths, and suggest that the red:far-red ratio may serve as a better indicator of drought stress than SIF irradiance alone.

Lastly, in Chapter 4, I demonstrated that SIF signals are subject to diurnal hysteresis patterns that lead to lower signals during the afternoon. As satellite observations typically are scaled to daily estimates using a clear-sky PAR proxy (Frankenberg et al., 2011; Köhler et al., 2018), this method has the potential to overestimate (underestimate) SIF when scaling morning (afternoon) observations to daily averages. Additionally, I showed that observed SIF signals are dependent on the incident angle between viewing direction and solar position, with smaller incident angles leading to higher SIF irradiances. These directional aspects of the SIF signal exhibited competing effects with diurnal patterns, which tended to obfuscate directional dependencies during the afternoon.

5.2. Directions for Future Research

One of the challenges in Chapter 2 was that meaningful interannual signals did not emerge from GOME-2 SIF observations until they were regionally aggregated. Chapter 2 included observations from GOME-2 because it provides the longest continuous timeseries of SIF to date, since launching in October 2006, and we successfully demonstrated potential for using satellite observations for studies of interannual variability. However, while GOME-2 currently collects observations with a footprint size of 40 km x 40 km and typically obtains 10-25 individual soundings in any 0.5° gridcell per month, more recent satellites provide SIF observations at significantly higher temporal frequency and finer spatial resolution. OCO-2, which launched in July 2014, collects observations with a footprint size of 1.3 km x 2.25 km on a 16-day repeat cycle (Frankenberg et al., 2014), and TROPOMI, which launched in October 2017, has an observation footprint of 7 km x 3.5 km at nadir and provides near-daily global coverage. Over the next few years, studies of interannual variability will become more feasible using these additional satellites, which will provide opportunities to investigate the carbon-climate interactions discussed in Chapter 2 at much finer spatial scales. This will allow for better comparison with ground-based observations (e.g. eddy flux networks and tower-based remote sensing), and validation of the mechanisms behind the patterns of interannual variability that we observed.

Alternatively, studies of interannual variability may be furthered through the combination of data from multiple satellites into single timeseries. As such, there is interest in combining SIF observations from multiple satellites (Parazoo et al., 2019), or in using machine learning approaches to combine SIF with vegetation indices to create extended timeseries (Li & Xiao, 2019). As Chapter 2 demonstrated, however, different satellite datasets are subject to unique instrumental and sensor characteristics that complicate direct comparisons, even when two instruments observe the same phenomenon. Chapter 4 presented a framework for assessing diurnal and directional aspects of the SIF signal that likely contribute to differences between satellite observations over temperate deciduous forest. As my PhotoSpec instrument at the University of Michigan Biological Station AmeriFlux tower (US-UMB) has been included as a target for the OCO-3 instrument aboard the International Space Station (ISS) beginning in late 2019, there are future opportunities to explore how these directional and diurnal effects scale to space-based observations using data from OCO-3, as well as from TROPOMI.

At the local scale, there is also a wealth of ancillary data at US-UMB that has not been included in this dissertation, often due to lags in processing time. One such dataset is a LiDAR characterization (Atkins et al., 2018) of canopy structure along the transects observed by the PhotoSpec instrument. As local canopy structure very likely contributes to the noise seen in the directional relationships found in Chapter 4, combining canopy LiDAR data with 3-D radiative transfer modeling (e.g. DART; Gastellu-Etchegorry et al., 2015) would serve to improve an understanding of these relationships and better explore how they would scale to satellite observations.

While it is valuable to understand how differences in scale between space-based and tower-based observations influence scientific findings, investigating how canopy observations scale to the individual species and leaf level is another critical step towards understanding the biological mechanisms behind SIF and its relation to GPP. Although not included in this dissertation, sap flow data at US-UMB (Matheny et al., 2017) may provide one avenue for connecting GPP signals to hydraulic function of individual species. And, as discussed in Chapter 3, concurrent leaf-level observations of fluorescence and pigment (e.g. chlorophyll and carotenoids) content would be a future strategy for testing hypotheses behind drought-induced changes in SIF signals. Ultimately, my tower-based observations of SIF at US-UMB serve as a valuable link between local ecosystem function and satellite observations, and provide many avenues for future research.

References

Atkins, J. W., Bohrer, G., Fahey, R. T., Hardiman, B. S., Morin, T. H., Stovall, A. E. L., et al. (2018). Quantifying vegetation and canopy structural complexity from terrestrial Li DAR data using the forestr r package. *Methods in Ecology and Evolution*, *9*(10), 2057–2066.

Badgley, G., Field, C. B., & Berry, J. A. (2017). Canopy near-infrared reflectance and terrestrial photosynthesis. *Science Advances*, *3*(3), e1602244.

Baldocchi, D., Falge, E., Gu, L., Olson, R., Hollinger, D., Running, S., et al. (2001). FLUXNET: A new tool to study the temporal and spatial variability of ecosystem-scale carbon dioxide, water vapor, and energy flux densities. *Bulletin of the American Meteorological Society*, *82*(11), 2415–2434.

Didan, K. (2015). MOD13C2 MODIS/Terra vegetation indices monthly L3 global 0.05 deg CMG V006. *NASA EOSDIS Land Processes DAAC, Doi*, *10*.

Frankenberg, C., Fisher, J. B., Worden, J., Badgley, G., Saatchi, S. S., Lee, J., et al. (2011). New global observations of the terrestrial carbon cycle from GOSAT: Patterns of plant fluorescence with gross primary productivity. *Geophysical Research Letters*, *38*(17).

Frankenberg, C., O'Dell, C., Berry, J., Guanter, L., Joiner, J., Köhler, P., et al. (2014). Prospects for chlorophyll fluorescence remote sensing from the Orbiting Carbon Observatory-2. *Remote Sensing of Environment*, *147*, 1–12.

Gastellu-Etchegorry, J.-P., Yin, T., Lauret, N., Cajgfinger, T., Gregoire, T., Grau, E., et al. (2015). Discrete anisotropic radiative transfer (DART 5) for modeling airborne and satellite spectroradiometer and LIDAR acquisitions of natural and urban landscapes. *Remote Sensing*, *7*(2), 1667–1701.

Golub, G. H., & Reinsch, C. (1971). Singular value decomposition and least squares solutions. In *Linear Algebra* (pp. 134–151). Springer.

Grossmann, K., Frankenberg, C., Magney, T. S., Hurlock, S. C., Seibt, U., & Stutz, J. (2018). Remote Sensing of Environment PhotoSpec : A new instrument to measure spatially distributed red and far- red Solar-Induced Chlorophyll Fluorescence. *Remote Sensing of Environment*, *216*(June), 311–327. https://doi.org/10.1016/j.rse.2018.07.002

Joiner, J., Guanter, L., Lindstrot, R., Voigt, M., Vasilkov, A. P., Middleton, E. M., et al. (2013). Global monitoring of terrestrial chlorophyll fluorescence from moderate-spectral-resolution near-infrared satellite measurements: methodology, simulations, and application to GOME-2. *Atmospheric Measurement Techniques*, *6*(10), 2803–2823.

Köhler, P., Frankenberg, C., Magney, T. S., Guanter, L., Joiner, J., & Landgraf, J. (2018). Global Retrievals of Solar-Induced Chlorophyll Fluorescence With TROPOMI: First Results and Intersensor Comparison to OCO-2. *Geophysical Research Letters*, *45*(19), 10–456.

Li, X., & Xiao, J. (2019). A Global, 0.05-Degree Product of Solar-Induced Chlorophyll Fluorescence Derived from OCO-2, MODIS, and Reanalysis Data. *Remote Sensing*, *11*(5), 517.

Magney, T. S., Frankenberg, C., Köhler, P., North, G., Davis, T. S., Dold, C., et al. (2019). Disentangling changes in the spectral shape of chlorophyll fluorescence: Implications for remote sensing of photosynthesis. *Journal of Geophysical Research: Biogeosciences*, *124*(6), 1491–1507.

Magney, T. S., Bowling, D. R., Logan, B. A., Grossmann, K., Stutz, J., Blanken, P. D., et al. (2019). Mechanistic evidence for tracking the seasonality of photosynthesis with solar-induced fluorescence. *Proceedings of the National Academy of Sciences*, *116*(24), 11640–11645.

Matheny, A. M., Fiorella, R. P., Bohrer, G., Poulsen, C. J., Morin, T. H., Wunderlich, A., et al. (2017). Contrasting strategies of hydraulic control in two codominant temperate tree species. *Ecohydrology*, *10*(3), e1815.

Moore III, B., Crowell, S. M. R., Rayner, P. J., Kumer, J., O'Dell, C. W., O'Brien, D., et al. (2018). The potential of the geostationary Carbon Cycle Observatory (GeoCarb) to provide multi-scale constraints on the carbon cycle in the Americas. *Frontiers in Environmental Science*, *6*, 109.

Parazoo, N. C., Frankenberg, C., Köhler, P., Joiner, J., Yoshida, Y., Magney, T., et al. (2019). Towards a harmonized long-term spaceborne record of far-red solar-induced fluorescence. *Journal of Geophysical Research: Biogeosciences*, *124*(8), 2518–2539.

Pastorello, G., Papale, D., Chu, H., Trotta, C., Agarwal, D., Canfora, E., et al. (2017). The FLUXNET2015 dataset: The longest record of global carbon, water, and energy fluxes is updated. *Eos*, *98*.

Pinzon, J., & Tucker, C. (2014). A non-stationary 1981–2012 AVHRR NDVI3g time series. *Remote Sensing*, *6*(8), 6929–6960.

Sun, Y., Frankenberg, C., Wood, J. D., Schimel, D. S., Jung, M., Guanter, L., et al. (2017). OCO-2 advances photosynthesis observation from space via solar-induced chlorophyll fluorescence. *Science*, *358*(6360), eaam5747.

Wohlfahrt, G., Gerdel, K., Migliavacca, M., Rotenberg, E., Tatarinov, F., Müller, J., et al. (2018). Sun-induced fluorescence and gross primary productivity during a heat wave. *Scientific Reports*, *8*(1), 14169.

Yang, K., Ryu, Y., Dechant, B., Berry, J. A., Hwang, Y., Jiang, C., et al. (2018). Sun-induced chlorophyll fluorescence is more strongly related to absorbed light than to photosynthesis at half-hourly resolution in a rice paddy. *Remote Sensing of Environment*, *216*, 658–673.

Yang, X., Tang, J., Mustard, J. F., Lee, J., Rossini, M., Joiner, J., et al. (2015). Solar-induced chlorophyll fluorescence that correlates with canopy photosynthesis on diurnal and seasonal scales in a temperate deciduous forest. *Geophysical Research Letters*, *42*(8), 2977–2987.

Appendices

Appendix A

Description of PhotoSpec Spectrometer System[2]

A.1. Introduction

Solar-induced chlorophyll fluorescence (SIF) occurs when the photosystems in vegetation re-emit absorbed sunlight at longer wavelengths in the red and far-red regions of the electromagnetic spectrum. SIF exhibits a double peak pattern with maxima at around 685 nm and 740 nm (see Chapter 1, Fig. X) with an intensity of typically 1-2% of reflected sunlight. Within the last 10 years, researchers have developed methods to measure SIF from satellite platforms (Christian Frankenberg et al., 2011; Joiner et al., 2011), which have lead to increased interest in assessing the relationship between SIF observations and photosynthetic productivity, and how regional and global observations of SIF relate to the leaf-level phenomena where this signal originates. Bridging the gap between leaf-level and satellite measurements requires observations to be made at a range of spatial and temporal scales, and tower-based observations provide one avenue for improving our multi-scale understanding of how SIF signals can be related to photosynthesis and ecosystem productivity.

---

[2] Modified from Barr, S. 2018. “PhotoSpec Review.” Student paper for Space 590. University of Michigan.

To obtain tower-based observations of SIF, I led the construction of a PhotoSpec spectrometer system based on designs described by Grossmann et al. (2018). The PhotoSpec instrument is designed to acquire SIF observations at high temporal frequency (every ~20 s) at both red and far-red wavelengths, as well as canopy reflectance and vegetation indices such as the normalized difference vegetation index (NDVI). Because spectral retrievals of the SIF signal require the spectrometers to be optically stable, the spectrometers required strict temperature and humidity control. Light samples were collected using a 2D scanning telescope with a narrow field of view (0.7°) that allowed for the investigation of directional dependencies within the SIF signal. Specialized parts for the spectrometer housing and telescope were custom made by the Space Physics Research Lab (SPRL) at the University of Michigan. The system additionally consisted of a downwelling photosynthetically active radiation (PAR) sensor (LICOR LI-190-R) and a webcam for monitoring telescope functionality as well as the real-time state of the canopy and weather conditions.

The PhotoSpec instrument was deployed on the AmeriFlux tower at the University of Michigan Biological Station (US-UMB), above a deciduous broadleaf forest consisting primarily of oak, aspen, and maple. Acquiring data on an AmeriFlux tower allowed for comparisons with concurrent eddy flux observations of CO_2, as well as other ancillary data. As these observations are the only of their kind above a temperate deciduous forest, they provide a novel and valuable opportunity explore how SIF signals relate to ecosystem productivity and inform the interpretation of satellite-based data. Beginning in late 2019, my instrument has been recurrently targeted by the OCO-3 (Orbiting Carbon Observatory-3) instrument aboard the International Space Station (ISS), furthering future opportunities to explore how differences in scale impact remote sensing observations of SIF.

In this Appendix, I describe the various components and technical aspects of the PhotoSpec system including, in order, the spectrometer and temperature control system, the telescope unit, spatial alignment procedures, data acquisition automation, wavelength and radiometric calibration procedures, and spectral analysis.

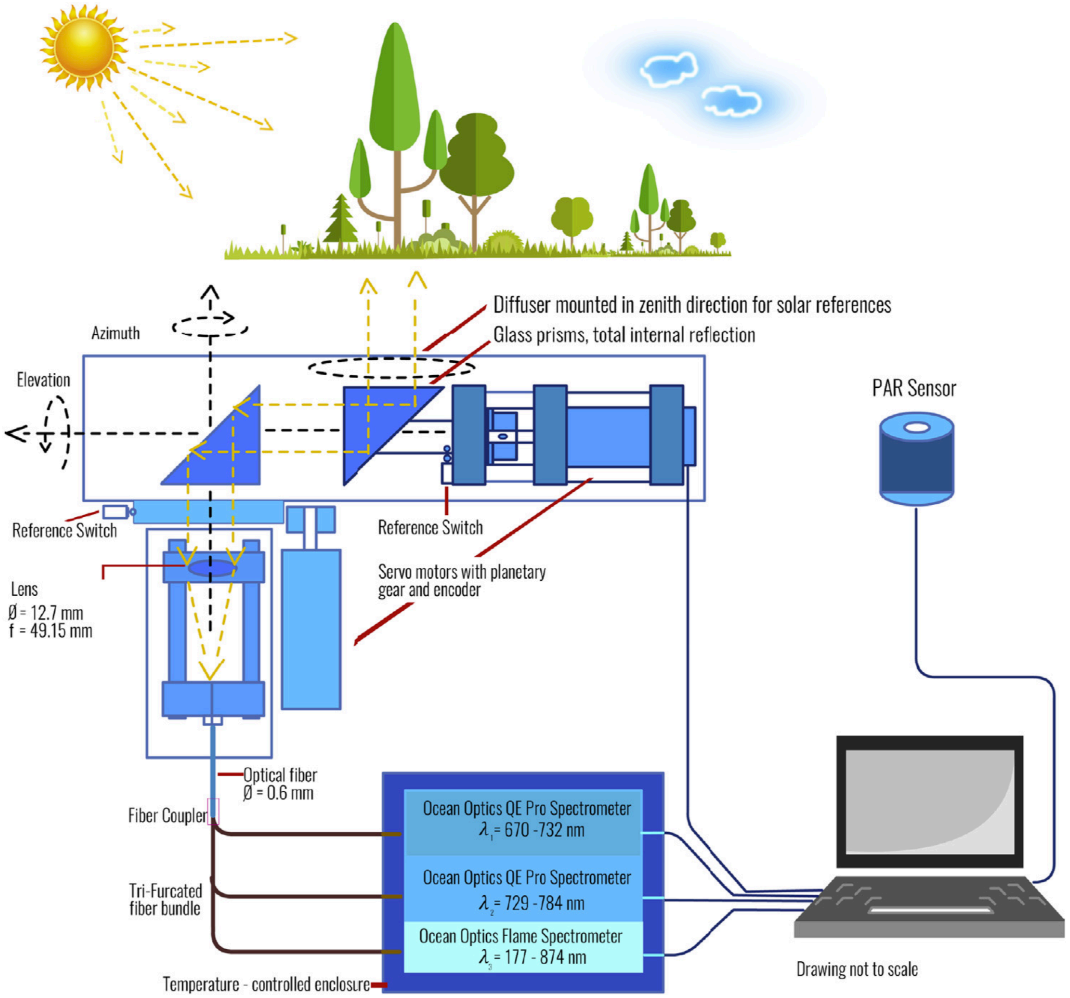

Figure A.1. Schematic Layout of PhotoSpec Instrument (from Grossmann et al., 2018).

Figure A.2. Spectrometer housing and electronics at US-UMB. The computer, power supply, and temperature controllers are housed in the electronics box on the top shelf, while spectrometers are housed in the foam-encased enclosure on the lower shelf.

A.2. Spectrometers and Temperature Control

At its core, the PhotoSpec instrument consists of three commercial spectrometers for measuring SIF and other vegetation signals. SIF signals are obtained using two narrowband QEPro (Ocean Optics Inc.) spectrometers for red and far-red wavelengths. The red QEPro has a wavelength range of 670-732 nm with a spectral resolution of 0.074 nm/pixel, while the far-red QEPro has a range of 729-794 nm and resolution of 0.067 nm/pixel. Both narrowband spectrometers have a full width half maximum (FWHM) of 0.3 nm. A broadband Flame (Ocean Optics Inc.) spectrometer, which is used to calculate NDVI and other vegetation indices, has a wavelength range of 177-874 nm with a 0.382 nm/pixel spectral resolution and 1.2 nm FWHM.

Because the PhotoSpec spectrometers require the high precision for parsing the SIF signal from reflected sunlight, the spectrometers were housed in a temperature- and humidity-stabilized container. The spectrometers themselves were mounted on an aluminum frame, and glued with a thermal conductor, allowing for heat dispersion throughout the system. Also mounted onto the frame are small heating elements, and a thermistor. These, in conjunction with a temperature controller (Arroyo), allow for the spectrometers to remain at 25° C. This frame was enclosed in insulation and placed in a larger aluminum box (Phoenix Mercano) which was also enclosed in foam insulation and kept at 18° C using a Peltier chiller (TE Technology). By heating the spectrometers within a cooled enclosure, temperature was kept to within 0.02° of the 25° C target. To maintain low humidity within the spectrometer enclosure, a slight flow of high purity nitrogen gas (i.e. dry air) was directed into the large aluminum box.

At US-UMB, the spectrometer housing and temperature controllers were kept in a building at the base of the AmeriFlux tower alongside the computer that ran the data acquisition software. The power supply (SE-200-24; Mouser Electronics) for the Peltier chiller was housed in a custom electronics box to isolate it from other electronic components.

A.3. Telescope

The telescope component of the PhotoSpec instrument is the only piece of the instrument mounted on the AmeriFlux tower. The telescope was mounted at a height of 45 m, roughly 25 m above the top of the canopy, and directed light into a fiber optic cable running to the bottom of the tower. The telescope optics consist of two prisms that direct light from the canopy towards the fiber optic, which are manipulated by two motors that rotate the elevation and azimuth angles of their field of view. Two limit switches are implemented in the telescope to home motor positions, allowing the system to maintain a viewing angle accuracy of < 1°. A collimating lens with a 12.7 mm diameter and 49.15 mm focal length is used to focus light from the prisms into the 50 m fiber optic cable, which has a numerical aperture of 0.12 and a diameter of 0.6 mm. A distributor fiber is subsequently used to direct the light signal into all three spectrometers. A diffuser disk was installed on top of the prism channel, allowing for the acquisition of reference solar spectra when the prisms were directed towards zenith.

The DC motors (1226E 012B K1855; Faulhaber Group) that directed the viewing angle of the telescope were controlled by two motor controllers (MCBL3006; Faulhaber Group). The motor controllers were housed on the tower in an aluminum box with the end of the fiber optic cable and collimating lens. The prism channel containing the two prisms and the elevation-adjusting motor sat on top of the custom aluminum box. To protect from precipitation and weather, the telescope unit was weatherized by sealing the edges of the telescope box and prism channel with aluminum tape and by using duct putty to seal access holes for the fiber and wiring. A rubber gasket was installed between the prism channel and the telescope box, in order to protect the electronics from precipitation while also allowing for the free rotation of the prism channel. The telescope unit was also covered with reflective material to prevent the electronics from overheating in the sun.

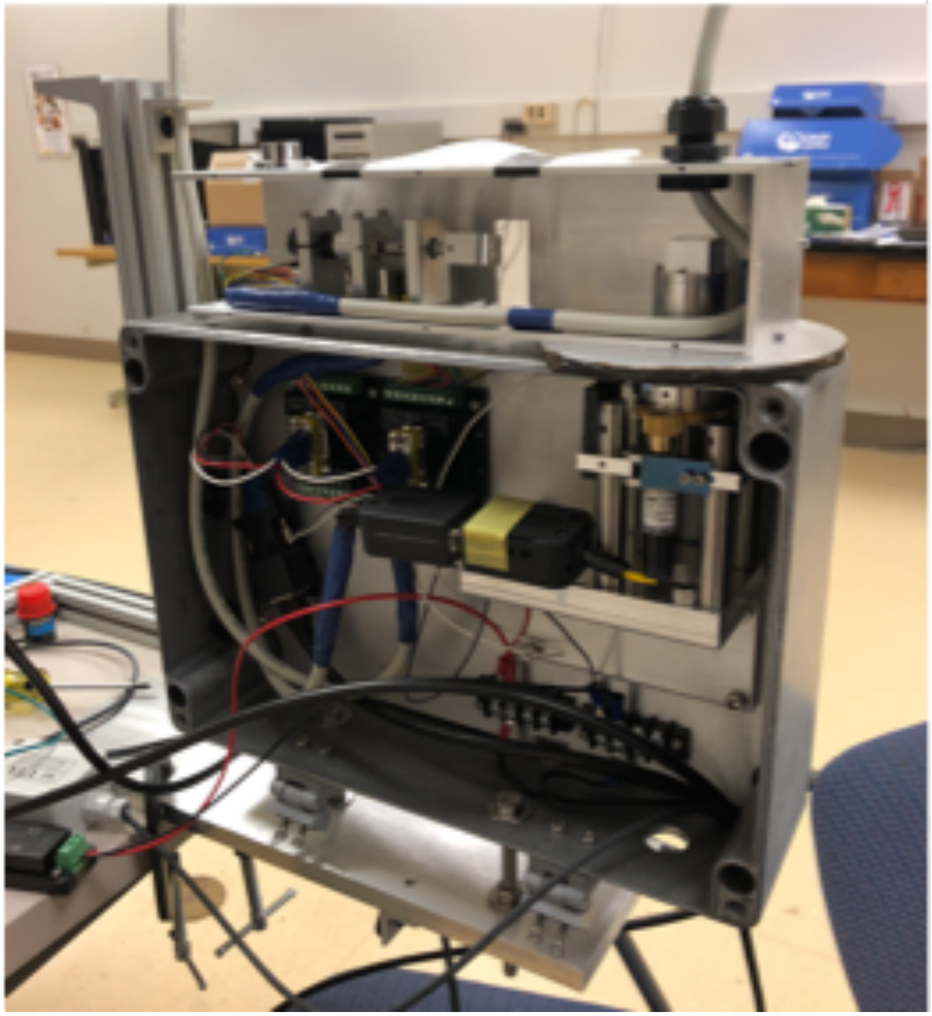

Figure A.3. Internal components of the PhotoSpec telescope unit. The larger aluminum box contains the motor controllers and the motor that controls the azimuth angle, as well as the fiber coupler and collimating lens. The prism channel on top contains the prisms and motor that controls the elevation angle.

Figure A.4. PhotoSpec telescope unit attached to the US-UMB AmeriFlux tower.

The LICOR PAR sensor was placed on a mounting plate approximately six inches above the top of the telescope. A data logger (E-1608; Measurement Computing) also housed in the telescope unit collected output from the PAR sensor and was connected to the computer at the base of the tower via an ethernet cable. Ethernet surge protectors were used between the telescope electronics and computer in order to protect the computer and spectrometers from the risk of lighting hitting the tower.

A.4. Spatial Alignment

As the directional capabilities are one of the novel aspects of the PhotoSpec system, knowing the exact viewing direction of the telescope is a critical facet of data acquisition. The telescope unit was mounted on the AmeriFlux tower using an aluminum plate and three bolts. These bolts were adjusted to level the telescope while referencing a bubble level atop the prism channel.

To further test the orientation of the telescope, we returned to the site after dark and directed a light source backwards through the fiber optic cable, illuminating the spot on the ground where the telescope optics were focused. Using this method, we tracked exactly how the telescope view changed when the motors were moved. We first moved the elevation angle to direct the light from the telescope to nadir and noted the elevation angle. We then tracked the light from the telescope as the elevation angle was slowly elevated, and noted the azimuth angle of the elevation pan. The positions of the limit switches were then adjusted in the data acquisition software such that nadir corresponded to a -90° elevation angle, and due south corresponded to an azimuth angle of 0°.

A.5. Spectrometer Calibration

Wavelength calibrations of the spectrometers were made using a mercury-argon lamp (HG-1; Ocean Optics Inc.) with well-defined spectral peaks. After identifying the pixel numbers associated with the mercury and argon emission lines, we calculated a third order polynomial relating pixel number to wavelength for each spectrometer. These polynomials were then recorded in the data acquisition and spectral analysis software, modifying the pixels to align with the correct wavelengths.

After the final connection of all optical components, we carried out a radiometric calibration to quantify the irradiance (mW/m^2/sr/nm) relative to the recorded intensities (counts/s) of the spectrometers. For the radiometric calibration, we used a second broadband Flame spectrometer that was calibrated using a radiometrically calibrated light source (HL-3P-CAL; Ocean Optics Inc.). In order to compare the calibration spectrometer to data acquire with the PhotoSpec system, we directed the PhotoSpec telescope at a Spectralon disk (Labsphere) mounted below the telescope unit. By collecting simultaneous measurements of the Spectralon disk with the calibrated Flame spectrometer, we were able to obtain radiometric calibration correction factor at specific wavelengths. These calibration spectra also allowed for the normalization of reflectances used to calculate vegetation indices.

A.6. Data Acquisition

We used DOASIS (Kraus, 2006) as the software for controlling the experiment and coordinating the spectrometers and telescope motors to acquire canopy and reference spectra. Beginning at sunrise, the PhotoSpec system begins its data acquisition algorithm and continues until sunset. I programmed the scanning algorithm to acquire canopy spectra using elevation scans from nadir to 45° below horizon at three different azimuthal angles that included 60° east of south, due south, and 60° west of south. For each footprint along an elevation scan, the PhotoSpec instrument would view a specific location for a 20 s period. We varied the exposure time of individual spectra in order to maintain a constant detector signal level, thereby mitigating nonlinearities due to spectrometer detector response. The number of individual spectra able to be collected within 20 s were then combined added together and saved as a single spectrum. Following each 20 s observation, the motors would then move to the next footprint and repeat the process. Roughly every ten scans, the prisms would be directed towards the zenith in order to acquire reference spectra. After sunset, the PhotoSpec instrument would wait until midnight and then collect dark current and background spectra by directing the prisms towards the inside of the prism channel which had been painted black. The dark and background signals were used to correct the canopy and reference spectra before applying the spectral analysis.

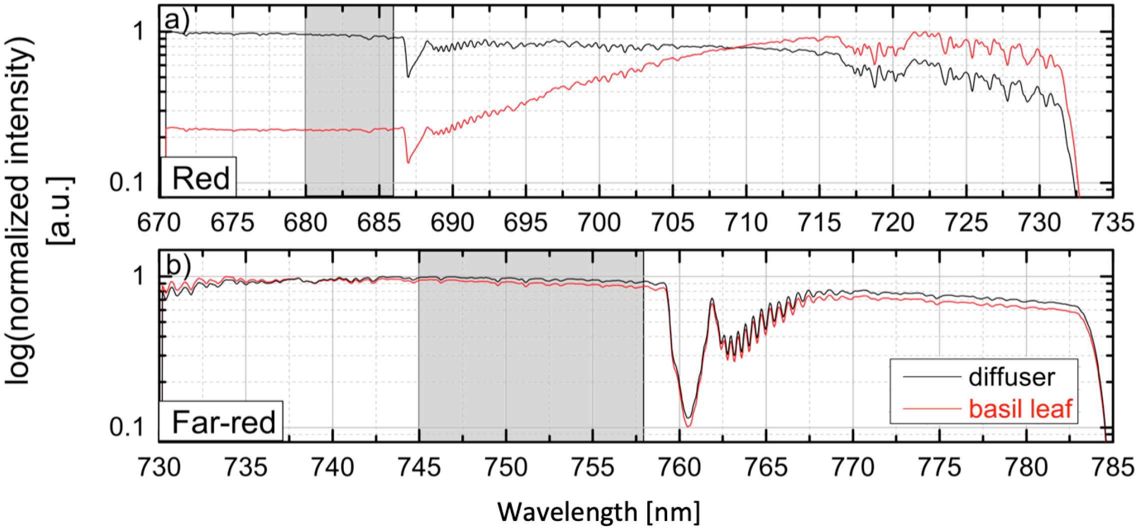

Fig. A.5. Sample spectra for the red (top) and far-red (bottom) QEPro spectrometers. Black indicates reference spectra, while red shows sample canopy spectra. Fitting windows for the respective SIF retrievals are indicated by gray shading (from Grossmann et al., 2018).

A.7. Spectral Analysis

The DOASIS software was also used to run the spectral retrievals and calculate SIF irradiances and vegetation indices. As the SIF signal is on the order of 0.5-2% of the overall spectral intensity, the retrieval calculation requires stable and high resolution spectra, thus the need for the two high resolution QEPro spectrometers and strict temperature and humidity control. While it is possible to calculate SIF irradiances from surface-based observations using the infilling of the O_2-A absorption band, atmospheric scattering effects complicate this approach using satellite-based observation (C Frankenberg et al., 2011). Instead, satellite instruments rely on the infilling of solar Fraunhofer lines, which are spectral features originating in the solar atmosphere and are less influenced by interactions with the Earth's atmosphere.

To maintain consistency with satellite observations, we focused our spectral retrievals on wavelength regions containing solar Fraunhofer lines. The fitting window for the red QEPro was 680-686 nm, while the fitting window in the far-red was 745-756 nm. Spectral fits were calculated using a physical linearized least-squares approach, where the SIF signal was assumed to be linear within the fitting window. While satellite-based SIF datasets generally utilize a fully non-linear retrieval of the SIF signal, using a linear least-squares method expedited computing times and guaranteed a mathematical solution to the spectral fits. From the first-step of the linear retrieval, an approximate solution for SIF intensity was typically within 10% of the true SIF signal. As a second step, the residual signal was again analyzed with throught the retrieval process, bringing the approximated SIF value to within 0-3% for the red and 0-0.3% for the far-red (see Grossmann et al., 2018). Once final SIF values were obtained by the DOASIS fitting algorithm, these values were multiplied by the radiometric calibration factors to convert from units of counts/s to irradiances.

References

Frankenberg, C, Butz, A., & Toon, G. C. (2011). Disentangling chlorophyll fluorescence from atmospheric scattering effects in O2 A-band spectra of reflected sun-light. *Geophysical Research Letters*, *38*(3).

Frankenberg, Christian, Fisher, J. B., Worden, J., Badgley, G., Saatchi, S. S., Lee, J., et al. (2011). New global observations of the terrestrial carbon cycle from GOSAT: Patterns of plant fluorescence with gross primary productivity. *Geophysical Research Letters*, *38*(17).

Grossmann, K., Frankenberg, C., Magney, T. S., Hurlock, S. C., Seibt, U., & Stutz, J. (2018). Remote Sensing of Environment PhotoSpec : A new instrument to measure spatially distributed red and far- red Solar-Induced Chlorophyll Fluorescence. *Remote Sensing of Environment*, *216*(June), 311–327. https://doi.org/10.1016/j.rse.2018.07.002

Joiner, J., Yoshida, Y., Vasilkov, A. P., & Middleton, E. M. (2011). First observations of global and seasonal terrestrial chlorophyll fluorescence from space. *Biogeosciences*, *8*(3), 637–651.

Kraus, S. (2006). *DOASIS: A framework design for DOAS*. Shaker.

Appendix B

Supplemental Material for Chapter 2

Table B1. Months included in each season (spring, summer, and fall) for the four focus regions: Temperate Mixed Forest (TMF), Boreal Coniferous Forest (BCF), Midwest Cropland (MC), and Canadian Great Plains (CGP). The beginning of spring and end of fall were determined using a 0° C temperature threshold, while an 85% SIF threshold was used to define summer months. Spring and fall were additionally limited to consist of at most 3 months.

	Spring	**Summer**	**Fall**
TMF	April, May	June, July	August, September, October
BCF	May, June	July	August, September, October
MC	April, May, June	July, August	September, October, November
CGP	April, May, June	July	August, September, October

Table B2. Estimated influence of the spatial point spread function (PSF) for GOME-2 gridded data for both 0.5° and 1.0° spatial resolution at 45° latitude. PSF mean indicates the fraction of pixel-level data originating from within a respective grid cell. GOME-2 aboard MetOp-A had a footprint size of 40km x 80km before July 15, 2013 and of 40km x 40km afterwards, and the 0.5° gridded data typically contained 10-25 soundings per grid cell (Joiner et al., 2013). As soundings are not distributed uniformly within a grid cell, we used a Monte Carlo technique to estimate the PSF by randomly placing the centers of 15 (or 60) satellite footprints within a 0.5° (or 1.0°) grid cell for each footprint size. PSF mean values were then calculated as the fraction of total footprints falling within the grid cell boundaries. Values calculated at 45° latitude are representative of the majority of locations used in our site level analysis, but decrease significantly at higher latitudes (to as little as 0.15-0.21 for 40km x 80km soundings at FI-Sod). Means and standard deviations were calculated based on 10,000 simulations.

		40km x 40km		40km x 80km	
Grid cell size	**# of soundings**	**PSF mean**	**Standard deviation**	**PSF mean**	**Standard deviation**
0.5°	**15**	0.61	0.04	0.40	0.02
1.0°	**60**	0.79	0.03	0.67	0.02

Table B3. Coefficients of Variability (CVs) in four ecoregions: Temperate Mixed Forest (TMF), Boreal Coniferous Forest (BCF), Midwest Cropland (MC), and Canadian Great Plains (CGP). The CV is defined as the ratio of the interannual standard deviations to the seasonal amplitude of the multi-year mean, where the interannual standard deviation has been calculated separately for the full year (A-O), spring (AM), summer (JJA), and fall (SO).

	Annual IAV (%)	Spring IAV (%)	Summer IAV (%)	Fall IAV (%)
TMF				
GOME-2 SIF	2.3%	8.5%	4.3%	3.1%
MODIS NIRv	1.6%	3.9%	1.3%	5.0%
MODIS NDVI	2.3%	6.4%	1.7%	2.9%
AVHRR NDVI	3.2%	11.5%	1.8%	2.2%
BCF				
GOME-2 SIF	4.1%	10.1%	10.9%	5.5%
MODIS NIRv	2.5%	5.3%	4.4%	4.3%
MODIS NDVI	1.9%	5.3%	1.8%	2.2%
AVHRR NDVI	2.9%	8.0%	6.1%	3.2%
MC				
GOME-2 SIF	1.8%	4.8%	5.4%	2.6%
MODIS NIRv	2.6%	3.7%	7.1%	4.4%
MODIS NDVI	2.0%	3.5%	4.1%	4.0%
AVHRR NDVI	1.5%	5.4%	4.1%	3.2%
CGP				
GOME-2 SIF	2.8%	4.3%	9.4%	2.4%
MODIS NIRv	3.1%	3.8%	6.8%	2.9%
MODIS NDVI	2.2%	3.7%	4.1%	2.1%
AVHRR NDVI	2.5%	3.3%	5.1%	3.0%

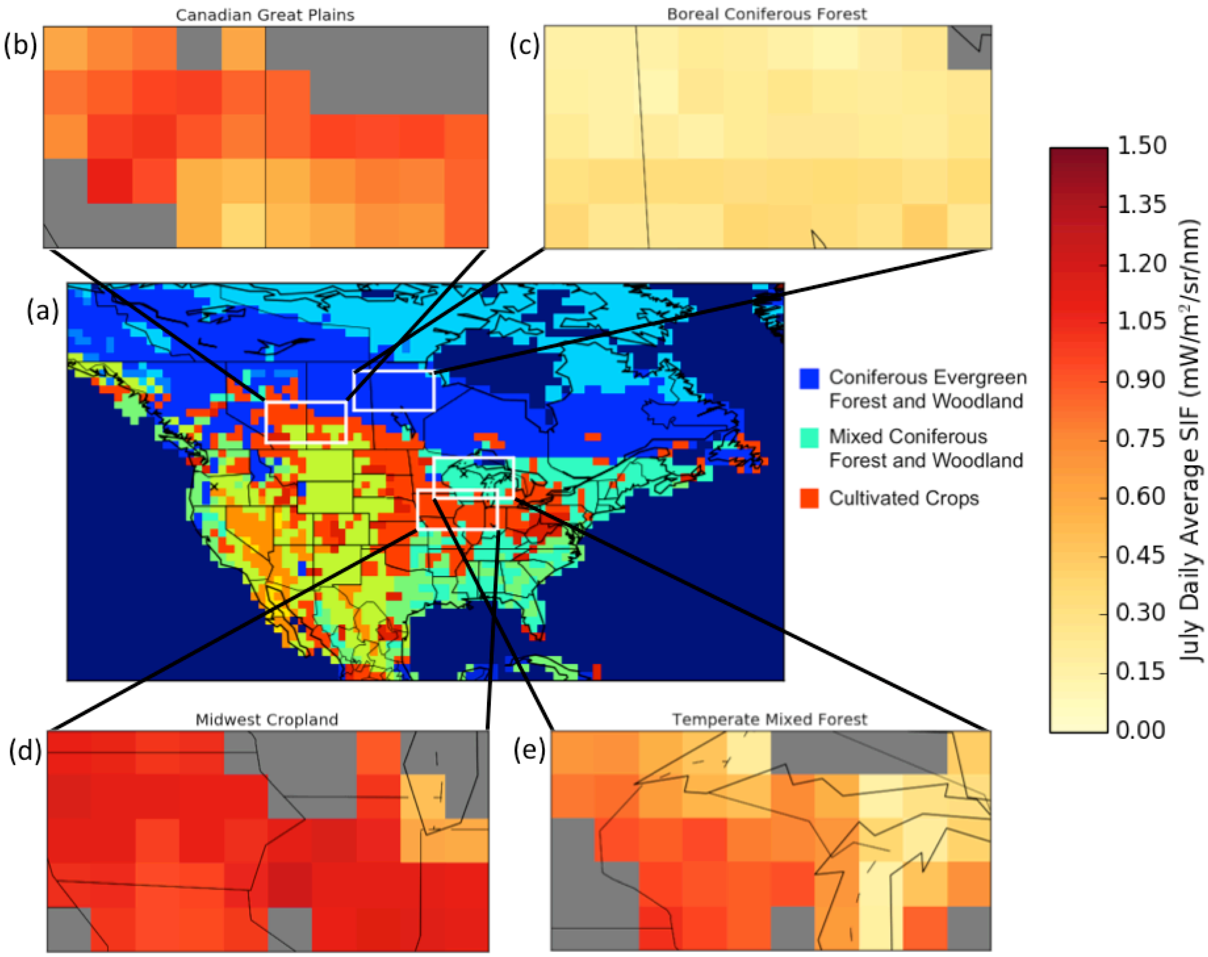

Fig. B1. (a) Land classification from AVHRR (Hansen et al., 1998) at 1° x 1° resolution, and July mean SIF values from GOME-2 for: (b) Canadian Great Plains, masked by Cultivated Crops; (c) Boreal Coniferous Forest, masked by Coniferous Evergreen Forest and Woodland; (d) Midwest Cropland, masked by Cultivated Crops; and (e) Temperate Mixed Forest, masked by Mixed Coniferous Forest and Woodland.

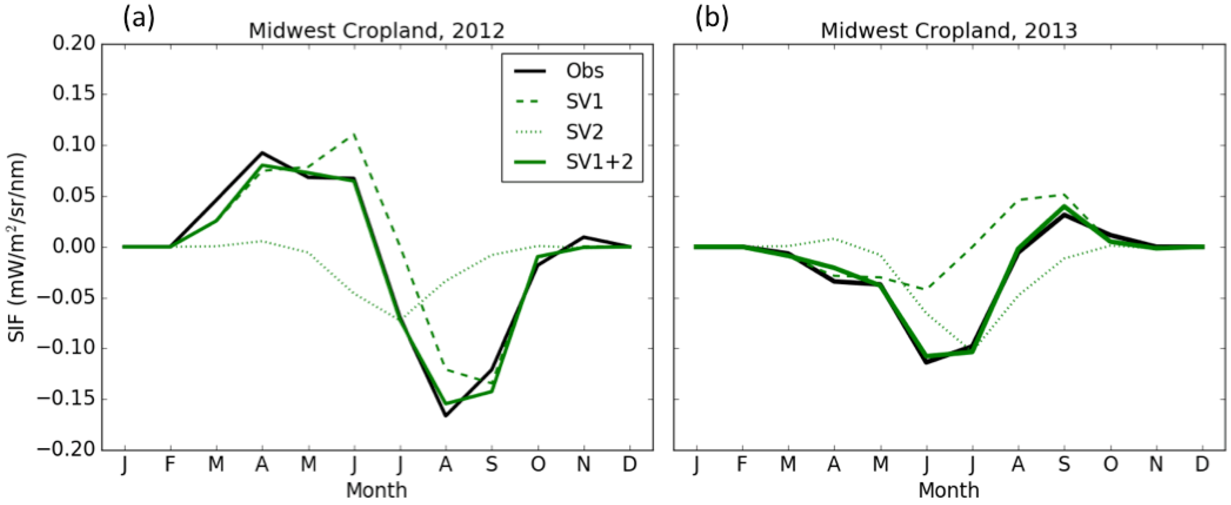

Fig. B2. Regional anomalies in SIF over the Midwest cropland during two contrasting years: (a) 2012 and (b) 2013. Black solid lines indicate observed anomalies, while green solid lines indicate anomalies reconstructed from the sum of the two dominant singular vector contributions. The individual contributions from the first (green dashed lines) and second (green dotted lines) singular vectors are also included, the magnitude of which are determined by the product of the unmodified singular vector (Fig. 4) and the respective weight for that year. In this case, the associated weights for the first singular vector are roughly 0.7 for 2012 and -0.3 for 2013, while the second singular vector weights are roughly -0.4 for 2012 and -0.6 for 2013.

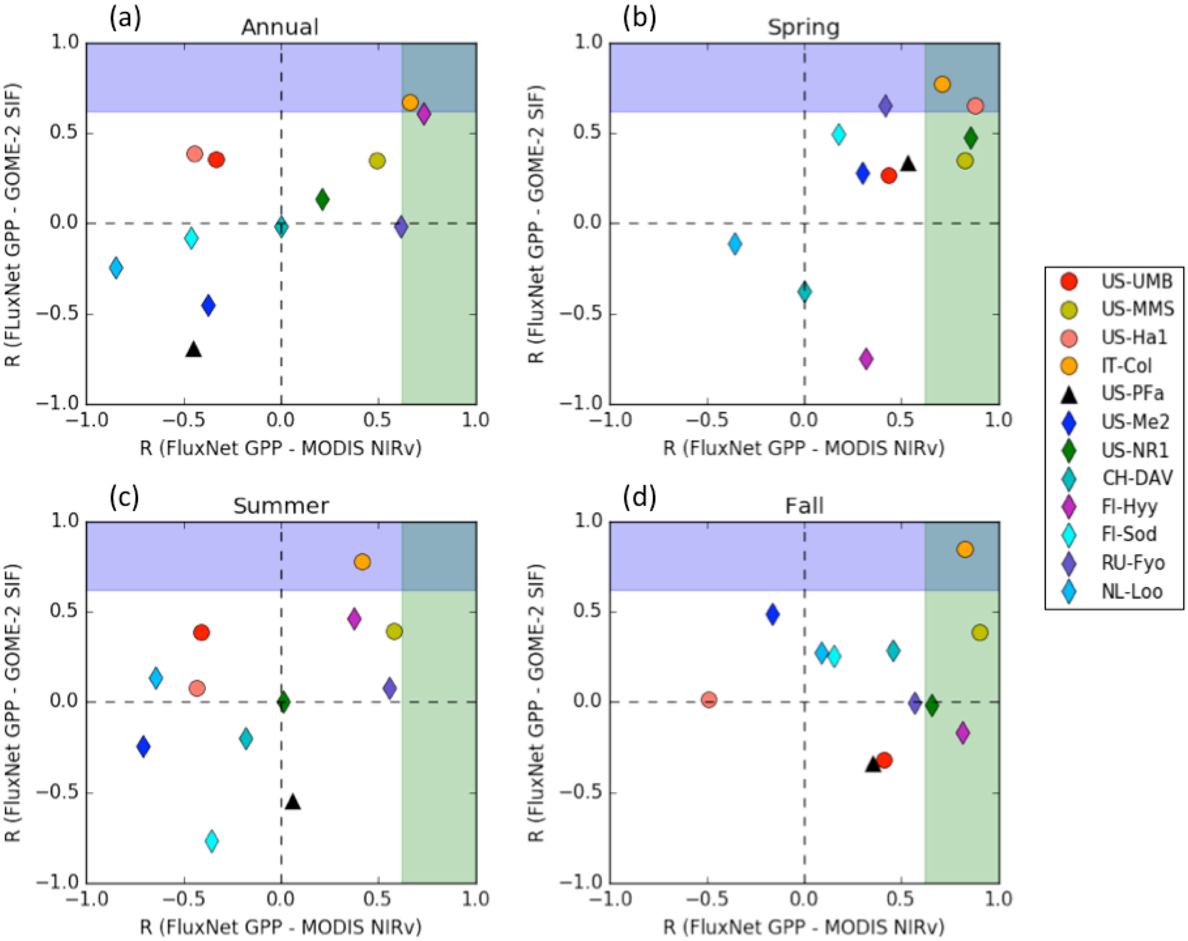

Fig. B3. Comparison between correlation coefficients of interannual anomalies in FLUXNET NT GPP against GOME-2 SIF and MODIS NIR_V using satellite data averaged over a 0.5° grid cell containing the respective FLUXNET site at annual (a) and seasonal (b-d) timescales from 2007 through 2014. Spring, summer, and fall seasons are defined by using a 0° C temperature threshold to determine the beginning of spring and end of fall, and an 85% GPP threshold to determine summer months. Round symbols indicate sites in deciduous broadleaf forest, diamonds indicate evergreen needleleaf forest, and triangles indicate mixed forest. Shaded regions indicate statistically significant ($p<0.1$) positive correlations.

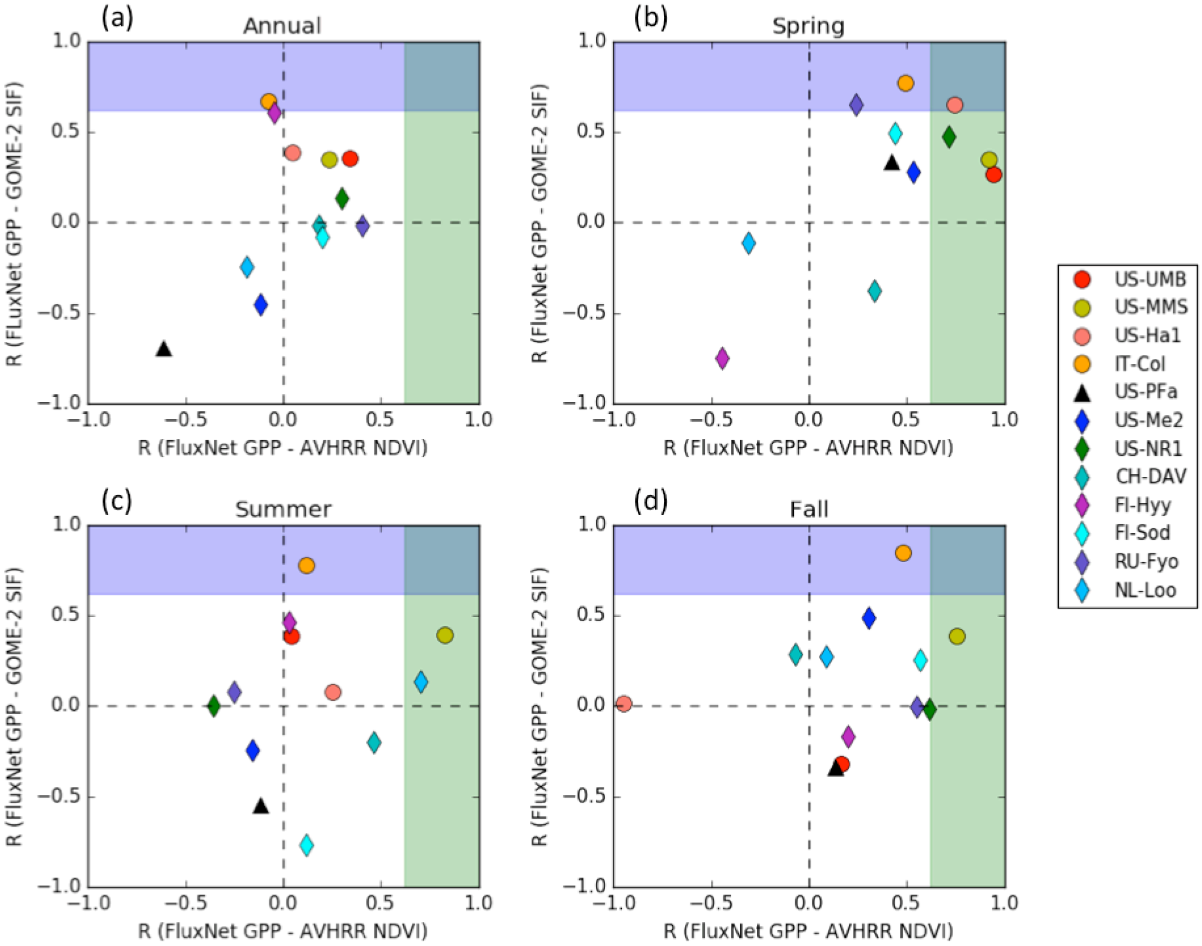

Fig. B4. Same as Fig. B3 but with AVHRR NDVI in place of MODIS NIR$_V$.

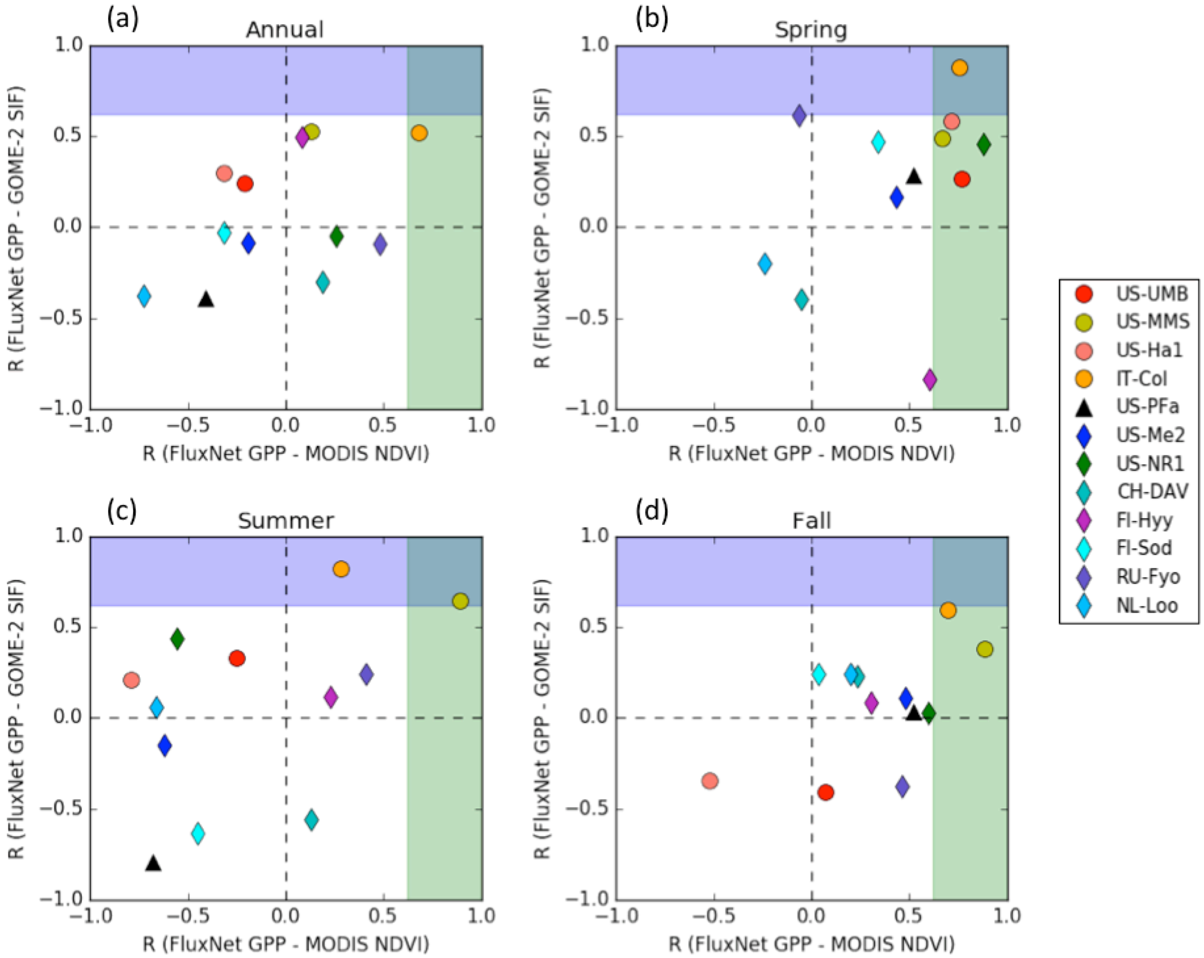

Fig. B5. Same as Fig. B3 but with FLUXNET DT GPP in place of FLUXNET NT GPP, and MODIS NDVI in place of MODIS NIR_V.

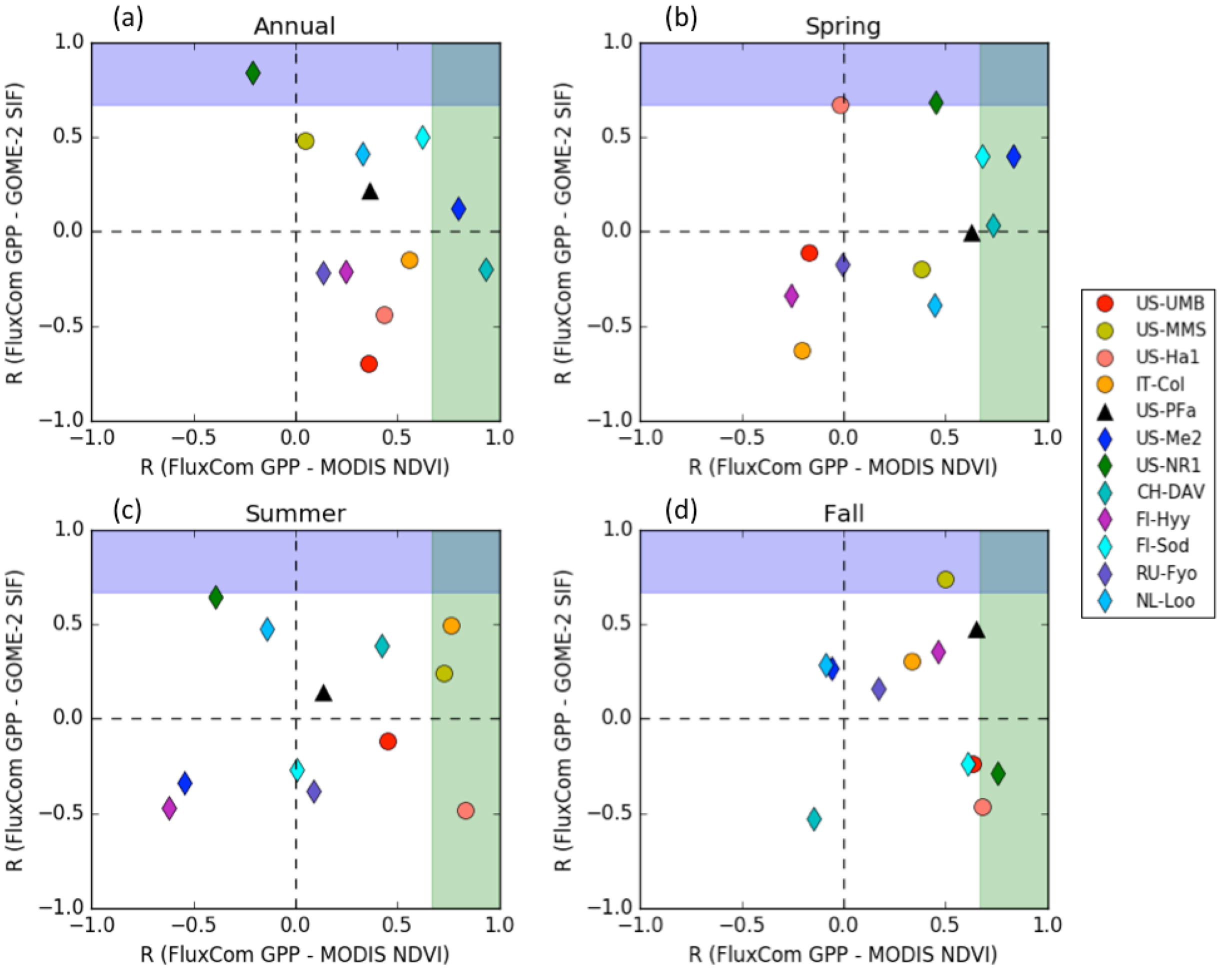

Fig. B6. Same as Fig. B3 but with FLUXCOM GPP in place of FLUXNET NT GPP, and MODIS NDVI in place of MODIS NIR$_V$. As the pixel containing US-UMB is classified as lake in the FLUXCOM dataset, the correlations for that site are from the pixel directly south.

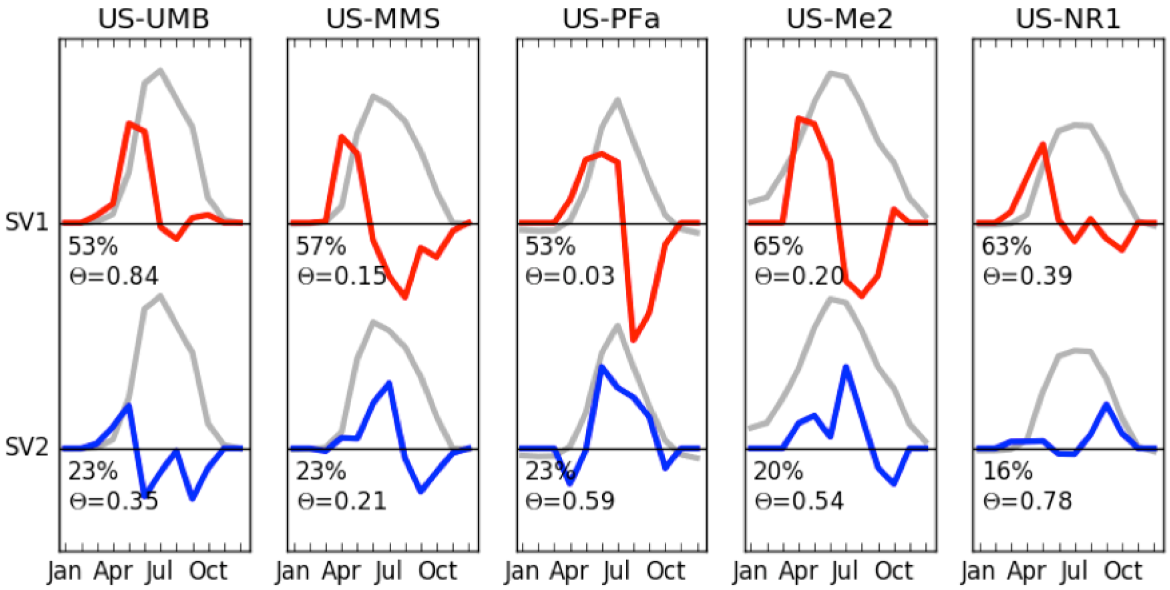

Fig. B7. First and second singular vectors resulting from the decomposition of the interannual variability of FLUXNET NT GPP at the five North American FLUXNET2015 sites from 2007-2014. Gray lines show the climatological mean annual cycle. Red vectors indicate a temporal redistribution of productivity within the growing season, while blue vectors indicate an amplification of peak seasonal signal. Each singular vector has an associated percentage of interannual variability that is described by the respective vector, and a θ value that indicates net impact on the integrated seasonal signal.

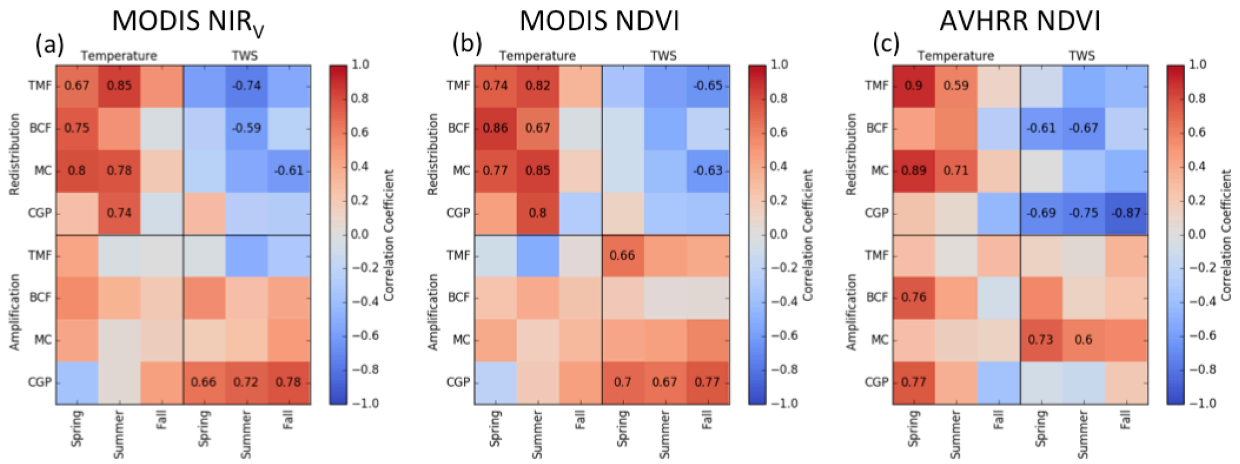

Fig. B8. Correlation coefficients between the (a) MODIS NIR$_V$, (b) MODIS NDVI, and (c) AVHRR NDVI redistribution and amplification vectors and seasonal temperature and liquid water equivalent anomalies for the Temperate Mixed Forest (TMF), Boreal Coniferous Forest (BCF), Midwest Cropland (MC), and Canadian Great Plains (CGP) regions. Red shading indicates that positive anomalies in temperature or moisture are associated with redistribution of productivity towards earlier in the growing season (for Redistribution) or an increase in peak growing season signal (for Amplification); blue shading indicates the opposite. Numbers in grid cells indicate statistically significant ($p<0.1$) correlations.

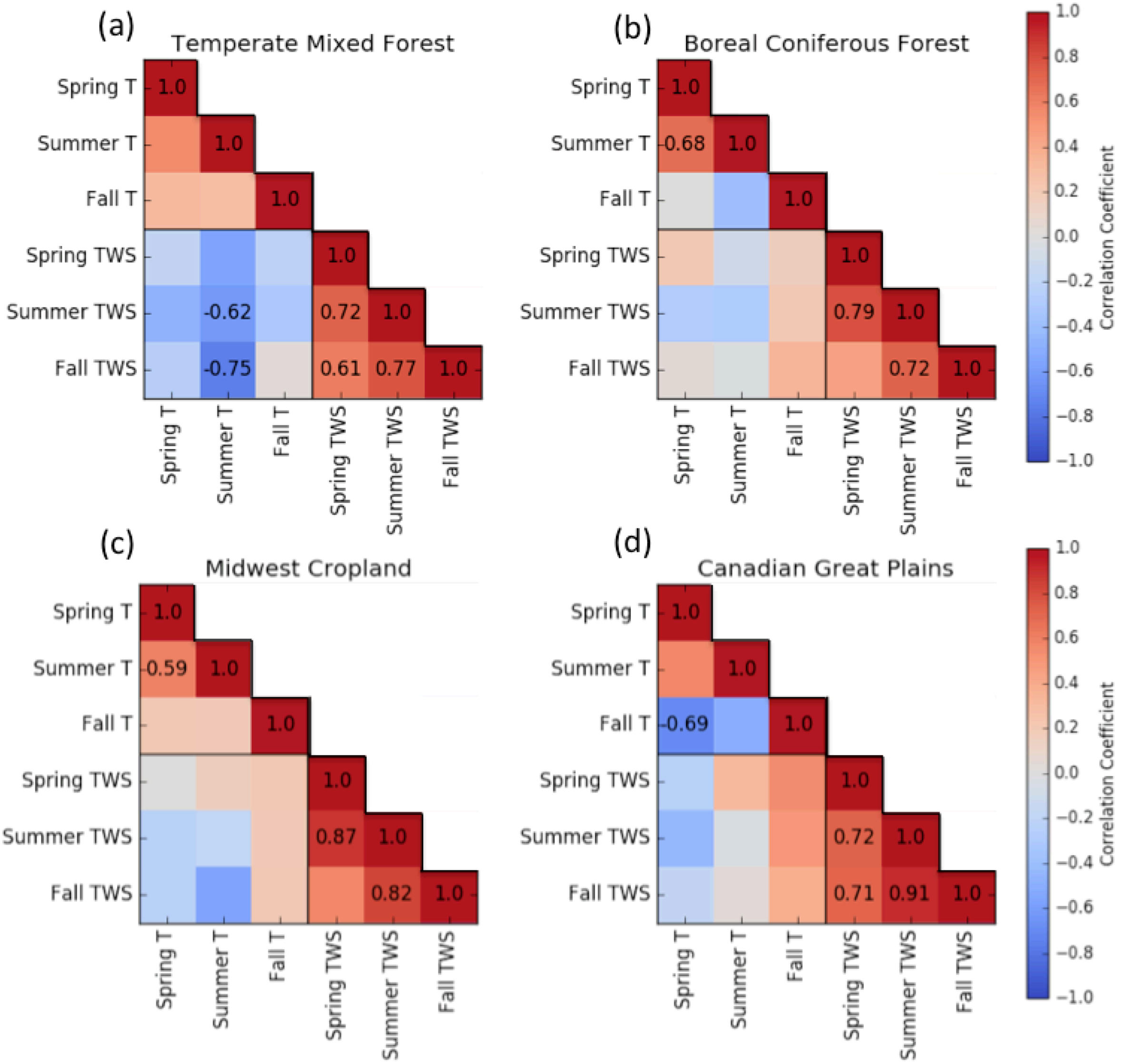

Fig. B9. Correlation coefficients between seasonal climate anomalies in the (a) Temperate Mixed Forest, (b) Boreal Coniferous Forest, (c) Midwest Cropland, and (d) Canadian Great Plains regions. Numbers in grid cells indicate statistically significant ($p<0.1$) correlations.

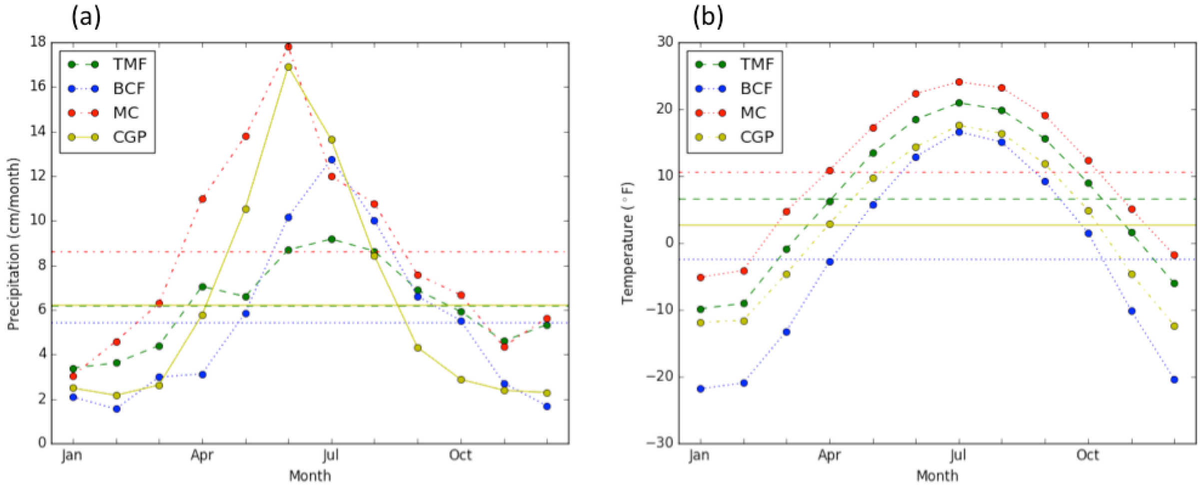

Fig. B10. Climatological monthly mean (a) temperature and (b) precipitation (2007-2015) for Temperate Mixed Forest (TMF), Boreal Coniferous Forest (BCF), Midwest Cropland (MC), and Canadian Great Plains (CGP) regions. Horizontal lines indicate annual mean values.

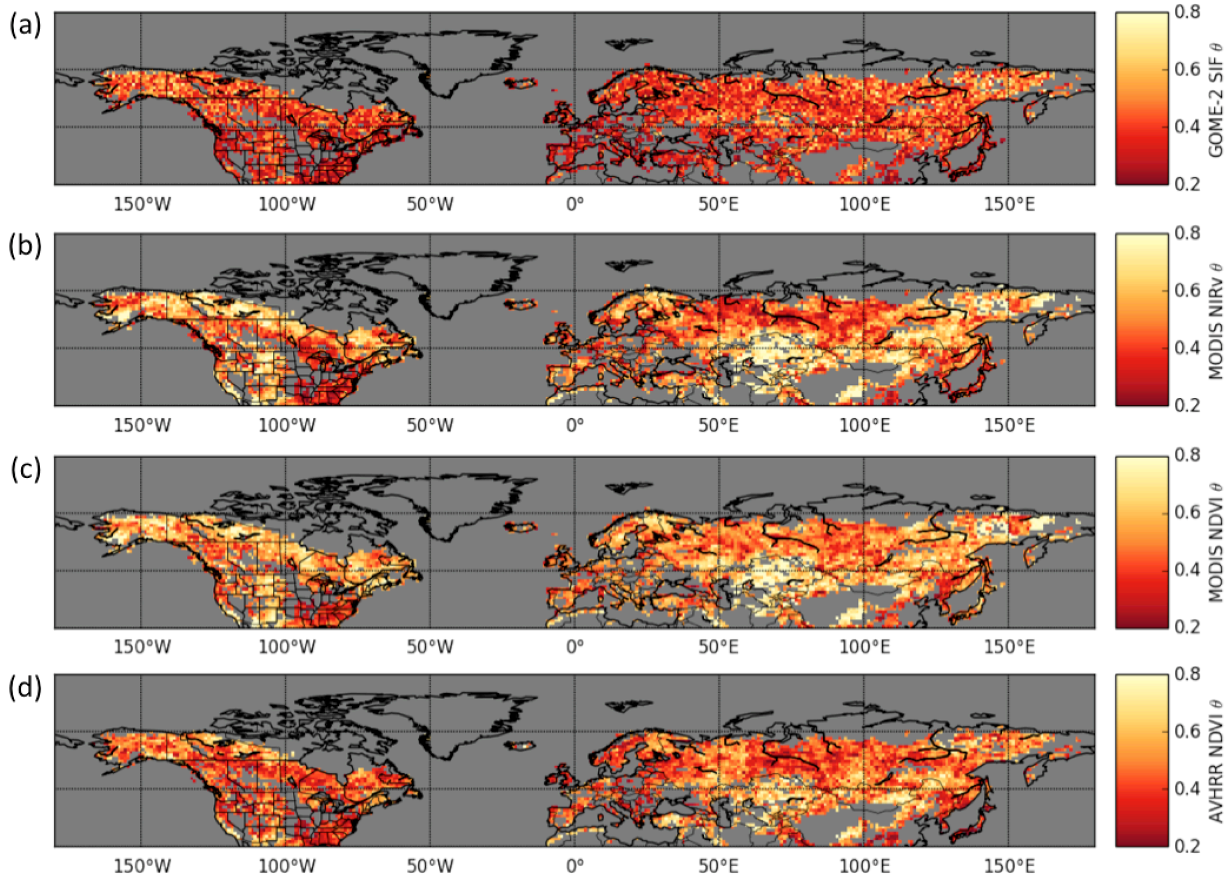

Fig. B11. Spatial maps of observational θ values from non-crop grid cells using (a) GOME-2 SIF, (b) MODIS NIR_V, (c) MODIS NDVI, and (c) AVHRR NDVI.

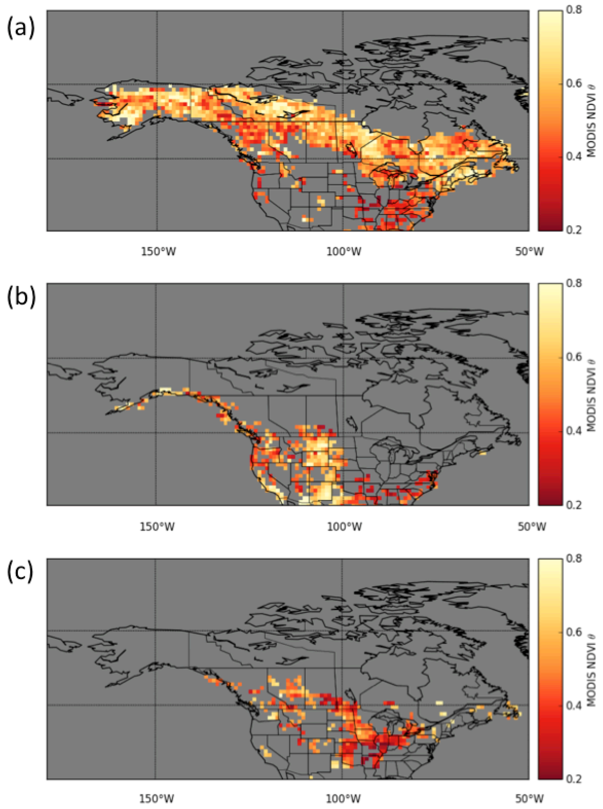

Fig. B12. Spatial maps of θ values calculated from MODIS NDVI over North America for (a) forested pixels, (b) non-crop grassland, and (c) cropland.

References

Hansen, M., DeFries, R., Townshend, J.R.G., Sohlberg, R., 1998. Land cover classification derived from AVHRR. Coll. Park. MD Glob. L. Cover Facil.

Joiner, J., Guanter, L., Lindstrot, R., Voigt, M., Vasilkov, A.P., Middleton, E.M., Huemmrich, K.F., Yoshida, Y., Frankenberg, C., 2013. Global monitoring of terrestrial chlorophyll fluorescence from moderate-spectral-resolution near-infrared satellite measurements: methodology, simulations, and application to GOME-2. Atmos. Meas. Tech. 6, 2803–2823.

Appendix C

Supplemental Material for Chapter 3

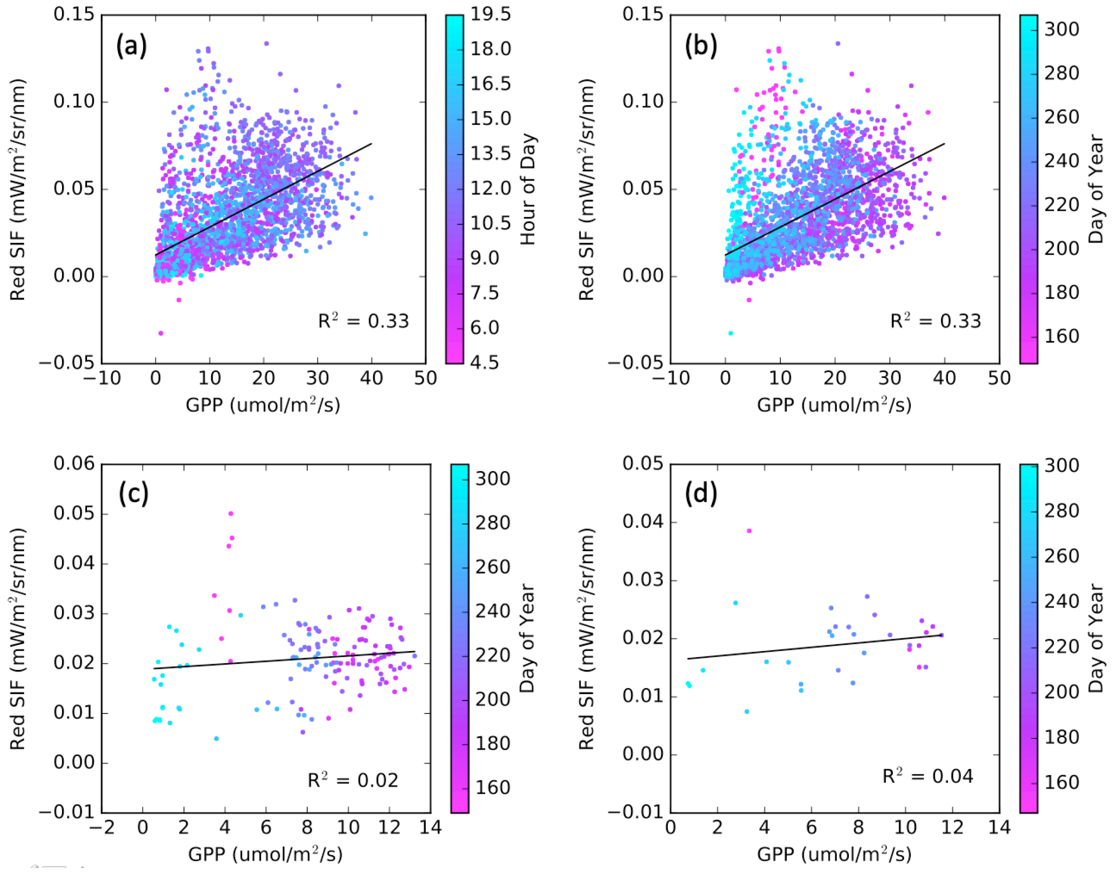

Fig. C1. Correlation plots between red SIF and GPP at 90 minute (a-b), daily (c), and weekly (d) temporal resolution observations. Color bars are weighted by day of year (b-d) or by hour of day (a).

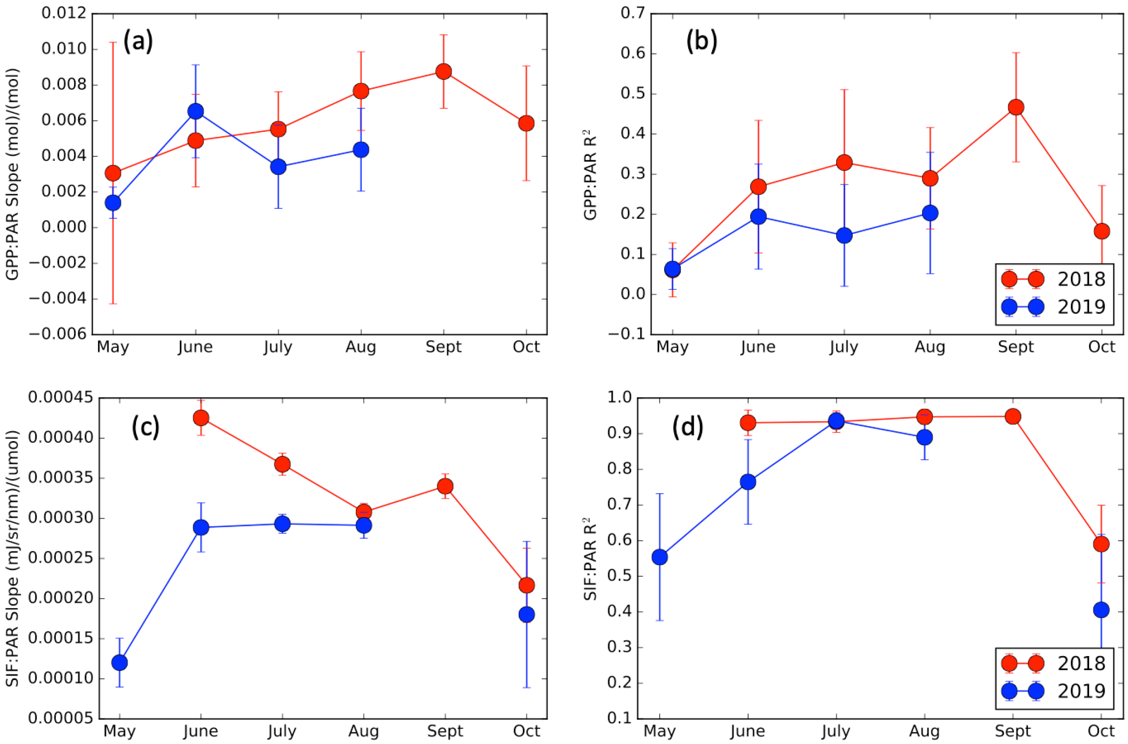

Fig. C2. Slopes and correlation coefficients from monthly linear fits of daily-averaged GPP (a-b) and far-red SIF (c-d) with PAR. Data from 2018 are in red, while 2019 data are in blue. Error bars represent the standard deviations of results from a bootstrapping method used to test the robustness of the linear regressions.

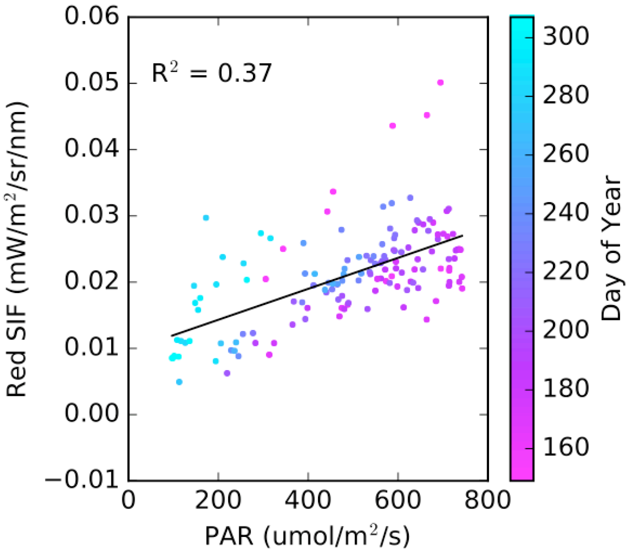

Fig. C3. Correlation plot between daily-averaged red SIF and photosynthetically active radiation (PAR). Color bar is weighted by day of year.

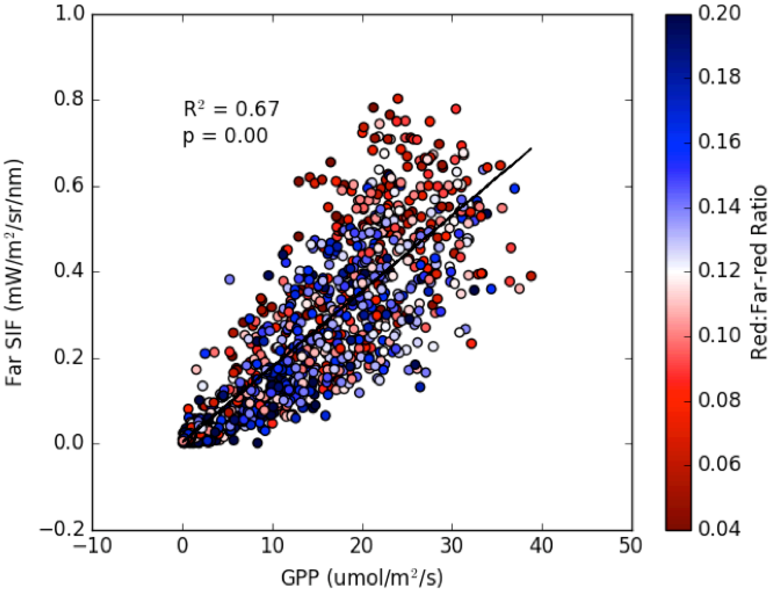

Fig. C4. Correlation plot between 90-minute far-red SIF and GPP observations. Color scale is weighted by the red:far-red SIF ratio. (Compare with Fig. 7b from Magney et al., 2019.)

Appendix D

Supplemental Material for Chapter 4

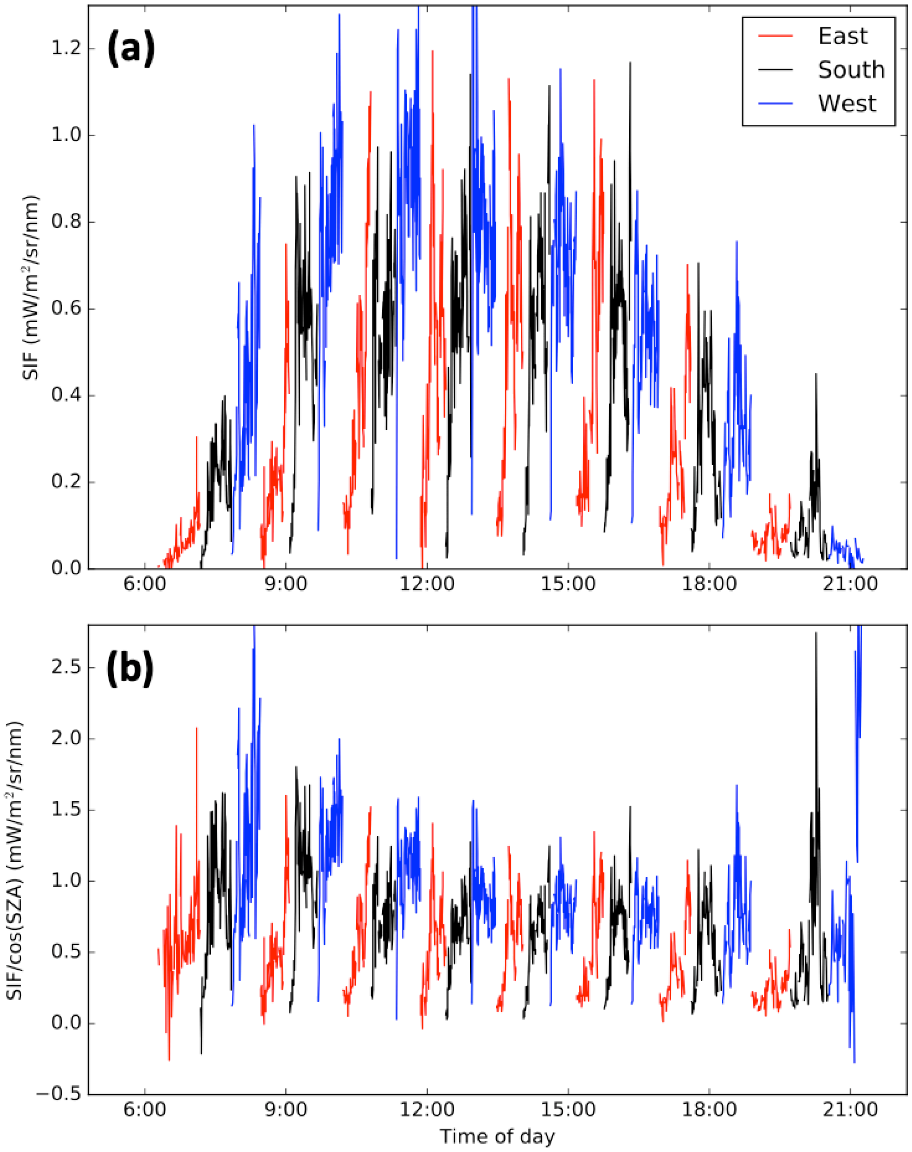

Fig. D1. A single day timeseries of far-red SIF observations under sunny conditions on July 18, 2018. The upper panel (a) shows unprocessed data, with the eastward azimuthal scan in red, southward scan in black, and westward scan in blue. In the lower panel (b), SIF observations have been normalized by dividing by the cosine of the SZA.

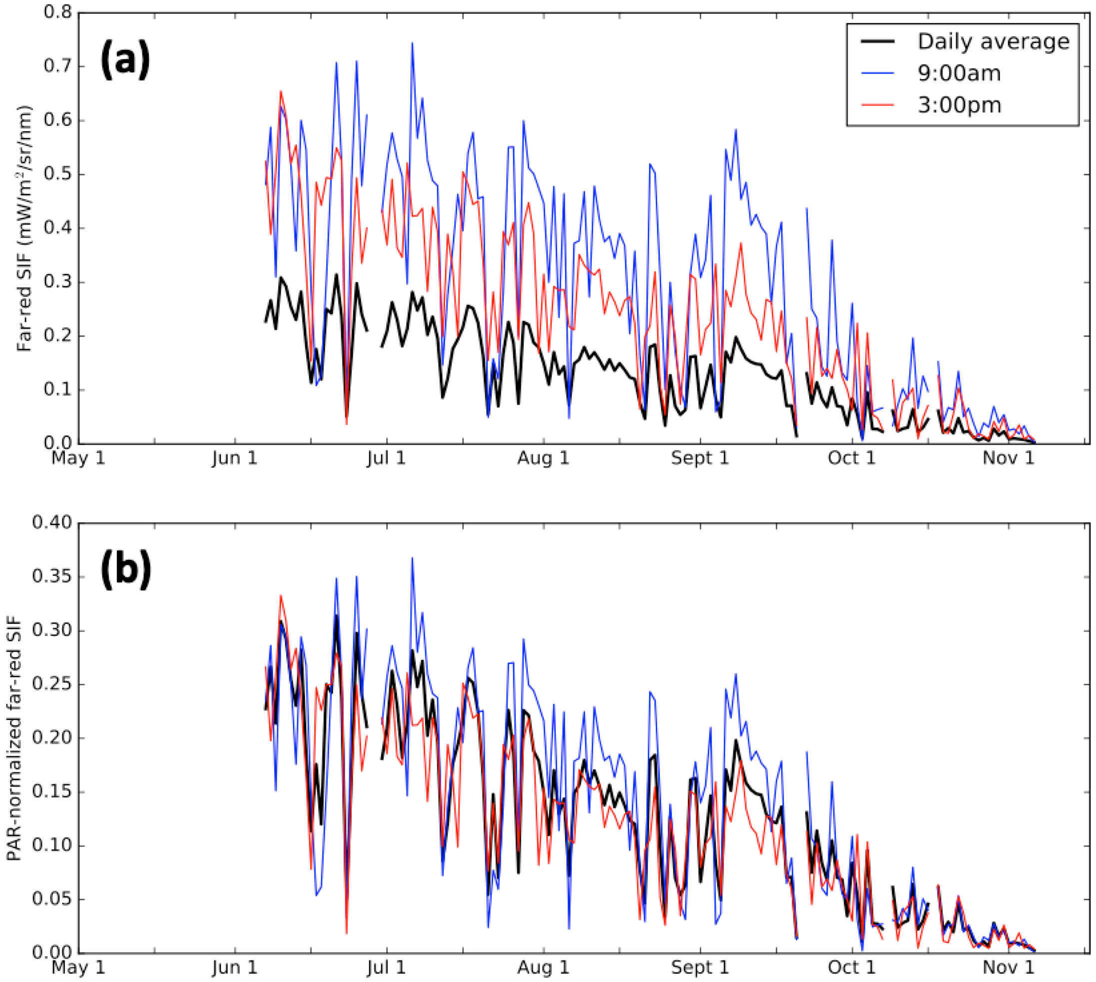

Fig. D2. Timeseries of far-red SIF observations during the 2018 growing season. The black line indicates the daily-averaged signal, while 9:00am values are in blue and 3:00pm values are in red. The upper panel (a) shows the raw data, and a clear-sky PAR proxy has been used to normalize morning and afternoon observations to daily-average estimates in the lower panel (b).

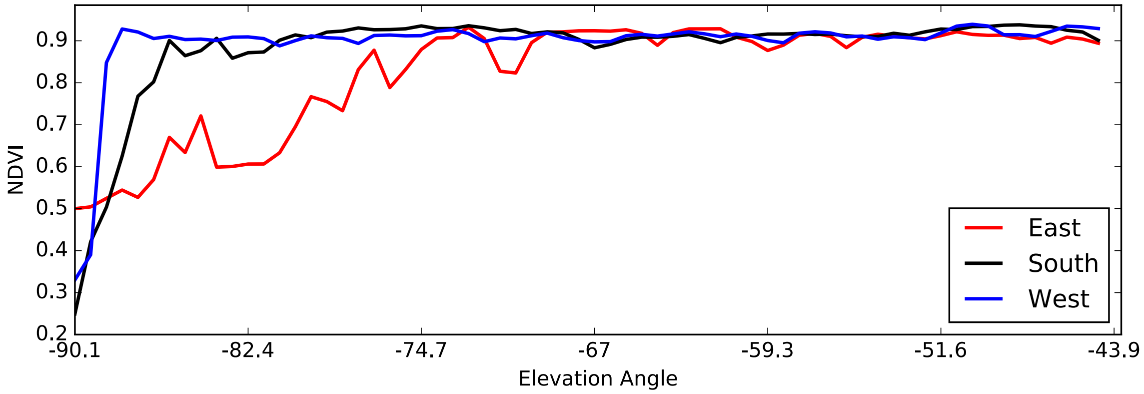

Fig. D3. Mean July NDVI values across elevation angles for the three (60° east of south in red, due south in black, 60° west of south in blue) azimuthal scans incorporated in the SIF data. The west-facing scan observes a more uniform canopy as indicated by fewer variations in the NDVI signal. Lower and more variable NDVI values, especially in the east-facing data, indicate a more heterogeneous canopy structure.